Implications of physics beyond the Standard Model in the quark and lepton sectors

DISSERTATION

zur Erlangung des akademischen Grades
doctor rerum naturalium
(Dr. rer. nat.)
im Fach: Physik
Spezialisierung: Theoretisch physik

eingereicht an der
Mathematisch-Naturwissenschaftlichen Fakultät
der Humboldt-Universität zu Berlin

von

M.Sc. Rasmus Westphal Rasmussen

Präsident der Humboldt-Universität zu Berlin:
Prof. Dr.-Ing. Dr. Sabine Kunst

Dekan der Mathematisch-Naturwissenschaftlichen Fakultät:
Prof. Dr. Elmar Kulke

Gutachter: 1. Priv.-Doz. Dr. Walter Winter

2. Prof. Dr. Christophe Grojean
3. Dr. Werner Rodejohann

Tag der mündlichen Prüfung: 10-04-2018

Implications of physics beyond the Standard Model in the quark and lepton sectors

A dissertation submitted for the degree of
Doctor rerum naturalium (Dr. rer. nat.)

Rasmus Westphal Rasmussen
Mathematisch-Naturwissenschaftlichen Fakultät
Institut für Physik
Humboldt-Universität zu Berlin

Doctoral degree committee: *Walter Winter, Christophe Grojean, Werner Rodejohann, Heiko Lacker, Alejandro Saenz*

Year of dissertation defense: 10-04-2018

Abstract

The Standard Model (SM) of particle physics is a well-tested and predictive theory, being celebrated as one of the most successful models in newer time. However, non-zero neutrino masses, the existence of dark matter, and the baryon asymmetry suggest physics beyond the SM since the SM is not capable of explaining these phenomena. Thus, in order to have a model consistent with observations, a more complete theory is needed. There are several Beyond the Standard Model (BSM) scenarios which can replace the SM, and each of them lead to different new physics signatures. Experimentally, one can search for new physics, either producing it directly in particle physics experiments or indirectly by observing deviations from the SM prediction. This makes it possible to test each BSM scenario, and we consider both possibilities in this thesis.

We consider BSM scenarios in the quark and lepton sectors, and study their phenomenological consequence on measurable observables. A specific example studied in this thesis is sterile neutrinos, and we consider sterile neutrino masses at the eV, GeV and 10^{12} GeV scale in the context of symmetry-generated or structureless neutrino mass models. For the GeV sterile neutrinos, we find a distinct hierarchy among the flavor-dependent active-sterile mixings in the symmetry-generated mass models, which acts as a model discriminator. Considering 10^{12} GeV scaled sterile neutrinos, they can, when combined with thermal leptogenesis, generate the baryon asymmetry in addition to small neutrino masses. As a result, either a broad or peaked sterile neutrino mass distribution is predicted from symmetry-generated or anarchical neutrino mass models, respectively. Anarchical neutrino mass models with eV sterile neutrino leads to either flavor-independent or flavor-dependent active-sterile mixing distributions, depending on the method used in the analysis.

Similarly as using symmetries in the neutrino sector, one can also use symmetries in quark mass models. This thesis consider symmetries capable of quantizing the Cabibbo quark mixing angle to leading order. As a result, a variety of possible symmetries are obtained, which can be used to build specific quark mass models.

Probing BSM physics indirectly via astrophysical neutrinos, acts as an alternative to direct detection, and using the neutrino flavor composition as observable, BSM physics leads to clear deviations from expectation. Additional information comes from other effects, and it helps in constraining the parameter space further. Beside discussing different BSM scenarios, we illustrate the potential of future experiments, emphasizing their effectiveness to test and discriminate BSM physics.

Zusammenfassung

Das Standardmodell (SM) der Teilchenphysik hat sich in der Praxis als vielseitige Theorie bewährt, und wird als eines der erfolgreichsten Modelle der modernen Physik angesehen. Dennoch deuten nichtverschwindende Neutrinomassen, dunkle Materie und Baryonenasymmetrie auf Physik jenseits des SM (BSM) hin, denn diese Phänomene können durch das SM nicht begründet werden. Um also ein mit den Beobachtungen konsistentes Modell zu entwickeln, ist eine umfassendere Theorie nötig. Experimentell kann entweder direkt mit teilchenphysikalischen Experimenten oder indirekt in Abweichungen von den Vorhersagen des SM nach neuer Physik gesucht werden. So kann jedes BSM-Szenario getestet werden, wobei in dieser Dissertation beide Möglichkeiten betrachtet werden.

In dieser Arbeit werden BSM-Szenarien im Quark- sowie im Leptonen-Sektor und deren phänomenologische Konsequenzen auf messbare Observablen betrachtet. Ein konkretes Beispiel in dieser Dissertation sind sterile Neutrinos, welche Massen im eV-, GeV- oder 10^{12} GeV-Bereich im Kontext symmetrie-erzeugter oder strukturloser Massenmodelle für Neutrinos aufweisen können. Für sterile Neutrinos im GeV-Bereich kann eine eindeutige Hierarchie zwischen Flavour-abhängigem aktiv-sterilen Mischen in den symmetrie-erzeugten Modellen ausgemacht werden, welche als Diskriminator für verschiedene Modelle im Rahmen zukünftiger Experimente dienen können. Sterile Neutrinos im 10^{12} GeV-Bereich können hingegen, kombiniert mit thermischer Leptogenese, die Baryonenasymmetrie zusätzlich zu kleinen Neutrinomassen erzeugen. Als Ergebnis wird entweder eine breite oder schmale Verteilung steriler Neutrinomassen von symmetrie-erzeugten oder anarchischen Modellen für Neutrinomassen vorhergesagt. Anarchische Modelle für Neutrinomassen mit sterilen Neutrinos im eV-Bereich führen entweder zu Flavour-unabhängigen oder Flavour-abhängigen aktiv-sterilen Mischungsverteilungen, abhängig von der in der Untersuchung genutzten Methode.

Ähnlich wie beim Ausnutzen von Symmetrien im Neutrinosektor, kann man Symmetrien auch in Modellen für Quarkmassen nutzen. In dieser Arbeit werden Symmetrien behandelt, die den Cabibbo-Winkel für Quarkmischung in führender Ordnung quantisieren können. Dies führt zu einer Vielzahl möglicher Symmetrien, welche genutzt werden können um spezifische Modelle für Quarkmassen zu entwickeln.

BSM-Physik indirekt mit Hilfe astrophysikalischer Neutrinos zu testen stellt eine Alternative zur direkten Detektion dar, und führt bei Betrachtung der Zusammensetzung des Neutrino-

Flavours zu klaren Abweichungen von den Erwartungen. Zusätzliche Informationen können durch andere Effekte gewonnen werden, was weiter zur Eingrenzung des Parameterraums beiträgt. Neben der Behandlung verschiedenster BSM-Szenarien wird auch das Potenzial zukünftiger Experimente betrachtet, vor Allem im Hinblick auf deren Effektivität Physik jenseits des SM zu testen und zu unterscheiden.

Acknowledgments

This dissertation is the culmination of a journey through the amazing world of physics. Following this path, lead to interaction with many people who I owe my gratitude. First, I would like to thank my supervisor, Walter Winter, for giving me the opportunity to do the research leading to this dissertation. His advice and guidance as well as his support were always welcome. Also, I am grateful to the committee members, who agreed reviewing my dissertation or attending the oral defense, and I have had valuable discussions with them. Big thanks to Robert Brose, Daniel Biehl, Jonas Heinze, Jim Talbert and Ivo Varzielas for proof-reading or giving suggestions to the dissertation. In addition, I should mention Kathrin Mallot with whom I have had a lot of discussions about physics and other related questions. Furthermore, a thanks goes to Heike Prokoph and Maria Krause who helped me with LATEX issues and the layout of the dissertation. I would like to thank the entire astropaticle community in Zeuthen and especially the THAT/NEUCOS group for the countless scientific and social activities they offered to me.

I want to dedicate this dissertation to my beloved family members, grandfather Erik Thomsen, grandmother Kirsten Thomsen, and aunt Birthe Clausen, who sadly passed away during my stay at DESY. I was devastated to hear about their death, and it was a difficult time for me. I will always cherish the memories of them, and they are always missed. My family was supporting and loving throughout the dissertation period, and I am glad for them always standing by my side.

Note: After handing in the thesis, my dear step-grandmother Katrine Hageland passed away. She will be missed, and I will cherish the memories of her.

Contents

Chapter 1

Introduction

The theory of elementary particle physics, dubbed the Standard Model (SM), describes three of four fundamental forces in Nature, namely the electromagnetic, the weak and the strong force. The SM is considered one of the most successful models in modern physics since its predictions are consistently verified by data with only a few compelling anomalies. A major achievement is the joint description of the electromagnetic and the weak forces, leading to the prediction of neutral gauge bosons. Since then, speculations about combining all forces have emerged, but an experimental confirmation is still needed. Another great accomplishment is the discovery of the Higgs boson, explaining the mass generation mechanism for the SM particles (except for neutrinos). However, it is, in general, a problem of the SM that it leaves its parameters undetermined, meaning experimental input is needed to determine them. This mystery leads us to believe that the SM must be considered as an effective theory obtained from the low-energy limit of a more complete theory, in which its parameters can be derived from first principles.

A complete theory must include new physics since there are a number of observations that cannot be explained by the SM. The origin of neutrino masses has emerged as one of the hot topics in particle physics after the observations of neutrino oscillations. Neutrinos were previously thought to be massless according to the SM, but the existence of neutrino oscillations implies massive neutrinos (discussed in detail later). Thus, the explanation of non-zero neutrino mass requires physics beyond the SM. Additionally, the SM is unable to provide a viable dark matter candidate, and it is not capable of describing the baryon asymmetry. At the same time, the SM cannot account for an expanding Universe at an accelerating rate, and gravity is not included at all. Therefore, the SM is extreme successful, yet lack answers for various phenomena. Thus, one must extend the SM to obtain a theoretical model consistent with observations.

Pursuing a complete theory capable of describing fermion masses and mixings from first principles, an underlying mechanism is still not clear. But the hierarchical masses and small mixings exhibited by quarks and charged leptons seem to suggest that mass matrices are organized by some yet-unknown symmetry principles. The discovery of neutrino masses and mixings seem to even complicate the puzzle further since they allow large mixings with a small mass hier-

archy. The first approach uses structured mass matrices originating from symmetries, *e.g.* see Refs. [1–5], meaning one must extend the SM's symmetries. An alternative approach relies on structureless mass matrices [6, 7], and they may originate from a very complicated (unknown) theory. We consider both frameworks (symmetrical and anarchical approaches) to explain the observed fermion mass and mixing values in this dissertation.

An example of BSM physics is sterile neutrinos, *i.e.* they do not participate in weak interactions compared to its light "active" counterpart. Introducing a sterile neutrino, allows to generate a neutrino mass. Due to the sterile neutrinos being singlets under the SM's symmetries, *i.e.* not participating in weak interactions, their masses are free parameters. As a consequence, one can introduce them at any mass scale, leading to a rich phenomenology. This dissertation is intended as an investigation of the roles of sterile neutrinos at different mass scales in the context of neutrino mass models. Beside this specific BSM scenario, there are many other possibilities of physics beyond the SM. We investigate different new physics scenarios in this dissertation, and study its impact on experimental observables.

To test BSM scenarios, various experiments are looking for possible deviations from the SM, either via direct or indirect measurements. The Large Hadron Collider (LHC) is a perfect example since it tests the SM under more extreme conditions (at higher energies). However, the LHC is producing the initial particle beam itself, one could also look toward the sky. Several experiments use particles from the atmosphere and/or the Universe to study new physics scenarios. An example is the IceCube experiment, a giant neutrino telescope, which study the origin of astrophysical neutrinos. All examples above, shows a rich variety in experiments searching for BSM physics, and we discuss specific experiments and how they probe new physics in this dissertation.

The dissertation is structured as follows: in Chapter 2, we discuss mass generation of the fermions. We start with a general discussion about possible mass terms before summarizing the measured fermion mass values. As a consequence of fermion mass, a phenomenon called fermion mixing is possible. We discuss this phenomenon in Chapter 3. We introduce the reader to the main two fermion mass modeling frameworks in Chapter 4, and we discuss the generation of the observed mixing parameters within each framework. We start with the terminology associated with the two frameworks, whereafter we show different models capable of explaining the mixing parameters. In the end of the chapter, we discuss the current status of the fermion mass modeling field. Thereafter in Chapter 5, we introduce three GeV sterile neutrinos in the context of neutrino mass models. We perform both model-independent and model-dependent analyses, and study their predictions of the active-sterile mixing to future experimental sensitivities. Focusing on Cabbibo mixing in th quark sector in Chapter 6, we find symmetries which can generate this observable to leading order. We discuss the possibility of having sterile neutrinos with Grand

Unified Theory (GUT) scale masses in Chapter 7, and we investigate their mass distribution for generating a successful baryon asymmetry in the context of structured and structureless mass matrices. In Chapter 8, we consider eV sterile neutrinos within the framework of structureless mass matrices, and we show the mass and active-sterile mixing distributions. Considering physics beyond the SM, we investigate its impact on the flavor composition of astrophysical neutrinos in Chapter 9. Lastly, we make our final remarks and conclude in Chapter 10.

Chapter 2

Fermion mass generation

With the introduction to the Standard Model and its problems, we consider the fermion mass generation in this chapter. When generating a fermion mass term, two possibilities are possible, depending on the properties of the fermion, and the specific mass terms for the SM fermions are discussed in detail. Thereafter, the discovery of the fermions and their masses are considered, showing the vast difference among the fermion mass values. Additionally, the main proposals for explaining the smallness of the neutrino masses are discussed. However, we start with the basic concept/terminology of fermion mass term generation before going more in-depth with specific details.

2.1 Dirac and Majorana mass terms

A Dirac mass term arises as a result of the Higgs mechanism through the presence of Yukawa couplings of the fermion fields with the Higgs doublet. After electroweak symmetry breaking, the mass term is written as

$$\mathcal{L}_{\text{Dirac}} = \frac{y_\psi v}{\sqrt{2}}\overline{\psi_L}\psi_R + h.c = \frac{y_\psi v}{\sqrt{2}}\overline{\psi}\psi\,, \tag{2.1.1}$$

where v is the Higgs vacuum expectation value, y_ψ is the Yukawa coupling of the fermion ψ, ψ_L (ψ_R) is the left-handed (right-handed) chiral projection of ψ, *i.e.* $\psi_{L,R} = P_{L,R}\psi = 1/2 \cdot (1 \mp \gamma_5)\psi$ using chiral projection operators $P_{L,R} = 1/2 \cdot (1 \mp \gamma_5)$, and the matrix $\gamma_5 = \text{diag}(-1, 1)$. In the SM, the charged fermion obtain its mass via a Dirac term since both the left- and right-handed fermion field are present. However, the Dirac neutrino mass term is forbidden because no right-handed neutrino field exists, meaning the neutrino remains massless.

Note that only the terms $\overline{\psi}_R\psi_L$ and $\overline{\psi}_L\psi_R$ survive in Eq. (2.1.1) since the chiral projection operators $P_{L,R}$ have the properties $P^2_{L,R} = P_{L,R}$, $P_L + P_R = 1$, and $P_L P_R = 0$, meaning $\overline{\psi}_L\psi_L = 0$ and $\overline{\psi}_R\psi_R = 0$. However, there is a second possibility for writing a mass term using $\psi_{L,R}$ alone together with its charge conjugated field $\psi^c_{L,R} = \mathcal{C}\overline{\psi}^T_{L,R}$, where $\mathcal{C}$ is the charge conjugation

matrix. It is a Majorana mass term, and it is written as

$$\mathcal{L}^{L}_{\text{Majorana}} = \frac{v y_{\psi L}}{2\sqrt{2}} \overline{\psi^{c}_{L}} \psi_{L} + h.c. = \frac{v y_{\psi L}}{2\sqrt{2}} \overline{\Psi_{L}} \Psi_{L} \,, \tag{2.1.2}$$

$$\mathcal{L}^{R}_{\text{Majorana}} = \frac{v y_{\psi R}}{2\sqrt{2}} \overline{\psi^{c}_{R}} \psi_{R} + h.c. = \frac{v y_{\psi R}}{2\sqrt{2}} \overline{\Psi_{R}} \Psi_{R} \,, \tag{2.1.3}$$

for the left- and right-handed fermion field, respectively. Here, $y_{\psi L}$ ($y_{\psi R}$) is the Yukawa coupling of the fermion field $\Psi_L = \psi_L + \psi^c_L$ ($\Psi_R = \psi_R + \psi^c_R$), and the Majorana mass matrix is, in general, symmetric, *i.e.* $M^T = M$. A major difference between the Dirac and Majorana mass terms is that the Majorana fields $\Psi_{L,R}$ satisfy the relation $\Psi^c_{L,R} = \Psi_{L,R}$, meaning they are their own antiparticle. Therefore, a Majorana mass term is forbidden for the charged fermions due to their electric charge. However, it is possible for a Majorana neutrino mass term since neutrinos are electrically neutral. To make a Majorana mass term for the left-handed neutrinos renormalizable, one must introduce a weak isospin triplet with hypercharge $Y = 2$ since it follows that $\overline{\psi^c_L}\psi_L$ has hypercharge equal to $Y = -2$. However, the SM lacks the weak isospin triplet, making the mass term forbidden due to the SM $SU(2)\times U(1)$ gauge group. A similar mass term can be written for the right-handed neutrinos (assuming neutrinos being Majorana particles) since they are singlets under the SM symmetries, *i.e.* they do not participate in the electroweak force. Additionally, no weak isospin triplet is needed to construct a Majorana mass term for the right-handed neutrinos.

Specifically for the neutrinos, one can generate an effective Majorana mass term by the dimensional five Weinberg operator [8]

$$\mathcal{L}_{\text{Weinberg}} = \frac{g}{\mathcal{M}} (L^T_L \tau_2 \Phi) \mathcal{C}^{\dagger} (\Phi^T \tau_2 L_L) + h.c. \,, \tag{2.1.4}$$

where g is a gauge coupling, L_L is the lepton doublet, Φ is the Higgs field, and $\mathcal{M}$ is a high-energy mass scale. As a consequence of electroweak symmetry breaking, $\mathcal{L}_{\text{Weinberg}}$ generates a Majorana mass term such as Eq. (2.1.2) with the neutrino mass $m_\nu = gv^2/\mathcal{M}$. The Weinberg operator is unique since it is the only dimension five operator which can generate a neutrino mass. Considering higher dimensional operators, there are a vast amount of operators generating neutrino masses [9]. The Weinberg operator $\mathcal{L}_{\text{Weinberg}}$ is not acceptable in the SM since the SM is made up by dimensional four operators. The Weinberg operator is a dimensional five operator, meaning it is not renormalizable. However, the SM is only an effective low-energy theory of the symmetry breaking of a high-energy unified theory. Hence, it is plausible that there are effective low-energy terms which are non-renormalizable. This approach is analogous to that adopted in the effective non-renormalizable Fermi theory of weak interactions, which is a low-energy manifestation of the SM.

To recap, the charged fermions obtain their masses via a Dirac mass term, which requires the

existence of both the left- and right-handed fermion field. This is prohibited for the neutrinos since the SM lacks the right-handed neutrino field. Furthermore, a Majorana mass term is forbidden for the charged fermions due to their electric charge, whereas it is a possibility for the electrical neutral neutrinos. However, it is excluded due to the SM lacking a weak isospin triplet, meaning the term would violate the SM symmetries. However, one can construct an effective Majorana mass term for the neutrino via the Weinberg operator, but it is non-renormalizable, meaning it is not acceptable in the SM. Therefore, the neutrinos remain massless in the SM, whereas the charged fermions obtain a mass. However, their Yukawa couplings are unknown parameters of the SM, meaning the masses cannot be predicted and must be obtained from experimental measurements.

2.2 Discovery of the fermions and their mass

The first three flavors of quarks (up, down, and strange) were hypothesized to describe the multitude of hadrons (the particle zoo) found in the 1960's[10–12]. The up and down quarks were discovered at the Stanford Linear Accelerator Center (SLAC) by measuring the deep inelastic scattering on protons[13, 14]. Charm quarks were produced almost simultaneously by two teams - one at SLAC, and one at Brookhaven. The charm quarks were observed, bound together with charm antiquarks in mesons. The two teams had assigned the discovered meson two different symbols, thus it became formally known as the J/ψ meson [15, 16]. The bottom quark was observed at Fermilab[17], making it a strong indicator of the top quark's existence. Without the top quark, the bottom quark would have no partner. The top quark was discovered at Fermilab by the CDF[18] and DØ[19] experiments. The current measurements of the quark masses are summarized as [20]

$$m_u = 2.2 \pm 0.5 \text{ MeV}, \quad m_c = 1.28 \pm 0.03 \text{ GeV}, \quad m_t = 173.1 \pm 0.6 \text{ GeV}, \tag{2.2.1}$$

$$m_d = 4.7 \pm 0.5 \text{ MeV}, \quad m_s = 96 \pm 6 \text{ MeV}, \quad m_b = 4.18 \pm 0.03 \text{ GeV}. \tag{2.2.2}$$

The electron was discovered by J.J. Thomson in 1897[21], whereas the electron neutrino was postulated by Wolfgang Pauli to preserve conservation of energy in beta decay [22]. The electron neutrino was discovered in 1956 by measuring the inverse beta decay using the neutrino flux coming from a nuclear reactor[23]. The muon was discovered in 1936, however it was first thought to be a meson, but eventually it was reclassified as a lepton since it did not undergo strong interactions[24, 25]. With two charged and one neutral lepton, it was interesting whether there existed a neutrino associated with the muon or not. However in 1962, it was showed that a muon neutrino existed by detecting its interactions[26]. The tau lepton was detected in

different experiments at SLAC[27], and it was expected to have an associated neutrino. The tau neutrino was discovered by the DONUT experiment at Fermilab in 2000[28], completing the three generation of leptons - similar to the quarks. The charged lepton masses are (uncertainties on the electron and muon mass are less than 10^{-6} - therefore, it is not displayed) [20]

$$m_e = 0.51 \text{ MeV}, \quad m_\mu = 105.66 \text{ MeV} \quad \text{and} \quad m_\tau = 1776.86 \pm 0.12 \text{ MeV}\,, \tag{2.2.3}$$

whereas we have no definite information about the neutrino mass. Even though the neutrino is predicted to be massless in the SM, there is clear evidence from neutrino oscillation experiments that the neutrino is massive (discussed in detail later). Other experiments provide additional information about neutrino mass, but there exist only upper limits at this time. Cosmology is sensitive to the sum of neutrino masses since the neutrinos contribute to the energy density of the Universe via $\Omega_\nu h^2 = \sum m_\nu/(94.14 \text{ eV})$. From the Planck measurement of the neutrino contribution to the energy density $\Omega_\nu h^2 < 0.0076$, we obtain the upper limit $\sum m_\nu < 0.72$ eV [29]. At the same time, we do not know the absolute neutrino mass scale, and one can determine it by measuring the end spectrum of the electron in the tritium beta decay process. The spectrum is given by [30]

$$\frac{d\Gamma_F}{dE_e} \simeq \frac{G_F^3}{2\pi^3}|\mathcal{M}|^2 F(Z, R_e, E_e) p_e E_e (E_e^{\max} - E_e)\sqrt{(E_e^{\max} - E_e)^2 - m_\beta^2}\,, \tag{2.2.4}$$

where G_F is the Fermi constant, p_e, E_e, and $E_e^{\max}$ are the momentum, energy, and maximum endpoint energy, respectively, of the electron, $F(Z, R_e, E_e)$ is the Fermi function capturing the correction due to the Coulomb interactions of the electron, $|\mathcal{M}|^2 \sim 5.3$ is the absolute square of the nuclear matrix element, and the observable is $m_\beta^2 = \sum_i |U_{ei}|^2 m_i^2$. As seen from Eq. (2.2.4), the neutrino mass distort the end spectrum, meaning one can obtain a limit. The current upper limit is $m_\beta < 2$ eV [31], whereas the KATRIN experiment is suppose to improve this limit by an order of magnitude, *i.e.* $m_\beta < 0.2$ eV. Specific for Majorana neutrinos, a process called neutrinoless double beta decay is possible. Here, two neutrons in a nuclei decay simultaneously, producing two protons, two electrons, and two electron antineutrinos. Since the neutrino is its own antiparticle in the case of Majorana neutrinos, the two antineutrinos can annihilate. This leaves two protons and two electrons, meaning no neutrinos are present in the end. For this process, the inverse of the half-life can be written as [32]

$$(T_{1/2}^{0\nu})^{-1} = G^{0\nu}|M^{0\nu}|^2 \left(\frac{m_{\beta\beta}}{m_e}\right)^2\,, \tag{2.2.5}$$

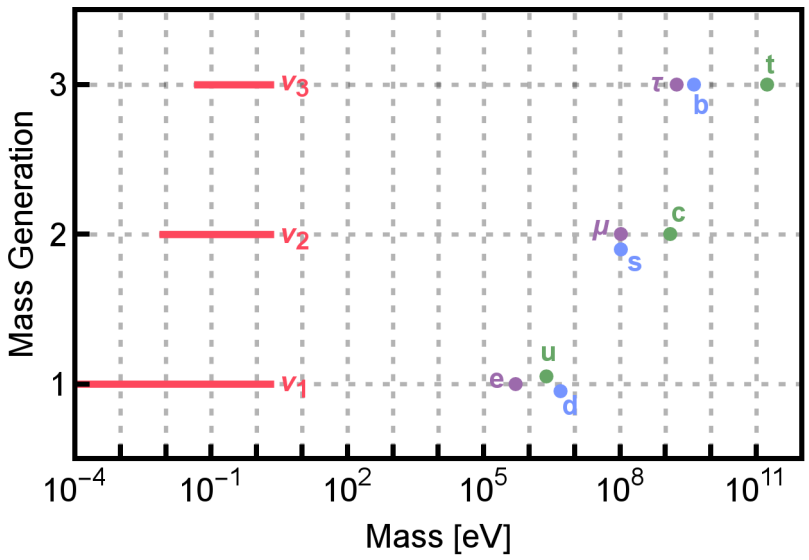

Figure 2.1: Schematic showing the mass hierarchies for each fermion mass generation. The charged fermion masses are given by points since they are experimentally measured, whereas there are only upper limits on the neutrino masses, meaning to the allowed neutrino mass range is represented by the red line. This is the specific case of neutrinos with normal ordered masses, *i.e.*$m_1 < m_2 < m_3$.

where $G^{0\nu}$ is a phase-space factor, $M^{0\nu}$is the nuclear matrix element, and m_e is the electron mass. The observable is given by $m_{\beta\beta} = |\sum_i U_{ei}^2 m_i|$, and the current upper limit is $m_{\beta\beta} < (0.2 - 0.4)$ eV [33]. There are plans of constructing experiments which are suppose to improve this limit by an order of magnitude, and the long term goal is setting the limit $m_{\beta\beta} < 0.01$ eV. All of the limits point toward the neutrino being much lighter than the charged fermions, and there must be some explanation behind this.

2.3 Smallness of neutrino mass

In Fig. 2.1, the fermion masses are shown. The charged fermions are all within one to two orders of magnitude from each other for each generation, whereas there is a huge gap from the charged fermions down to the neutrinos. The four main proposals explaining the smallness of neutrino masses are:

- The seesaw mechanisms [34–46]
- R-parity violating supersymmetry [47–53]
- TeV scale loop mechanisms [54–59]

- Extra dimensions [60–63]

A possible neutrino mass generation is the seesaw mechanism, and its starting point is the dimension five operator in Eq. (2.1.4). The seesaw mechanism of type I [34–38] introduces sterile (right-handed) neutrinos, and it assumes they are Majorana particles. This means the neutrino mass Lagrangian is given by [64]

$$\mathcal{L} = \frac{1}{2}\begin{pmatrix}\overline{\nu_L} & \overline{\nu_L^c}\end{pmatrix}\begin{pmatrix}0 & m_D\\ m_D^T & M_R\end{pmatrix}\begin{pmatrix}\nu_R^c\\ \nu_R\end{pmatrix} + \text{h.c.}\,, \tag{2.3.1}$$

with the additional assumption $m_D \ll M_R$, decoupling the mass scales of the active (left-handed) and sterile neutrinos. One must write all possible mass terms, and since it is assumed the neutrinos are Majorana particles, both Dirac and Majorana mass terms appear. However, the upper left matrix is zero since the Lagrangian has to be $SU(2)$ invariant. Diagonalizing the mass matrix in Eq. (2.3.1), gives the effective neutrino mass matrices of the active and sterile neutrinos

$$m_\nu = -m_D M_R^{-1} m_D^T \quad \text{and} \quad M_N = M_R\,, \tag{2.3.2}$$

respectively. Here, the smallness of the light neutrino masses are explained by the heaviness of the sterile neutrino masses. Since the sterile neutrino is a singlet under the SM's symmetries, means an arbitrary number of sterile neutrinos can be added, and, additionally, the overall scale of M_R is, in general, unknown. However, the seesaw mechanism of type I was firstly discuss in the context of Grand Unified Theories (GUT) [34–38], meaning the sterile neutrinos would have masses of 10^{16} GeV. As a consequence, the neutrino Yukawa couplings are of order one, satisfying the requirement of having a perturbative field theory. However, the sterile neutrino masses are not bound to the GUT scale, and the allowed (but rather large) range in the seesaw mechanism is in the interval $[10^{-10}, 10^{16}]$ GeV [65]. It is bound due to having a perturbative field theory and obeying the experimental limits on the neutrino masses. Due to the large mass range, one can introduce an arbitrary number of sterile neutrinos with different masses in the seesaw mechanism, and we consider different examples in the dissertation. There are other variants of the seesaw mechanism with different types of mediator, namely the seesaw mechanism of type II (type III) introduces scalar triplets (fermion triplets), whereas the inverse seesaw mechanism introduces six fermion singlets (three singlets are usually associated as sterile neutrinos, whereas the other three are new singlet states).

A different scenario for neutrino mass generation is R-parity violating supersymmetry (SUSY), where the new quantum number (R-parity) is defined as $R = (-1)^{3B+L+2S}$ with L, B, and S being lepton number, baryon number, and spin, respectively. Introducing supersymmetric particles (sparticles) together with the SM particles, means R-parity violating interactions in

the superpotential can contribute to neutrino mass. The relevant part of the superpotential is given by [66]

$$W = \left[\frac{1}{2}\lambda_{ijk}\hat{L}_i\hat{L}_j\hat{E}^c_k + \lambda'_{ijk}\hat{L}_i\hat{Q}_j\hat{D}^c_k + \epsilon_i\hat{L}_i\hat{H}_u\right], \tag{2.3.3}$$

where $\hat{Q}_i, \hat{U}^c_i, \hat{D}^c_i$ are the quark superfields, $\hat{L}_i, \hat{E}^c_i$ are lepton superfields, $\hat{H}_u$ is the Higgs superfields, and $\lambda, \lambda', \epsilon_i$ are R-parity violating Yukawa couplings. This potential leads to mixing between neutrinos and neutralinos (a hypothetical sparticle), and it induces a low energy-scale seesaw-like mechanism for the neutrino masses. Here, the neutrino masses are suppressed by the Minimal Supersymmetric Standard Model (MSSM) neutralino mass matrix. The Large Hadron Collider (LHC) searches for TeV scale neutralinos, thereby constraining or excluding parts of the parameter space.

There are many non-SUSY loop models capable of generating neutrino masses, and they extend the scalar sector with either double-charged, single-charged or neutral particles, meaning the general Lagrangian can be written as [67]

$$-\mathcal{L} = f_{ij}H^{++}\ell_i\ell_j + g_{ij}H^+\ell_i\nu_j + h_{ij}H^0\nu_i\nu_j + h.c.\,. \tag{2.3.4}$$

Four specific examples are the left-right symmetric model, the Higgs triplet model, the Zee model, and the Babu model, and all provide TeV-scale mechanisms of neutrino mass generation consistent with current data. New particle discovery (such as new scalar or gauge bosons $Z', W', H^{\pm\pm}, H^{\pm}, h^0$) at the LHC is also possible if they are within experimentally reach, and the Yukawa couplings can induce lepton-flavor violating decays ($\mu \to eee$, $\mu \to e\gamma$), which can probe these models further.

There are a number of neutrino mass models with extra dimensions, and they are (usually) constructed within string theories. An useful relation between the string mass scale M_S and the four-dimensional Planck mass M_P is $M_P^2 = 8V_bM_s^2/g^4$, where g is the SM gauge coupling, and V_b is the volume of the bulk. The model localizes the SM on the brane, whereas fermion singlets can propagate in the bulk. As a result, the Dirac neutrino mass is given by $m_\nu^{\text{Dirac}} \simeq \lambda v/\sqrt{V_b} \simeq \sqrt{8}\lambda v M_s/(g^2M_P)$, where v is the Higgs VEV, and λ is the interaction strength among the sterile neutrino, the Higgs and lepton doublet. Therefore, neutrino masses are naturally suppressed by the bulk volume V_b, and current experimental data allows for a string scale at the TeV range, making it experimentally accessible for the LHC to test this scenario. However, one can adjust the theory parameters in this model to satisfy experimental data since the parameters are in general unknown.

To recap, there is a mass gap between the neutrinos and the charged fermions of, at least, six orders of magnitude, meaning a more complete theory of elementary particle physics must

account for this. There are many different and phenomenological interesting scenarios, even though we described the four main proposals only. Most of them introduces a heavy mediator, which, when integrated out, leads to the suppression of the neutrino masses, and the type of mediator (fermion or boson) depends on the specific model. Introducing extra spatial dimensions, means the neutrino mass is suppressed by the bulk volume due to the singlets being able to propagate off the brane into the extra dimensions. Nevertheless of the particular model, massive neutrinos mean BSM physics, and a consequence of massive neutrinos is neutrino oscillations, which is discussed in the next chapter.

Chapter 3

Fermion mixing

With the discussion about fermion mass generation, their experimental measured mass values, and the smallness of the neutrino masses, one might study the consequence of introducing massive fermions. Starting with the charged-current fermion production process, one finds that the fields with definite flavor are not equal to the fields with definite mass. As a consequence, it leads to fermion flavor transitions. Experimentally, one studies this phenomenon for both the quarks and leptons, and as a result, two quite different mixing patterns emerge. There is no final explanation for this, and it intrigues even more excitement among physicists. Therefore, it is important to discuss the phenomenon in more in-depth details.

3.1 Charged current interactions of fermions

The fermion flavor eigenstates are produced in charged-current (CC) weak interaction processes, and this interaction is govern by the Lagrangian

$$\mathcal{L}_{CC} = -\frac{g}{2\sqrt{2}} j^{\rho} W_{\rho} + h.c.\,, \tag{3.1.1}$$

where g is the gauge coupling, W_ρ is the W-boson field, and j^ρ is the fermion charged current

$$j^{\rho} = 2\overline{\psi'_L}\gamma^{\rho}\phi'_L \tag{3.1.2}$$

with the left-handed fermion fields ψ'_L and ϕ'_L. However, the Yukawa matrices associated with the fermion fields ψ'_L and ϕ'_L are, in general, nondiagonal, meaning the primed fields do not have definite masses. Therefore, it is necessary to diagonalize the Yukawa matrices by the transformations

$$U_L^{\psi\dagger} Y'^{\psi} U_R^{\psi} = Y^{\psi}\,, \quad U_L^{\phi\dagger} Y'^{\phi} U_R^{\phi} = Y^{\phi}\,, \tag{3.1.3}$$

and this basis-transformation gives the fermion fields $\psi_L = U_L^{\psi\dagger}\psi'_L$ and $\phi_L = U_L^{\phi\dagger}\phi'_L$ with definite masses. This shows the fermion flavor eigenstates are not necessarily equal to the fermion mass

eigenstates, and as a consequence, the fermion charged current becomes

$$j^\rho = 2\overline{\psi_L} U_L^{\psi\dagger} \gamma^\rho U_L^\phi \phi_L = 2\overline{\psi_L} U_L^{\psi\dagger} U_L^\phi \gamma^\rho \phi_L \,. \tag{3.1.4}$$

By convention, one chooses a basis where one of the fermion fields has a diagonal Yukawa matrix, whereas one projects $U = U_L^{\psi\dagger} U_L^\phi$ on the other fermion field. This leads to the phenomenon called *fermion mixing*, meaning the fermion changes its flavor from one generation to an other due to the mixing matrix U. In the context of quark mixing, one can substitute $\psi_L = q_L^U$ and $\phi_L = q_L^D$ for the up-type and down-type quarks, respectively, and one chooses the basis with a diagonal up-type Yukawa matrix. As a consequence, the down-type quarks changes its flavor in hadron decays. In the context of lepton mixing, no mixing should occur since the neutrino is predicted to be massless, meaning Eq. (3.1.3) is ill-defined. However, as we will discuss later in detail, experimental evidence shows the neutrino is massive. Therefore for the further discussion, one can replace $\psi_L = \ell_L$ and $\phi_L = \nu_L$ for the charged and neutral leptons, respectively, and one chooses a basis with a diagonal charged lepton Yukawa matrix, meaning neutrinos mix or rather oscillate (flavor transitions varying with time/distance). One might think charged leptons can mix, since it is a matter of convention seen from Eq. (3.1.4). However, it is not possible since the charged lepton flavor is defined by the mass of the charged lepton; the only property that distinguishes them because they have similar interactions with same coupling strength. Therefore, one measures flavor through mass by applying kinematical cuts or investigating their decay products, meaning charged leptons are defined as mass eigenstates, and cannot undergo flavor mixing.

The flavor eigenstates are related to the mass eigenstates by the mixing matrix U, and it is a product of two unitary matrices, which diagonalizes the Yukawa matrices. In the quark (lepton) sector, it is given by $U_{\text{CKM}} = U_u^\dagger U_d$ ($U_{\text{PMNS}} = U_\ell^\dagger U_\nu$), and it is dubbed the CKM (PMNS) mixing matrix. For Dirac particles, *i.e.* quarks and Dirac neutrinos, the mixing matrix is parameterized as

$$U_{\text{CKM/PMNS}}^{\text{Dirac}} = \begin{pmatrix} c_{12}c_{13} & s_{12}c_{13} & s_{13}e^{-i\delta} \\ -s_{12}c_{23} - c_{12}s_{23}s_{13}e^{i\delta} & c_{12}c_{23} - s_{12}s_{23}s_{13}e^{i\delta} & s_{23}c_{13} \\ s_{12}s_{23} - c_{12}c_{23}s_{13}e^{i\delta} & -c_{12}s_{23} - s_{12}c_{23}s_{13}e^{i\delta} & c_{23}c_{13} \end{pmatrix}, \tag{3.1.5}$$

where $c_{ij} = \cos(\theta_{ij})$ and $s_{ij} = \sin(\theta_{ij})$. For Majorana neutrinos, it is given by $U_{\text{PMNS}}^{\text{Majorana}} = U_{\text{PMNS}}^{\text{Dirac}} \cdot \text{diag}(1, e^{i\alpha}, e^{i\beta})$. The mixing matrix depends on three mixing angles θ_{12}, θ_{23}, and θ_{13}, which, by convention, are allowed in the interval $\theta_{ij} \in [0, \pi/2]$. Additionally, the mixing matrix depends on a CP-violating phase, which tells whether there is a difference or not between particles and antiparticles, and its allowed range is $\delta \in [0, 2\pi]$. For Majorana neutrinos, the

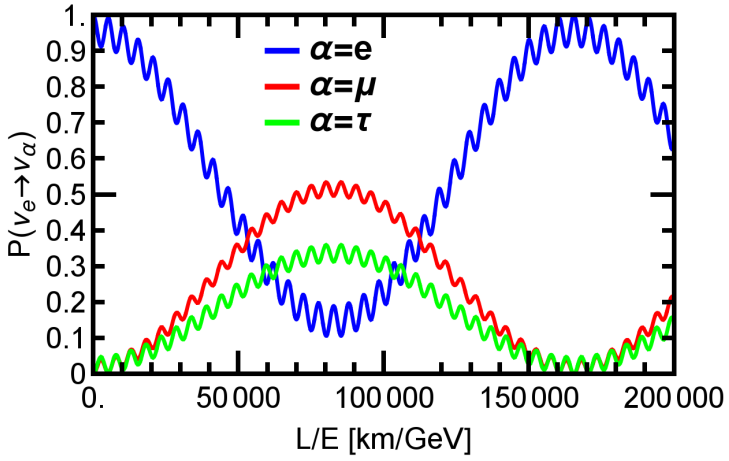

Figure 3.1: Oscillation probability for an initial electron neutrino to oscillate into an electron (blue curve), muon (red curve) or tau (green curve) neutrino as a function of baseline over energy.

additional phases (α and β) in $U_{\text{PMNS}}^{\text{Majorana}}$ appear as a consequence of less freedom since the particle field have to be equal to the antiparticle field, *i.e.* $\nu = \nu^c$. However, the additional phases are irrelevant for neutrino oscillations, but important for neutrinoless double beta decay. Whether neutrinos are Dirac or Majorana particles, they undergo neutrino oscillations, and the probability for a transition is studied next in the context of vacuum and matter oscillations.

3.2 Neutrino oscillations

In the standard theory of neutrino oscillations, the flavor eigenstate is related to the mass eigenstate via

$$|\nu_\alpha\rangle = \sum_i U_{\alpha i}^* |\nu_i\rangle \,, \tag{3.2.1}$$

where U is the mixing matrix, and one requires the neutrino states are forming an orthonormal basis, *i.e.* $\langle\nu_\alpha|\nu_\beta\rangle = \delta_{\alpha\beta}$. The massive neutrino states $|\nu_i\rangle$ are eigenstates of the Hamiltonian, $\mathcal{H}|\nu_i\rangle = E_i|\nu_i\rangle$, and its time-dependence is govern by the Schrödinger equation, $i\frac{d}{dt}|\nu_i(t)\rangle = \mathcal{H}|\nu_i(t)\rangle$, implying it evolve as $|\nu_i(t)\rangle = e^{-iE_it}|\nu_i\rangle$ in time. Therefore, the time-dependent flavor eigenstate is

$$|\nu_\alpha(t)\rangle = \sum_i U_{\alpha i}^* |\nu_i(t)\rangle = \sum_i U_{\alpha i}^* e^{-iE_it} |\nu_i\rangle \,. \tag{3.2.2}$$

With this at hand, the amplitude of $\nu_\alpha \to \nu_\beta$ transitions are

$$A_{\nu_\alpha \to \nu_\beta}(t) \equiv \langle \nu_\beta | \nu_\alpha(t) \rangle = \sum_i U^*_{\alpha i} U_{\beta i} e^{-iE_i t} \,, \tag{3.2.3}$$

whereas the probability is given by

$$P_{\nu_\alpha \to \nu_\beta}(t) \equiv |A_{\nu_\alpha \to \nu_\beta}(t)|^2 = \sum_{i,j} U^*_{\alpha i} U_{\beta i} U_{\alpha j} U^*_{\beta j} e^{-i(E_i - E_j)t} \,. \tag{3.2.4}$$

For ultrarelativistic neutrinos, it follows $E_i \simeq E + m_i^2/(2E)$ with E being the mean neutrino energy, and in this case, $E_i - E_j \simeq \Delta m^2_{ij}/(2E)$ with $\Delta m^2_{ij} = m_i^2 - m_j^2$. Additionally, ultrarelativistic neutrinos propagate almost at the speed of light, meaning it is possible to approximate the time t with the baseline L, *i.e.* $t = L$. Therefore, we obtain the vacuum neutrino oscillation probability

$$\begin{aligned} P(\nu_\alpha \to \nu_\beta) = \delta_{\alpha\beta} &- 4 \sum_{i>j=1}^{3} \mathrm{Re}[U_{\alpha i} U^*_{\beta i} U^*_{\alpha j} U_{\beta j}] \sin^2\left(\frac{\Delta m^2_{ij} L}{4E}\right) \\ &\pm 2 \sum_{i>j=1}^{3} \mathrm{Im}[U_{\alpha i} U^*_{\beta i} U^*_{\alpha j} U_{\beta j}] \sin\left(\frac{\Delta m^2_{ij} L}{2E}\right) \,, \end{aligned} \tag{3.2.5}$$

where the plus (minus) sign is used for (anti)neutrino oscillations. The mixing matrix gives the amplitude of the oscillation, whereas the mass square differences stands for the oscillatory part of the probability. Massless neutrinos would lead to $\Delta m^2 = 0$, meaning no oscillations would occur, and therefore, Eq. (3.2.5) shows directly that massive neutrinos lead to neutrino oscillations in accordance with experimental evidence.

Neutrino oscillation experiments have provided compelling evidence for the existence of neutrino oscillations by studying neutrinos from various sources such as the Sun, the atmosphere, reactors, and accelerators. From a global analysis of the neutrino oscillation data, one obtains the mass square differences [68]

$$\Delta m^2_{21} = (7.50 \pm 0.18) \cdot 10^{-5} \text{ eV}^2 \,, \quad |\Delta m^2_{32}| = (2.52 \pm 0.04) \cdot 10^{-3} \text{ eV}^2 \,, \tag{3.2.6}$$

however this does not tell us whether all neutrinos are massive or one remains massless. This is direct proof of neutrinos being massive, meaning one must go beyond the SM to describe neutrino oscillations. Additionally, the mixing angles are [68]

$$\theta^\nu_{12} = 33.56^\circ \pm 0.76^\circ \,, \quad \theta^\nu_{23} = 41.6^\circ \pm 1.3^\circ \,, \quad \theta^\nu_{13} = 8.46^\circ \pm 0.15^\circ \,, \tag{3.2.7}$$

which provides large off-diagonal mixing elements in the PMNS mixing matrix. A pictorial example is displayed in Fig. 3.1, showing the probability of an electron neutrino to oscillate as a function of the baseline over energy. Some of the parameters in the neutrino sector are still unknown, namely the mass ordering ($\Delta m^2_{32} > 0$ for normal ordering (NO) or $\Delta m^2_{32} < 0$ for inverted ordering (IO)), the absolute mass scale, the octant of θ_{23} (whether $\theta_{23} < 45°$ (lower octant) or $\theta_{23} > 45°$ (higher octant)) and the value of the CP-violating Dirac phase δ^{lepton} (and α, β if neutrinos are Majorana particles). It is the task for future experiments to measure these unknown observables, and we discuss a particular example later. Regardless, it is clear that the lepton sector exhibit large and non-hierarchical mixings. Beside the neutrino oscillation parameters, one can consider the unitarity of the PMNS matrix. One must measure the mixing elements individually, thereby overconstraining the PMNS mixing matrix. As shown in Ref. [69], there is a lot of potential for improvement, especially in the muon and tau sectors. There are three independent measurements from the electron neutrino sector, namely short-baseline reactor (long-baseline reactor) [solar] experiments are sensitive to $|U_{e3}|^2$ ($|U_{e1}|^2$) [$|U_{e2}|^2$]. These elements are measured to a high accuracy, meaning electron neutrino oscillations do not improve the unitarity bounds further. In the muon and tau sectors, it is more difficult since short- and medium-baseline accelerator experiments cannot measure the mixing elements independently due to degeneracies in the oscillation probability, *i.e.* they measure the combination $|U_{\mu 1}|^2 + |U_{\mu 2}|^2$ [69]. Nevertheless, measuring muon and tau neutrino oscillations can still improve the level of unitarity by the amount of data collected, meaning the allowed range for the mixing elements will shrink. Therefore, there is still a lot of room for new physics to enter in the neutrino sector without being affected by the unitarity bounds of the PMNS matrix.

Coming from the discussion regarding the current experimental status of the neutrino sector, one might investigate neutrino oscillations in a different environment. Neutrino oscillations in matter differ from vacuum oscillations due to the charged current interaction between the electron and electron neutrino in ordinary matter. In vacuum, the oscillation probability is always small for small mixing angles, however matter effects can enhance neutrino mixings since it can be close to unity even if the vacuum mixing angle is small. This manifestation of matter effects on neutrino oscillations is the Mikheyev-Smirnov-Wolfenstein (MSW) effect [70–72]. Matter effects are important when the matter potential V_α becomes comparable or larger than $\Delta m^2/2E$, meaning neutrino oscillations are strongly affected. We consider a simple case of two flavor mixing to easily visualize the main difference between oscillations in vacuum and matter. In this case, the oscillation probability in matter can be written analogously to the one

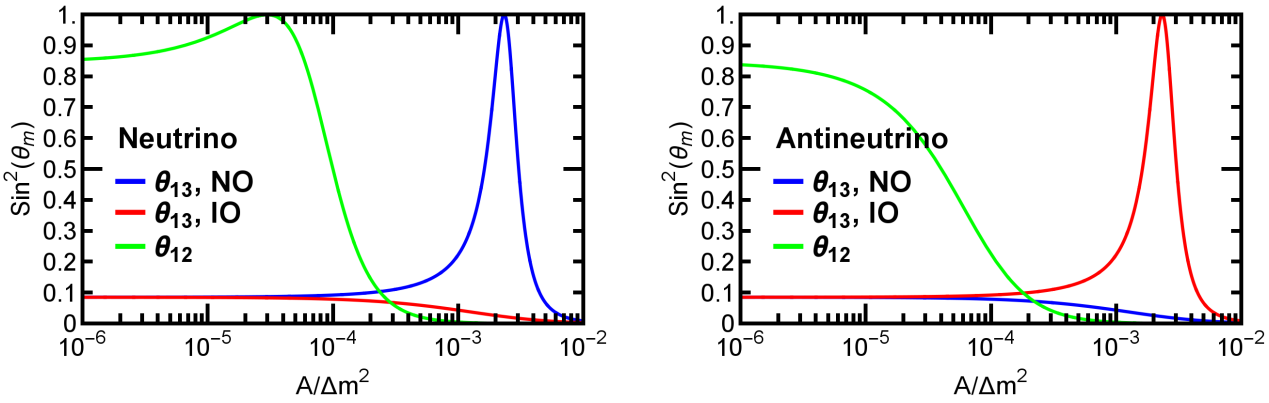

Figure 3.2: Effective mixing angle in matter as a function of matter density. Three cases are displayed, namely the mixing angle θ_{12} (green curve), the mixing angle θ_{13} for normal ordering ($\Delta m^2_{32} > 0$ - blue curve) and the mixing angle θ_{13} for inverted ordering ($\Delta m^2_{32} < 0$ - red curve). The plot to the left (right) shows the behavior of the mixing angles in the neutrino (antineutrino) sector.

in vacuum

$$P_m(\nu_\alpha \to \nu_\beta) = \sin^2(2\theta_m)\sin^2\left(\frac{\Delta m^2_m L}{4E}\right), \quad P_m(\nu_\alpha \to \nu_\beta) = 1 - P_m(\nu_\alpha \to \nu_\beta), \tag{3.2.8}$$

where E is the energy, L is the baseline, and θ_m (Δm^2_m) is the mixing angle (mass squared difference) in matter. The matter oscillation parameters are related to the vacuum oscillation parameters by $\sin(2\theta_m) = \sin(2\theta)/\gamma$ and $\Delta m^2_m = \Delta m^2 \gamma$ with

$$\gamma = \sqrt{\left(\cos(2\theta) \mp \frac{A}{\Delta m^2}\right)^2 + \sin^2(2\theta)}\,, \tag{3.2.9}$$

where $A = 2\sqrt{2} G_F N_e E$, G_F is the Fermi coupling, and N_e is the electron number matter density. The plus (minus) sign in Eq. (3.2.9) is valid for (anti)neutrinos since they do not experience the same matter potential. Note already that it allows the possibility of maximal mixing in matter $\sin(2\theta_m) \simeq 1$, even for small $\sin(2\theta)$.

One can determine the sign of the mass square differences using matter effects by investigating the resonance effect occurring in the neutrino or antineutrino sector. If one chooses the convention $\cos(2\theta) > 0$, there is a resonance for neutrinos if $\Delta m^2 \equiv \Delta m^2_{ij} > 0$, whereas the resonance occurs for antineutrinos when $\Delta m^2 < 0$. Therefore, for a given sign of Δm^2, either neutrinos or antineutrinos (but not both) can experience the resonantly enhanced oscillations in matter,

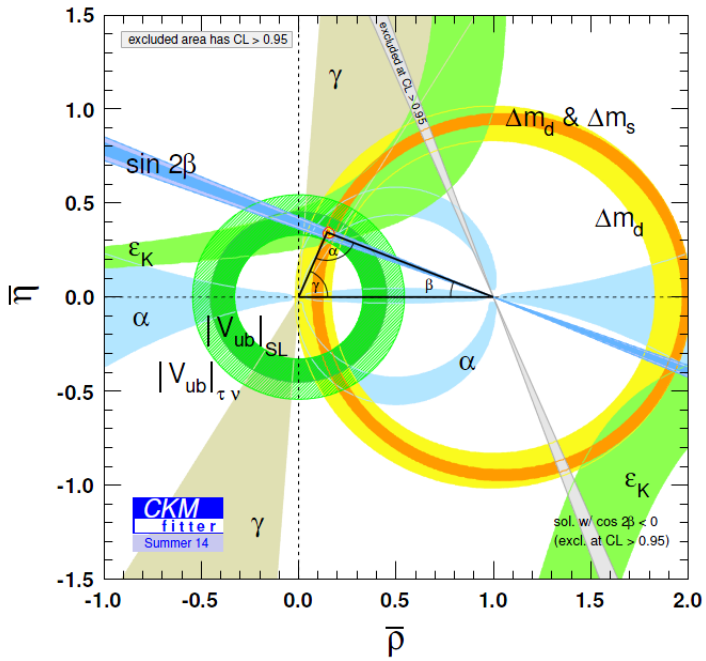

Figure 3.3: Combined fit of experimental constraints in the $\bar{\rho} - \bar{\eta}$ parameter space. The best-fit is $(\bar{\rho}, \bar{\eta}) \simeq (0.1, 0.3)$, leading to the solid triangle. This determines the level of unitarity of the CKM matrix, thereby constraining the three phases α, β, and γ. Figure taken from Ref. [73].

meaning one can determine the heavier mass eigenstate. In Fig. 3.2, the behavior of different mixing angles in matter as a function of the matter potential are shown with the left (right) plot being for (anti)neutrinos. We know the solar mass square difference is positive, *i.e.* $\Delta m^2_{21} > 0$, therefore a resonance occurs for θ_{12} in the neutrino sector. We do not know the sign of $|\Delta m_{32}|^2$, which means two possibilities for $\theta_{13,m}$ are possible. Evidently, there is a resonance for θ_{13} in the neutrino sector when the mass ordering is normal, whereas it occurs in the antineutrino sector for inverted mass ordering. Therefore, it is possible for future experiments such as DUNE and Hyper-Kamiokande to determine the sign of $|\Delta m_{32}|^2$ using matter effects.

After considering neutrino oscillations and the experimental evidence in this sector, it is interesting to investigate whether quarks exhibit the same mixing pattern as neutrinos or they behave differently. Therefore, we turn to quark mixing, and discuss its current experimental status.

3.3 Quark mixing

Quarks interact via the strong interaction in addition to the electroweak force, and as a consequence, they are confined within the nucleus due to asymptotic freedom[74, 75]. Due to their confinement, it is called quark mixing, not quark oscillations, since no oscillations are experimental observed. Therefore, one cannot write a quark oscillation probability in similar fashion as in the neutrino case. However, the quarks mix with each other, meaning flavor transitions occurs in hadron decays, and it plays an important role in flavor physics.

One can perform many different measurements of the CKM mixing elements, depending on method used and decay channel[20]. Considering the mixing element $|U_{ud}|$, one can measure it by studying $0^+ \to 0^+$ nuclear beta decays, from the neutron lifetime or via the decay $\pi \to \pi^0 e\nu_e$, obtaining a combined value $|U_{ud}| = 0.97425 \pm 0.00022$. The mixing element $|U_{us}|$ is measured in semileptonic/leptonic kaon decays or hadronic tau lepton decays, meaning a value $|U_{us}| = 0.2253 \pm 0.0008$ is obtained. The mixing element $|U_{ub}|$ is determined from the process $B \to X_u \ell\nu_\ell$, where X_u is a hadron containing a up quark. However, it is difficult to extract th mixing element $|U_{ub}|$ from this process due to the large background coming from the process $B \to X_c \ell\nu_\ell$, which is sensitive to $|U_{cb}|$. Therefore, one applies kinematical cuts to reduce background and use other processes such as $B \to \pi\ell\nu_\ell$ and $B \to \tau\nu_\tau$ to determine $|U_{ub}|$, thereby obtaining a combined value $|U_{ub}| = (4.13 \pm 0.49) \cdot 10^{-3}$. The magnitude of U_{cd} comes from the production of charm mesons in (anti)neutrino interactions or from semileptonic charm meson decays, leading to the determination $|U_{cd}| = 0.225 \pm 0.008$. Information about the element $|U_{cs}|$ comes from semileptonic D or leptonic D_s decays, resulting in the value $|U_{cs}| = 0.986 \pm 0.016$. Semileptonic B decays with a charmed meson in the final state are sensitive to $|U_{cb}|$, and one extracts the result $|U_{cb}| = (41.1 \pm 1.3) \cdot 10^{-3}$. The mixing elements $|U_{td}|$ and $|U_{ts}|$ are determined by measuring the oscillation frequency of B^0 and B_s^0 mesons, resulting in the values $|U_{td}| = (8.4 \pm 0.6) \cdot 10^{-3}$ and $|U_{ts}| = (40.0 \pm 2.7) \cdot 10^{-3}$. Lastly, the element $|U_{tb}|$ is determined by top decays, and result implies $|U_{tb}| = 1.021 \pm 0.032$. Given the measurements of the magnitude of the mixing matrix elements, one needs to determine three phases coming from the unitarity condition of the CKM mixing matrix, *i.e.* $\sum_\alpha U_{\alpha i}^* U_{\alpha j} = \delta_{ij}$ and $\sum_i U_{\alpha i} U_{\beta i}^* = \delta_{\alpha\beta}$. The three phases are given by

$$\beta = \phi_1 = \arg\left(-\frac{U_{cd}U_{cb}^*}{U_{td}U_{tb}^*}\right), \quad \alpha = \phi_2 = \arg\left(-\frac{U_{td}U_{tb}^*}{U_{ud}U_{ub}^*}\right), \quad \gamma = \phi_3 = \arg\left(-\frac{U_{ud}U_{ub}^*}{U_{cd}U_{cb}^*}\right), \tag{3.3.1}$$

and they lead to CP violation in hadron decays. All of the phases can be extracted by measuring the CP violation in B decays, and the world average result is $\alpha = 85.4^\circ \pm 4.0^\circ$, $\sin 2\beta = 0.682 \pm 0.019$, and $\gamma = 68.0^\circ \pm 8.0^\circ$.

Making a combined global fit to all flavor physics data, one obtains Fig. 3.3. It represents the allowed parts in the $\bar{\eta} - \bar{\rho}$ parameter space (colored regions), where $\bar{\eta}, \bar{\rho}$ are parameters used in the Wolfenstein parameterization of the CKM mixing matrix. Determining the overlapping region, one finds the best-fit point of $\bar{\rho}$ and $\bar{\eta}$, namely $(\bar{\rho}, \bar{\eta}) \simeq (0.1, 0.3)$. This makes one able to determine the phases α, β, and γ by the triangle seen in Fig. 3.3. Beside this, one can determine the four mixing parameters in the CKM matrix, and they are given by [20]

$$\theta_{12}^{\mathrm{q}} = 13.04^\circ \pm 0.05^\circ\,,\ \theta_{23}^{\mathrm{q}} = 2.38^\circ \pm 0.06^\circ\,,\ \theta_{13}^{\mathrm{q}} = 0.201^\circ \pm 0.011^\circ\,,\ \delta^{\mathrm{q}} = 1.20 \pm 0.08\ \mathrm{rad}\,. \quad (3.3.2)$$

Inserting this into the CKM matrix, shows it is very hierarchical, nearly exhibit an identity matrix to leading order. The off-diagonal elements in the CKM matrix is suppressed by one to two orders of magnitude. Additionally, due to the precise and independent measurements of the CKM mixing elements, one can determine the unitarity of the CKM matrix to a high accuracy. An example is $|U_{ud}|^2 + |U_{us}|^2 + |U_{ub}|^2 = 0.99999 \pm 0.0006$, and as a consequence, it leaves very little room for new physics to affect the CKM mixing matrix. This can be compared to our previous discussion about the level of unitarity in the neutrino sector.

Comparing the quark and neutrino sectors, one finds that they behave completely different. In Fig. 3.4, the CKM and PMNS mixing matrices are shown, and while the CKM mixing matrix nearly approximate an identity matrix, then the PMNS mixing matrix has large off-diagonal mixing elements. Additionally, there is a very hierarchical mass spectrum for the charged fermions, whereas the neutrinos shows a mild mass hierarchy. One sees a complete different pattern in the two sectors, and many attempts have been made in order to explain this from first principles. This is studied in the next chapter.

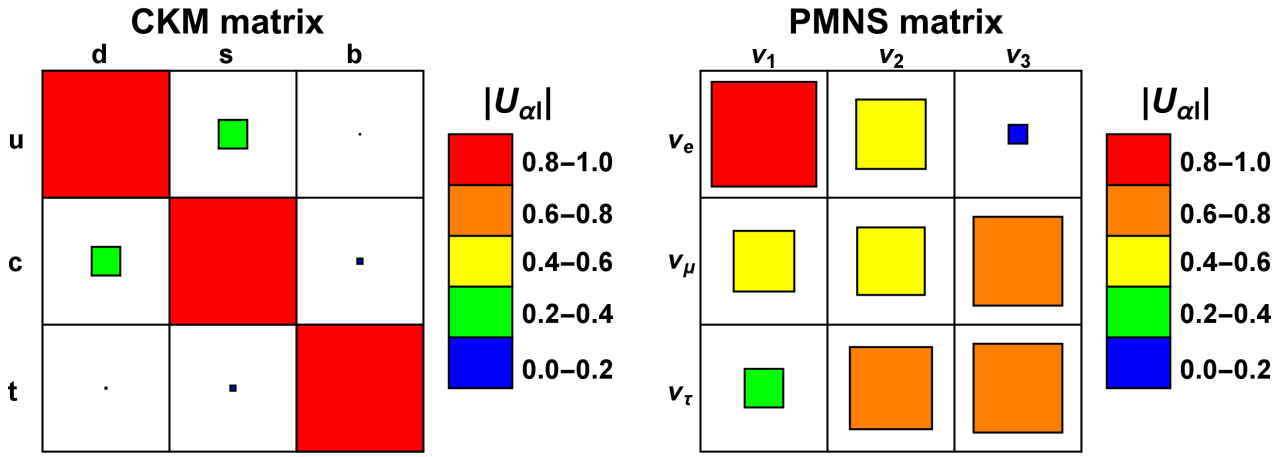

Figure 3.4: Schematic showing the relative magnitudes of mixing elements in the quark (CKM) and neutrino (PMNS) sectors. It is clear that the CKM matrix is largely hierarchical, whereas the PMNS matrix has large off-diagonal elements.

Chapter 4

Modeling of fermion mass and mixing

Considering the measured mixing parameters introduced in the previous chapter, one might wonder whether there is a deeper explanation for the experimental values and their origin. There are many ways to explain the observed mixing parameters, however we are going to discuss the two main proposals here in this chapter. The first possibility relies on symmetries, generating structured mass matrices. Symmetries appear to play an important role in understanding the physics of flavor, and they are described by group theory.

A complete counter example to flavor symmetries is the anarchy hypothesis, which relies on structureless mass matrices. While highly structured mass matrices suggests flavor symmetries as their origin, then the anarchy hypothesis origin might be a very complicated, yet unknown theory or, simply, there is no further explanation. It is a valid option for explaining the measured fermion mixing parameters, and we will explore its application to modeling fermion mass and mixing. Firstly, we introduce the terminology and concepts of finite group theory.

4.1 Group theory terminology

A group $\mathcal{G}$ is a set of elements $\{g_i\}$. They satisfy the following properties [76]:

1. Closure under multiplication: if $g_1, g_2 \in \mathcal{G}$, so $g_1 \cdot g_2 \in \mathcal{G}$.
2. Associativity: for any three elements $g_1, g_2, g_3 \in \mathcal{G}$, then $g_1 \cdot (g_2 \cdot g_3) = (g_1 \cdot g_2) \cdot g_3$.
3. Identity: there exists an element $e \in \mathcal{G}$ such that $e \cdot g = g$ for every $g \in \mathcal{G}$.
4. Inverse: for every $g \in \mathcal{G}$ there exists an inverse, $g^{-1} \in \mathcal{G}$, such that $g \cdot g^{-1} = e$.

Given these axioms, there exists some exponent n for each element g such that $g^n = e$. The smallest exponent is called the order of the element g. This is not to be confused with the order of a group $\mathcal{G}$ which simply means the number of elements in $\mathcal{G}$. The most basic way of defining a group is given in terms of the multiplication table, where the result of each product of two elements is listed. In the case of the smallest ordered non-Abelian finite group, the permutation

group S_3, we have six elements. They are classified into the identity element e, elements b_i whose square is e, and finally the elements a_i whose cube is e. Clearly, the definition of a finite group in terms of its multiplication table becomes cumbersome very quickly with increasing order of $\mathcal{G}$. Therefore, it is necessary to find a more compact way of defining $\mathcal{G}$. Noticing that all six elements of S_3 can be obtained by multiplying only a subset of its elements, we arrive at the notion of generators. Denoting $a_1 = a$ and $b_1 = b$, we obtain $a_2 = a^2$ as well as $b_2 = ab$ and $b_3 = ba$. In other words, a and b generates the group S_3. Being the group of permutations on an equilateral triangle, a corresponds to a 120° rotation and b to a reflection. This observation leads to the definition of S_3 by [76]

$$\langle a, b | a^3 = b^2 = e, ba^{-1}b = a^{-1} \rangle \,, \tag{4.1.1}$$

where the generators have to respect the rules listed on the right. Depending on these rules, a group can be defined uniquely in a compact way. The group $\mathcal{G}$ can have various properties such as being continuous or discrete, Abelian or non-Abelian, etc. with different advantages/difficulties. A discrete flavor symmetry comes with a finite number of generators, and, in addition, no Goldstone bosons or gauge bosons arise contrary to continuous symmetries [76]. However, the origin of the discrete symmetry is assumed to be a continuous gauge symmetry, in order to avoid breaking by gravitational quantum corrections [76]. Non-Abelian symmetries have more freedom for the charge assignment due to containing several two or three dimensional representation of generators, and, consequently, can predict or fit experimental data better. Abelian symmetries have generally the merit that they need only a very simple scalar sector to achieve the necessary flavor symmetry breaking, however it lacks the prediction power of non-Abelian symmetries since the generators commutes (defining property of Abelian symmetries). For further in-depth description about group theory and its consequences, see Ref. [76].

4.2 Paradigm of SM symmetries

The mathematical formulation of the SM is based on the symmetry $\mathcal{G}_{\text{SM}} = SU(3)_C \times SU(2)_L \times U(1)_Y$. This symmetry constrains the possible terms in the SM Lagrangian, which describe interactions among particles and their properties (do they have mass, electric charge, etc.). For example, quarks carry the charge *color*, whereas the other fermions are singlets under this charge, *i.e.* they do not interact via the strong force. Therefore, quarks can only interact with other fermions via the electromagnetic or weak force, whereas they can interact with other quarks/gluons via the strong force since they themself carry the color charge. An other example, the gluons, Z-bosons and W-bosons can self-interact, however this is prohibited for the photon.

This interaction is possible due to the non-commuting generators of the non-Abelian symmetries $SU(3)$ and $SU(2)$, which leads to trilinear couplings for the gluons, Z-bosons and W-bosons. Since $U(1)$ is an Abelian symmetry, it prevents the photon to self-interact. These examples are a direct consequence of the SM symmetry.

However, the SM symmetries are not sufficient to explain the observed fermion mass and mixing values. Therefore, one introduces new flavor symmetries to explain them from first principles. The addition of a parent flavor symmetry, $\mathcal{G}_\mathcal{F}$, extends the SM symmetries to

$$\mathcal{G} = SU(3)_C \times SU(2)_L \times U(1)_Y \times \mathcal{G}_\mathcal{F}\,, \tag{4.2.1}$$

requiring that the Lagrangian remains invariant under the transformations of this symmetry. It is usually assumed that the parent symmetry is broken at high energies to subgroups in the quark $\mathcal{G}_\mathcal{Q}$ and lepton $\mathcal{G}_\mathcal{L}$ sectors. Thereafter, they are subsequently broken to subgroups in the charged lepton $\mathcal{G}_\mathrm{e}$, neutrino $\mathcal{G}_\nu$, up quark $\mathcal{G}_\mathrm{u}$ and down quark $\mathcal{G}_\mathrm{d}$ sectors

$$\mathcal{G}_\mathcal{F} \to \begin{cases} \mathcal{G}_\mathcal{L} \to \begin{cases} \mathcal{G}_\nu \\ \mathcal{G}_\mathrm{e} \end{cases} \\ \mathcal{G}_\mathcal{Q} \to \begin{cases} \mathcal{G}_\mathrm{u} \\ \mathcal{G}_\mathrm{d} \end{cases} \end{cases} . \tag{4.2.2}$$

The particle fields can transform either differently under $\mathcal{G}_\mathcal{F}$ or in the same way. The parent symmetry $\mathcal{G}_\mathcal{F}$ can be Abelian or non-Abelian (we consider both cases in the following chapters), and the residual symmetries ($\mathcal{G}_\nu, \mathcal{G}_e, \mathcal{G}_u$ and $\mathcal{G}_d$) present in the SM Lagrangian must be Abelian and of order $N \geq$ number of mass generations (requirement of family generations having distinct masses and non-trivial mixing). Considering an example in the lepton sector, the transformation rules acts on the left-handed lepton doublets ℓ_L, right-handed charged lepton singlets e_R and neutrinos ν according to

$$\ell_L \to X_L \ell_L\,, \quad e_R \to X_R e_R\,, \quad \nu \to X_\nu \nu. \tag{4.2.3}$$

The unitary matrices X_L, X_R and X_ν belong to a representation of the symmetry group $\mathcal{G}_\mathcal{F}$, thus constraining the form of the charged lepton and neutrino mass matrices by

$$M_\ell = X_L^\dagger M_\ell X_R\,, \quad M_\nu = X_\nu^\dagger M_\nu X_\nu\,, \tag{4.2.4}$$

respectively. This can occur solely for the quarks/leptons or jointly if they are all charged under the same symmetry group. Model builders look for an underlying symmetry that can explain

the pattern of fermion masses and mixings. Hereafter, we investigate some examples to illustrate the power of using flavor symmetries to predict the observed fermion masses and mixings.

4.3 Examples of predicting fermion masses and mixings using flavor symmetries

These examples show the logic behind using flavor symmetries to explain the observed fermion masses and mixings. We start with a simple example in the neutrino sector which uses a symmetry between the muon and tau flavor. Thereafter, we investigate a general method to generate a hierarchical mass spectrum which can be applied to both the quark and lepton sectors.

4.3.1 A $\mu - \tau$ symmetric mass model

A well-studied example of explaining neutrino masses and mixings is the $\mu - \tau$ symmetry [77]. The neutrino mass matrix has to be invariant under this symmetry. In the basis where the charged lepton mass matrix is diagonal, the neutrino mass matrix becomes [77]

$$M_\nu^{\mu-\tau} \equiv \begin{pmatrix} x & y & y \\ y & z & w \\ y & w & z \end{pmatrix} . \tag{4.3.1}$$

This symmetry can be represented by the generator

$$T = \begin{pmatrix} 1 & 0 & 0 \\ 0 & 0 & 1 \\ 0 & 1 & 0 \end{pmatrix} , \tag{4.3.2}$$

so that $T^\dagger M_\nu T = M_\nu$. This generator satisfy the four properties described in numeration 1-4. Diagonalizing the mass matrix gives the mixing matrix

$$U = \begin{pmatrix} \cos\theta_{12} & \sin\theta_{12} & 0 \\ -\frac{\sin\theta_{12}}{\sqrt{2}} & \frac{\cos\theta_{12}}{\sqrt{2}} & \frac{1}{\sqrt{2}} \\ -\frac{\sin\theta_{12}}{\sqrt{2}} & \frac{\cos\theta_{12}}{\sqrt{2}} & -\frac{1}{\sqrt{2}} \end{pmatrix} , \tag{4.3.3}$$

which predicts maximal atmospheric mixing, *i.e.* $\theta_{23} = 45°$, and vanishing reactor angle, *i.e.* $\theta_{13} = 0$. Considering real entries in the neutrino mass matrix, there are four degrees of freedom present in Eq. (4.3.1) corresponding to three mass eigenvalues and the solar mixing angle θ_{12}.

These parameters are predicted in terms of the matrix elements by

$$\begin{aligned}
\sin^2 2\theta_{12} &= \frac{8y^2}{(x-w-z)^2+8y^2}\,, \\
m_1 &= \frac{1}{2}\left[x+z+w-\sqrt{(x-z-w)^2+8y^2}\right]\,, \\
m_2 &= \frac{1}{2}\left[x+z+w+\sqrt{(x-z-w)^2+8y^2}\right]\,, \\
m_3 &= z-w\,.
\end{aligned}$$

If the solar mixing angle is $\sin^2\theta_{12}=\frac{1}{3}$, the mixing matrix becomes the tribimaximal (TBM) mixing matrix [77]

$$U_{\text{TBM}} = \begin{pmatrix} \frac{2}{\sqrt{6}} & \frac{1}{\sqrt{3}} & 0 \\ -\frac{1}{\sqrt{6}} & \frac{1}{\sqrt{3}} & \frac{1}{\sqrt{2}} \\ -\frac{1}{\sqrt{6}} & \frac{1}{\sqrt{3}} & -\frac{1}{\sqrt{2}} \end{pmatrix}. \tag{4.3.4}$$

This is a very simple and predictive mixing matrix, and the framework of flavor symmetry tries to give a simple parameterization of the mixing matrix. Considering complex matrix entries, one has more degrees of freedom than observables, meaning one cannot fix all of the theory parameters. However, complex entries lead to CP violation compared real matrix entries (CP conservation). To recap, we promote the $\mu-\tau$ symmetry to a physical symmetry, thereby deriving the most generic mixing matrix Eq. (4.3.3), as well as the most generic $\mu-\tau$ invariant mass matrix Eq. (4.3.1). It is the first hint that understanding flavor mixing in the neutrino sector may be related to the imposition to a global discrete symmetry, as T is the generator of a cyclic symmetry Z_2. The $\mu-\tau$ permutation symmetry is not experimental viable due to the observation of non-zero θ_{13}, however a small breaking of this symmetry means the mass matrix can be written as [77]

$$M_\nu^{\cancel{\mu-\tau}} = M_\nu^{\mu-\tau} + M_\nu^{\text{breaking}} = \begin{pmatrix} x & y(1+\epsilon_1) & y(1-\epsilon_1) \\ y(1+\epsilon_1) & z(1+\epsilon_2) & w \\ y(1-\epsilon_1) & w & z(1-\epsilon_2) \end{pmatrix}, \tag{4.3.5}$$

where ϵ_1, ϵ_2 are small parameters. Using this mass matrix, one may argue that the neutrino mass matrix possesses an *approximate* $\mu-\tau$ permutation symmetry. By scanning over different theory parameters, experimental viable mixing parameters can be obtained. Therefore, this symmetry can still be used to leading order for model builders. This example shows the generation of the neutrino mixing parameters only since the approximate $\mu-\tau$ permutation symmetry is only viable in the neutrino sector. However, the next example can explain the observed mass

hierarchies in the fermion sector.

4.3.2 The Froggatt-Nielsen framework

A hierarchical mass spectrum can be explained by the Froggatt-Nielsen (FN) mechanism [78], which relies on continuous $U(1)$ flavor symmetries. However, in common practice, one introduces discrete cyclic groups Z_n to keep a finite number of generators. This is valid since $Z_n \in U(1)$, and one assumes the Z_n symmetry originates from a continuous $U(1)$ symmetry. In turn, this introduces a scalar flavon field f_k for each symmetry (defining property of introducing Abelian symmetries). They are only charged under its associated symmetry, but a singlet under all other symmetries. They acquire a non-zero universal vacuum expectation value (VEV) $\langle f_{n_k} \rangle \simeq v_f$ that spontaneously breaks the symmetry to generate the Yukawa/mass terms. At the same time, one introduces superheavy fermions with universal mass M_F, meaning the SM fermions can couple to them. Integrating out the superheavy fermions and the flavon fields, leads to an effective Yukawa term of the form [78]

$$\left(\frac{v_f}{M_F}\right)^n H\psi_L\psi_R \tag{4.3.6}$$

between the left-handed fermion ψ_L, the right-handed fermion ψ_R, and the Higgs H. Here, the exponent n depends on the charge assignments of the particle field. It is usually assumed that $v_f/M_F \leq 1$, such that the requirement of a perturbative field theory is satisfied. The factor $(v_f/M_F)^n$ acts as the Yukawa coupling of the mass term, and it explains the observed hierarchical mass spectrum. Thereafter, the Higgs boson obtains a VEV v, meaning the fermion ψ acquires a mass $m_\psi = v \cdot (v_f/M_F)^n$. Originally, the FN mechanism was inspired by the seesaw mechanism [79], where, as explained previously, one introduces heavy degrees of freedom. Integrating them out, leads to an effective neutrino mass matrix, and it is capable of explaining the observed mass spectrum. A pictorial example of the FN mechanism is shown in Fig. 4.1, where the intermediate steps with the flavons f_k and heavy fermions F leads to the suppression of the Yukawa coupling. Contracting the intermediate steps leads to the effective mass term in Eq. (4.3.6).

The mass ratios of the charged fermions can be described to leading order by [80]

$$m_u : m_c : m_t \sim \epsilon^6 : \epsilon^4 : 1, \quad m_d : m_s : m_b \sim \epsilon^4 : \epsilon^2 : 1\,, \quad m_e : m_\mu : m_\tau \sim \epsilon^4 : \epsilon^2 : 1\,, \tag{4.3.7}$$

where $\epsilon \simeq 0.2$ may be a remnant of a Grand Unified Theory (GUT) model. Additionally, one

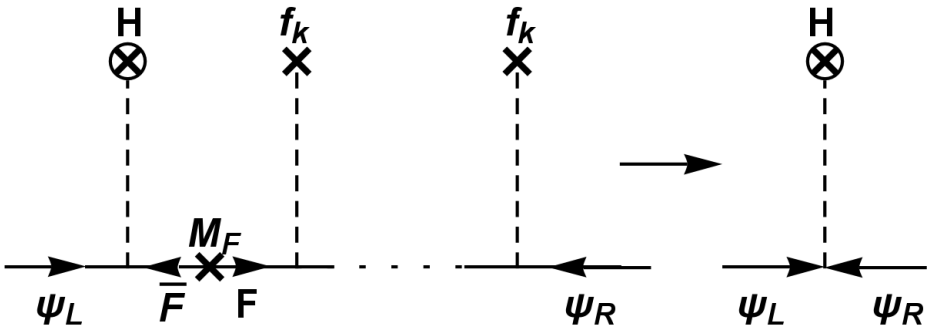

Figure 4.1: Generation of fermion mass term via the Froggatt-Nielsen mechanism, where the Yukawa coupling originates from integrating out the superheavy fermions with mass M_F (represented by the internal solid lines) and the flavons f_k, which are responsible for breaking the flavor symmetry with their universal VEV v_f. This leads to an effective mass term among the Higgs boson H and the SM fermion ψ, similar to Eq. (4.3.6), as displayed on the right side of the arrow.

can also describe the neutrino mass ratio by this approximation [80] via

$$m_1 : m_2 : m_3 \sim \epsilon^2 : \epsilon : 1, \quad m_1 : m_2 : m_3 \sim 1 : 1 : \epsilon\,, \quad m_1 : m_2 : m_3 \sim 1 : 1 : 1\,, \tag{4.3.8}$$

for normal, inverted and degenerate mass ordering, respectively. Using the FN mechanism, one can derived these mass ratios by assuming $v_f/M_F \simeq \epsilon \simeq 0.2$, and it is one of its strengths. In the FN mechanism, an order one complex number is allowed in each matrix element, leading to arbitrary mixings. Therefore, the FN mechanism is usually accompanied by a non-Abelian flavor symmetry, which fixes the mixing parameters. Rather than relying on flavor symmetries, a different approach uses structureless mass matrices to explain the fermion masses and mixing parameters.

4.4 The anarchy hypothesis

A perfect counter example to flavor symmetries is the *anarchy hypothesis* [6, 7], which relies on structureless mass matrices, and it gives an alternative explanation for the fermion mixing observables. The anarchy hypothesis generates the mass matrices in a basis-independent manner (ensuring structureless mass matrices in any basis), and this is done via the Haar measure [7]

$$dU_{\text{PMNS}} \propto ds_{12}^2 dc_{13}^4 ds_{23}^2 d\delta d\alpha_1 d\alpha_2\,, \tag{4.4.1}$$

where $s_{ij} = \sin\theta_{ij}$ and $c_{ij} = \cos\theta_{ij}$. This ensures the mixing parameters have a flat distribution, meaning θ_{12} has a flat distribution in $\sin^2\theta_{12}$, θ_{13} has a flat distribution in $\cos^4\theta_{13}$, etc.. However, the Haar measure does not dictate the choice of mass eigenvalues (it involves the mixing parameters only), meaning an arbitrary mass eigenvalue distribution is possible. If the matrix elements have to be distributed independently from each other, there is only one choice: the Gaussian measure [81]. This means, in practice, one chooses the entries of the fermion mass matrix from a Gaussian distribution, and, as a consequence, the mixing parameters will have a flat distribution according to Eq. (4.4.1). Therefore, a particular random set of matrix entries will explain the observed mixing parameters by chance.

The above mention example of the anarchy hypothesis uses a simple linear method of picking the matrix entries from a Gaussian distribution X, *i.e.* $M \sim X$. However, a different method is possible, where the fermion mass matrix is given by random matrix squared, *i.e.* $M \sim X^\dagger X$. This is the Wishart method [82], and using this method, the Dirac and Majorana mass matrices are given by

$$M_D = \frac{m_D}{N}(F^\dagger F)\,, \qquad M_R = \frac{M_0}{2N}(G^\dagger G + G^T G^*)\,, \tag{4.4.2}$$

respectively. Here, F and G are $N \times 3$ complex random matrices of order unity, and m_D and M_0 represents the typical mass scales. The Majorana mass matrix has two terms since it has to obey $M_R = M_R^T$. In general, N can be arbitrary and does not have to be equal to 3. However in the neutrino sector, one can place an upper bound on $N \leq 35$ [82] in order to explain the observed neutrino mass square differences. Using the Wishart method, the mixing matrix is still distributed according to the Haar measure Eq. (4.4.1), and the advantage of this method, it leads to degenerate mass spectrum for high N.

Given the different examples mention above, we consider a short, but descriptive resume of the scientific content concerning the origin of fermion masses and mixing parameters next.

4.5 Previous work in quark and lepton sectors

There is a bulk of theoretical studies explaining the mixing parameters and masses in the lepton and/or quark sectors using different flavor symmetries. Recently, a lot of effort was focused on the lepton sector due to a non-zero reactor angle θ_{13}, meaning simple models based on, e.g., the flavor symmetry A_4 [83–88] must be abandoned or substantially modified [89–102]. Pursuing new territories, it was anticipated that new models would easily explain the observation of a non-zero θ_{13}. However, all model-independent scans of the lepton sector indicates that only groups with order $\mathcal{O}(100)$ or larger can quantize the full PMNS matrix within 3σ [1, 103–109]. This applies for both Majorana and Dirac-type neutrinos, and independently of whether the parent

symmetry $\mathcal{G}_\mathcal{F}$ is a subgroup of $SU(3)$ or $U(3)$. However, it only applies to direct models which predicts all mixing angles. Similar studies confirmed this, whether it came from general group theoretical arguments [110] or from a bottom-up approach [111]. The need for a high ordered symmetry to quantize the full PMNS mixing matrix within 3σ, means more and more theory parameters (elements of the symmetry group) are introduced. Therefore, it is more interesting to turn towards the anarchy hypothesis since it can explain the observed mixing parameters in the neutrino sector quite well. The probability of a more unusual neutrino mixing parameter choice is 42% [112], with a lower (upper) bound of 40% (44%) for the 3σ range. This means the anarchy hypothesis is consistent with explaining the origin of the neutrino oscillation parameters.

In the quark sector, studies are performed in light of the leptons, *i.e.* searching for flavor symmetries which have the same origin (e.g. subgroups of $\Delta(6N^2)$) [113–116], but given the hierarchical structure of the CKM matrix, no finite group can predict all mixing parameters of the CKM to any accuracy. Small ordered Dihedral groups such as D_{14} and other variants can predict the Cabibbo angle to leading order [117, 118], however a larger order is needed if the Cabibbo angle has to be within 3σ. Therefore, considering small ordered groups to explain the observed fermion mixings, their predictions have to be modified, perhaps via Renormalization Group running [119–121] or additional symmetry breaking effects as have been studied in the lepton sector [122–124]. We will adopt this philosophy in Chapter 6. As a sidenote, the anarchy hypothesis has also been applied to the quark sector, however the compatibility probability is smaller than 6×10^{-6} [125]. This implies that the CKM matrix is safely discarded as a random unitary matrix, and a deeper explanation is needed to describe the entries in the CKM matrix.

Lastly, we consider a specific model for neutrino mass generation. This model does not give a deeper explanation for the mixing parameters, but it incorporates additional observed phenomena seen in Nature. Neutrino masses and mixings, dark matter and the baryon asymmetry is described in an unified framework by introducing three sterile neutrinos to the SM, and this model is dubbed the Neutrino Minimal SM (νMSM) [127, 128]. Since the sterile neutrinos are singlets under the SM symmetries, one can add an arbitrary number and at any mass scale; the specific details of the νMSM are described further down in the text. With only minimal modifications, it tries to explain all experimental data, and this is without changing the gauge group, the number of fermions remains the same (disregarding the introduction of the sterile neutrinos here), and no new energy scale above the Fermi scale is introduced. The dark matter candidate is a keV sterile neutrino, and as a fermionic DM candidate, the mass is constrained by the Tremaine-Gunn bound [129] on the phase space density in the Milky way's dwarf spheroidal galaxies, yielding a lower bound of 1 keV $< M_1$. Its active-sterile mixing is quite small due to the stringent X-ray limits, and as a consequence, the lightest of the active neutrinos is massless ($m_{\text{min}} < 10^{-5}$ eV). The generation of neutrino mass occurs due to two degenerate GeV sterile

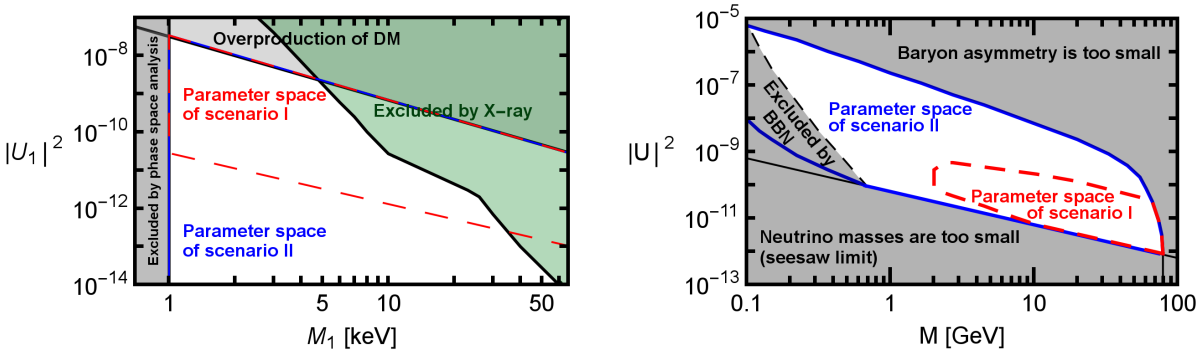

Figure 4.2: Allowed parameter space in the νMSM for the different scenarios (I and II), while the dark shaded regions (grey or green) are excluded by experimental limits. (Left) Active-sterile mixing of the DM sterile neutrino as a function of its mass. (Right) Active-sterile mixing of the GeV sterile neutrinos as a function of its mass. Figure taken from Ref. [126].

neutrinos via the seesaw mechanism Eq. (2.3.2), thereby explaining the small neutrino masses. The active-sterile mixing is a possible observable in future experiments, and it is given by [64]

$$|U_{\alpha I}|^2 = |(U_\ell^\dagger \theta U_N)_{\alpha I}|^2 \,, \qquad |U_I|^2 = \sum_\alpha |U_{\alpha I}|^2 \,, \tag{4.5.1}$$

where $|U_{\alpha I}|^2$ is the flavored active-sterile mixing, whereas $|U_I|^2$ represents the total mixing. These mixings enters decay rates [126, 130]

$$\begin{aligned}\Gamma(N_I \to X\ell_\alpha) = &\frac{|U_{\alpha I}|^2}{16\pi} G_F^2 |V_X|^2 f_X^2 M_I^3 \left(\left(1 - \frac{M_\ell^2}{M_I^2}\right)^2 - \frac{M_X^2}{M_I^2}\left(1 + \frac{M_\ell^2}{M_I^2}\right)\right) \\ &\times \sqrt{\left(1 - \frac{(M_X - M_\ell)^2}{M_I^2}\right)\left(1 - \frac{(M_X + M_\ell)^2}{M_I^2}\right)} \,,\end{aligned} \tag{4.5.2}$$

where the Fermi constant is G_F, the sterile neutrino (charged lepton) mass is M_I (M_ℓ), and the charged hadron X has a mass M_X. As a sidenote, the CKM matrix element $|V_X|$ enters, and to mention some examples, the CKM mixing element is $|V_X|^2 = |V_{ud}|^2 \equiv 0.949$ ($|V_X|^2 = |V_{us}|^2 \equiv 0.051$) for a pion (kaon) in the final state [20]. Additionally, the two GeV sterile neutrinos generate the baryon asymmetry [131–133], *i.e.* $\eta_B = (6.10 \pm 0.04) \cdot 10^{-10}$, through CP-violating oscillations. They generate a lepton asymmetry, which gets converted to a baryon asymmetry by the SM sphaleron processes. As a consequence, they have to be very degenerate

in mass, roughly $\delta M/M < 10^{-3}$ or smaller [126]. Due to the various constraints for realizing the νMSM, the parameter space for two benchmark scenarios are obtained. The total active-sterile mixing parameter space of the dark matter sterile neutrino (two GeV sterile neutrino) is shown on the left (right) side of Fig. 4.2 as a function of mass. The main difference between the two benchmark scenarios lies in the dark matter production. In scenario I, one assumes the dark matter is produced via active-sterile mixing only. The effective active-sterile mixing in the primordial plasma is given by [134]

$$\sin^2 2\theta_{\text{plasma}} \simeq \frac{\sin^2 2\theta_{\text{vac}}}{\sin^2 2\theta_{\text{vac}} + \left(\cos 2\theta_{\text{vac}} + (T^4 - \mu(T))/M^2\right)^2}\,, \tag{4.5.3}$$

where T is the temperature, M is the dark matter mass, θ_{vac} is the active-sterile mixing angle in vacuum, and μ is the lepton asymmetry. Introducing a lepton asymmetry in the primordial plasma, means a resonant MSW-like production mechanism is possible. As the temperature decreases in the expanding Universe, one obtains a resonant production due to cancellations between the terms in the effective active-sterile mixing angle. The largest lepton asymmetry found in the literature is $1.24 \cdot 10^{-4}$ [126], giving the lower bound for scenario I in the dark matter parameter space. However, as a consequence of the resonant dark matter production, one reduces the parameter space of the two GeV sterile neutrinos. Scenario II has the same particle content as scenario I, but the dark matter production mechanism remains unknown, meaning one cannot ensure the correct dark matter abundance in this scenario. As a result, the allowed parameter space of the two GeV sterile neutrinos enlarges since there is more freedom. Therefore, scenario II is an interesting benchmark scenario since it shows the complete allowed parameter space of the two GeV sterile neutrinos in general, whereas in scenario I, the parameter space is limited due to producing the correct abundance of dark matter. The actual dark matter production mechanism is secondary in this case.

Chapter 5

Abelian symmetric GeV neutrino mass generation

In the previous chapter, we discussed the νMSM, which is capable of explaining neutrino mass, dark matter, and the baryon asymmetry in an unified framework. This is done by introducing three sterile neutrinos, one keV dark matter candidate together with two degenerate GeV sterile neutrinos. Under certain conditions, it is possible to fully constrain the model parameter space. Therefore, this model has gotten a lot of interest, both theoretically and experimentally, and we will use this model as a basis when investigating flavor symmetry's impact on the active-sterile mixings. We will use a νMSM-like logic to explain the origin of the physical observables by introducing three GeV sterile neutrinos in our method, thereby relaxing the mass degeneracy needed to produce successful leptogenesis [135].

5.1 Experimental observables and future experiments

By introducing three GeV sterile neutrinos, there are many ways to experimentally constrain or exclude their parameter space. We focus on the active-sterile mixings Eq. (4.5.1). In general, due to their unknown masses, the sterile neutrinos can decay into heavier particles such as charmed mesons, B-mesons, gauge bosons, and Higgs bosons [136]. Peak searches are an effective method to study lighter sterile neutrinos, and it is usually done by beam-dump experiments, probing the mass range $0.1 - 2$ GeV [137]. B-factories can probe slightly heavier masses of $2 - 5$ GeV, whereas hadron or lepton colliders are sensitive to the mass range of 5 GeV$-$3 TeV. There are various methods to probe sterile neutrinos, either relying on displaced vertices or studying lepton flavor-violating (LFV) processes such as $pp \to W^* \to N(\to \ell^\pm jj)\ell^\pm$ with $\ell = \{e, \mu\}$ [136–138]. A variety of current experiments are searching for sterile neutrinos in the MeV-TeV energy range, *e.g.* BABAR[139], Belle[139], LHCb[140], ATLAS[141], and CMS[142]. Additionally, future experiments are proposed such as SHiP[143, 144], DUNE[145, 146], ILC[147], and FCC[148], which can also search for sterile neutrinos. We consider Search for Hidden Particles (SHiP), Future Circular Collider (FCC), and Deep Underground Neutrino Experiment (DUNE, formerly LBNE) experiments in our study, which are sensitive to the active-sterile mixing in the GeV

range. These are representative cases for the different proposed experiments which might be built in the future, and we introduce them one by one, discussing their experimental observables.

A proposed beam-dump experiment is SHiP, and it will be built at CERN if the experiment is approved for funding. It searches for hidden particles such as supersymmetric particles, dark photons, and sterile neutrinos. The SHiP Collaboration has published the processes they will investigate in Table 5.3 in Ref. [143], and we can deduce their observables from these final state decays: one measure the flavored active-sterile mixings by tagging the associated charged lepton in the processes. Take the process $N_I \to \mu\pi$ as an example. It is sensitive to $|U_{\mu I}|^2$ due to the flavor of the final state charged lepton. It implies that the sterile neutrino must have mixed with a muon neutrino, which subsequently lead to the considered decay. Using a similar argumentation, the process $N_I \to e\pi$ is sensitive to $|U_{eI}|^2$. Additionally, they are also sensitive to the total mixing $|U_I|^2$ by investigating decays such as $N_I \to \eta\nu \to \pi^+\pi^-\pi^0 + p^{\text{miss}}$. Here, the light neutrino appears as missing energy, meaning one has to sum over all possible flavors. Therefore, the SHiP experiment measures, in principle, the flavored mixings $|U_{eI}|^2$ and $|U_{\mu I}|^2$, and the total mixing $|U_I|^2$. The sensitivity bounds of the SHiP experiment are given in Refs. [143, 144], however we are not aware of any sensitivity study for the total mixing without assuming a ratio among the individual mixing elements. Therefore, no direct bounds for the total mixing are displayed. As a sidenote, one could obtain a bound for the total mixing from the bounds of the flavored mixings if $|U_{\tau I}|^2$ was measured.

Next generation of long-baseline neutrino experiments are under consideration for funding/constructing at this time, and DUNE is a possible candidate. With a baseline of 1300 km, it is ideal to measure the neutrino mass ordering and the lepton CP-violating phase δ due to matter effects. Additionally, it is also sensitive to the active-sterile mixings of GeV sterile neutrinos. No channel modes are reported by the DUNE Collaboration yet, however they are sensitive to a similar mass range as the SHiP experiment. This experiment has a lower initial proton energy compared to SHiP[1], meaning no significant mixing with the tau flavor is expected. Therefore, we expect similar final states as studied by SHiP, meaning we assume DUNE is sensitive to $|U_{eI}|^2$, $|U_{\mu I}|^2$, and $|U_I|^2$ for which we do not show any direct sensitivity curve.

A possible successor of the LHC experiments is the FCC experiment, which will have an accelerator circumference of 80–100 km. In the initial physics program, they consider colliding leptons with a center-of-mass (CM) energy of 90–350 GeV [148]. Thereafter, colliding hadrons with CM energies up to 100 TeV is considered. The main goal of this experiment is to measure the Higgs boson's couplings at the percent level, but it is also sensitive to GeV sterile neutrinos.

[1]The initial proton beam energy of the DUNE experiment is expected to be 80-120 GeV. This can be compared to 400 GeV at the SHiP experiment [145, 146].

Specifically, one can measure the Z-boson partial decay width

$$\Gamma_{Z\to\nu N_I} = 3\Gamma^{\rm SM}_{Z\to\nu\nu}|U_I|^2(1-(M_I/M_Z)^2)^2(1+(M_I/M_Z)^2)\,, \tag{5.1.1}$$

where $\Gamma^{\rm SM}_{Z\to\nu\nu}$ is the Z-boson decay rate into two light neutrinos, and M_I is the mass of the sterile neutrino. They use a displaced vertex method to tag possible interesting events. Evidently from Eq. (5.1.1), FCC is only sensitive to the total mixing $|U_I|^2$ at the Z-pole[2]. Two other interesting processes are $e^-e^+ \to N(\to \ell^\mp W^\pm)\nu_\ell \to \ell + 2j + \not{E}_{\rm missing}$ and $e^-e^+ \to N(\to \ell'^\mp W^\pm)\ell^\mp W^\pm \to 2\ell + 4j$, which leads to different final states, meaning one can distinguish between them. The first has one lepton, two jets, and missing energy as final states, and the other process leads to two leptons and four jets. One reduces the background by applying kinematical cuts, and, for the latter process, selecting two outgoing leptons with same electric charge [136].

The sensitivity bounds are studied under different assumptions, meaning it is difficult to make a direct comparison. SHiP and DUNE assume a specific ratio among the flavor-dependent mixings, meaning they are capable of translating a bound on the flavored mixing element into a bound on the total mixing. No such assumption is used by the FCC Collaboration since they can directly measure the total mixing.

The SHiP Collaboration consider five different scenarios, where they assume a specific ratio among the flavored active-sterile mixings [143]:

$$\begin{aligned}
&\textbf{Case 1:} && |U_{eI}|^2 : |U_{\mu I}|^2 : |U_{\tau I}|^2 \sim 52:1:1 \text{ for IO},\\
&\textbf{Case 2:} && |U_{eI}|^2 : |U_{\mu I}|^2 : |U_{\tau I}|^2 \sim 1:16:3.8 \text{ for NO},\\
&\textbf{Case 3:} && |U_{eI}|^2 : |U_{\mu I}|^2 : |U_{\tau I}|^2 \sim 0.061:1:4.3 \text{ for NO},\\
&\textbf{Case 4:} && |U_{eI}|^2 : |U_{\mu I}|^2 : |U_{\tau I}|^2 \sim 48:1:1 \text{ for IO},\\
&\textbf{Case 5:} && |U_{eI}|^2 : |U_{\mu I}|^2 : |U_{\tau I}|^2 \sim 1:11:11 \text{ for NO},
\end{aligned} \tag{5.1.2}$$

where NO (IO) means normal (inverted) ordering of the light neutrinos. Using the ratios, they can obtain their sensitivity to the *total* active-sterile mixing for the different scenarios. The sterile neutrino mixes predominantly with one flavor for the first three cases (electron, muon or tau flavor) [130], whereas the latter two cases are interesting in the context of the baryon asymmetry [150]. The SHiP Collaboration consider case 2 as their benchmark scenario, and they calculate the total active-sterile mixing sensitivity for case 2 only. Using the ratios given above, one obtains the sensitivities for the other cases by extrapolating the sensitivity from

[2]FCC and other proposed lepton colliders (ILC and CepC) can also measure the mixing element $|U_{eI}|^2$ if the CM energy is increased to $200-500$ GeV since the W-exchange of the process $ee \to e\nu_e$ (t-channel) dominates over the Z-exchange $ee \to \ell\nu_\ell$ (s-channel) with $\ell = \{e,\mu,\tau\}$ [136, 149]. However, these measurements are less sensitive than FCC's measurement of the total mixing, meaning we disregard them due to $|U_{eI}|^2 \leq |U_I|^2$.

case 2. Therefore, we use the sensitivity bound of case 2 when appropriate [130], otherwise we explicitly state the bound used.

The sensitivity curve from the DUNE Collaboration [145] is estimated by a simple scaling by comparing experimental parameters, such as protons on target, number of produced charm mesons, detector length, and detector area with the CHARM [151] and PS191 experiments [152]. This means that the limit of CHARM/PS191 is extrapolated to the expected sensitivity of DUNE. However, CHARM and PS191 have only reported limits of the individual mixing elements $|U_{eI}|^2$ and $|U_{\mu I}|^2$, meaning DUNE's sensitivity curve is only valid when these flavored mixing elements dominate the total mixing. Therefore, the DUNE and SHiP sensitivities are derived under similar assumptions. We choose the optimistic curve for the DUNE experiment [145].

The FCC experiment have reported various sensitivity curves for different experimental setups, such as detector length, running time, and decay length of the sterile neutrino. We use the more optimistic sensitivity curve, *i.e.* the one for a detector length of 30 m, 10^{13} Z-bosons produced, and decay length of 0.01-500 mm [148].

5.2 Model-independent view of total mixings

In this section, we investigate the total mixing of the lightest and heaviest sterile neutrino, and we use two model-independent methods which produce viable candidates for the charged lepton Yukawa matrix Y_ℓ, the Dirac mass matrix M_D, and the Majorana mass matrix M_R. The first method is the Casas-Ibarra parameterization, which uses the neutrino mixing parameters as input and parameterizes the different degrees of freedom. The second approach uses a "generate-and-tune" method to obtain neutrino oscillation parameters from random mass matrices. Thereafter, we discuss the results, and compare them to the expected sensitivity bounds of future experiments.

5.2.1 Casas-Ibarra parameterization and random mass matrices

The first method uses the Casas-Ibarra parameterization of the Dirac mass matrix [153]

$$M_D = U_{\text{PMNS}} \sqrt{m_\nu^{\text{diag}}} \mathcal{R}^T \sqrt{M_R}\,, \tag{5.2.1}$$

and it is a self-consistent parameterization in the seesaw framework. It uses the physical observables, such as neutrino mixing parameters $U_{\text{PMNS}}(\theta_{12}, \theta_{23}, \theta_{13}, \delta, \alpha, \beta)$, and neutrino masses $m_\nu^{\text{diag}} = \text{diag}(m_1, m_2, m_3)$, as input. The other matrices $M_R = \text{diag}(M_1, M_2, M_3)$ and $\mathcal{R}$ parameterizes the degrees of freedom, and are not directly accessible to experiments. A diagonal M_R is generally allowed due to freedom of redefining the particle fields in the SM Lagrangian,

but this choice of basis means an underlying flavor symmetry for generating the mass matrices is not visible anymore. The matrix $\mathcal{R}$ satisfies the constraint $R^T R = 1$, meaning it can be parameterized as [153]

$$\mathcal{R} = \begin{pmatrix} c_{12}c_{13} & s_{12}c_{13} & s_{13} \\ -s_{12}c_{23} - c_{12}s_{23}s_{13} & c_{12}c_{23} - s_{12}s_{23}s_{13} & s_{23}c_{13} \\ s_{12}s_{23} - c_{12}c_{23}s_{13} & -c_{12}s_{23} - s_{12}c_{23}s_{13} & c_{23}c_{13} \end{pmatrix}, \tag{5.2.2}$$

where $c_{ij} = \cos\omega_{ij}$ and $s_{ij} = \sin\omega_{ij}$ with ω_{ij} being a complex angle. The dependence of the parameter $\mathrm{Re}(\omega_{ij})$ is periodic [154], whereas $\mathrm{Im}(\omega_{ij})$ has no limit in general. Therefore, we choose $\mathrm{Re}(\omega_{ij}) \in [0, 2\pi]$ and $\mathrm{Im}(\omega_{ij}) \in [-8, 8]$ since a broader range is without consequence.

Model predictions with GeV heavy neutral lepton (HNL) masses are generated by choosing neutrino oscillation parameters from their 3σ ranges[3] [68], whereas the three CP-violating phases (one Dirac-type and two Majorana-type) are free to vary in the interval $\delta, \alpha, \beta \in [0, 2\pi]$. We rewrite the neutrino masses, so they depend on the mass square differences and the lightest neutrino mass, however we do not known the absolute mass scale. We have an upper limit on the sum of the neutrino masses from cosmology $\sum m_\nu < 0.72$ eV [29], leading to the interval for the lightest neutrino mass $m_{\mathrm{min}} \in [0, 0.23]$ eV. We consider the normal ordering of the neutrino mass hierarchy only, since we expect a similar result for inverted ordering. Since we are interested in GeV sterile neutrinos, we choose the interval $M_I \in [0.1, 80]$ GeV with the requirement $M_1 < M_2 < M_3$. Due to this requirement, we show the parameter space for the lightest and heaviest sterile neutrino only, thereby omitting the parameter space of the intermediate sterile neutrino. It is redundant since its parameter space lies between the parameter space of the two other sterile neutrinos. Additionally, each figure will satisfy the paradigm "one model, one dot", meaning all realizations of a specific scenario fulfilling every experimental constraint are shown.

In the second method, we generate random mass matrices

$$Y_\ell = \mathrm{diag}(y_e, y_\mu, y_\tau)\,, \quad M_D = m_D \begin{pmatrix} c_1 & c_2 & c_3 \\ c_4 & c_5 & c_6 \\ c_7 & c_8 & c_9 \end{pmatrix}, \quad M_R = \mathrm{diag}(M_1, M_2, M_3)\,, \tag{5.2.3}$$

where m_D controls the overall mass scale of the Dirac mass matrix, and c_i are independent order one complex numbers with $|c_i| = k_i$ and $\arg(c_i) = \phi_i$ for $i = [1, ..., 9]$. One obtain these matrices since one has the freedom to redefine the particle fields, meaning the mass matrices have a structure similar to the Casas-Ibarra parameterization. One might choose non-diagonal

[3] We use the standard parameterization of U_{PMNS} for Majorana neutrinos Eq. (3.1.5).

M_R and Y_ℓ, however it yields similar results due to basis-independence of physical observables. Using Eq. (5.2.3), leaves less free theory parameters compared to non-diagonal Y_ℓ and M_R. We dub this method the "random case" since the neutrino oscillation parameters are generated from random mass matrices given in the flavor symmetry basis. This concept is similar in motivation but somewhat different in implementation from the *anarchy hypothesis*, which postulates the independence of the measure [7].

For this method, we use the "generate-and-tune" method, similar to Ref. [155], to find viable realizations of the neutrino oscillation parameters. We choose $k_i \in [\epsilon, 1/\epsilon]$ with $\epsilon = 0.2$ (motivation becomes clear later in the dissertation) and $M_I \in [0.1, 80]$ GeV randomly with the requirement $M_1 < M_2 < M_3$. Thereafter, the phases ϕ_i and m_D are picked to locally minimize

$$\chi^2 = \left(\frac{\theta_{12} - \theta_{12}^{\text{bf}}}{\sigma_{\theta_{12}}}\right)^2 + \left(\frac{\theta_{13} - \theta_{13}^{\text{bf}}}{\sigma_{\theta_{13}}}\right)^2 + \left(\frac{\theta_{23} - \theta_{23}^{\text{bf}}}{\sigma_{\theta_{23}}}\right)^2 + \left(\frac{\Delta m_{21}^2 - (\Delta m_{21}^2)^{\text{bf}}}{\sigma_{\Delta m_{21}^2}}\right)^2 + \left(\frac{\Delta m_{32}^2 - (\Delta m_{32}^2)^{\text{bf}}}{\sigma_{\Delta m_{32}^2}}\right)^2 , \tag{5.2.4}$$

where we use the best-fit values and 1σ errors of the neutrino oscillation parameters from Ref. [68]. This minimization is performed with Brent's [156] and Powell's methods [157], where an one-dimensional minimizator minimizes along mutually perpendicular directions in the N-dimensional space. This leads the method to the minimum with the smallest possible χ^2 value, see Appendix B for a more detailed description of the minimization procedure. Initial values for the phases and the overall scale of the Dirac mass matrix are needed, and we choose 0 and 2π for the ϕ_is and 10 keV and 300 keV for m_D[4]. If the final value of $\chi^2 < 9$, we keep the realization; otherwise, we discard it.

This procedure does not (necessarily) find a global minimum, however we are interested in parameter sets obeying $\chi^2 \leq 9$. Therefore, any local minimum is also viable compared to the global minimum. Additionally, any perturbation might lead to a different minimum, however as long as χ^2 is satisfied, the parameter set is viable. More critically is the stability of procedure, *i.e.* whether it converges to a local minimum or not. The χ^2 function is a second order polynomial in the oscillation parameters, meaning the procedure strongly converges toward the minimum. We have tested this procedure ourself, perturbing the parameter set, and the same minimum is obtained in all cases, even with a perturbation of 75%. A study finds a similiar result [158]. Therefore, it seems that the minimization method is vigorish. If we minimize a different function, an other outcome is possible. In general, a third order polynomial has a saddlepoint at $x = 0$,

[4]The range for the overall scale of the Dirac mass matrix is obtained by using the scaling $m_D \sim \sqrt{M_I}$ from the seesaw mechanism. Putting $M_I \in [0.1, 80]$ GeV implies $m_D \in [10, 300]$ keV.

however the function has a lower value at $x = \infty$. Introducing a third order polynomial into the χ^2 function, means it behaves differently. Therefore, any perturbation might result in a completely different outcome compared to our case. We have also checked the behavior of a third order polynomial in this minimization procedure, and a small perturbation ($\sim 5\%$) can result in different parameter set. Therefore, the stability of the procedure depends strongly on the function, which one wants to minimize.

5.2.2 Results

We generate realizations with the two different methods. We apply cuts to ensure that they obey experimental limits such as the upper limit on the effective mass of neutrino-less double beta decay $m_{\beta\beta}$, the upper limit on the decay rate of the lepton flavor violating process $\mu \to e\gamma$, and upper limit on the active-sterile mixings. Additionally, the sterile neutrino lifetime has to obey $\tau_N < 0.1$ s, since the observed abundances of light nuclei imply that they must have decayed long before Big Bang nucleosynthesis (BBN). This is supported by good agreement between experimental observations and theoretical computations. We follow Ref. [154] to compute these observables. We keep the set of mass matrices which obeys all experimental constraints, else we disregard them. Especially, the constraints from direct searches and BBN are of importance since they directly exclude parts of the active-sterile mixing parameter space.

Our results for the two methods are displayed in Fig. 5.1 top. We show the total active-sterile mixing of the lightest and heaviest sterile neutrino as a function of their mass, and the dark shading regions are excluded by different experimental constraints. The lower bound comes from BBN since our requirement of $\tau_N < 0.1$ s impacts the total mixing due to the relationship $\tau_N \sim \Gamma_N^{-1} \propto |U_I|^{-2}$. Additionally, a lower bound from the seesaw mechanism is frequently used in the literature. Considering the case with $\mathcal{N} = 2$ sterile neutrinos, fixes a lower bound to [144]

$$|U_I|^2 \gtrsim \frac{m_{\text{atm}}}{M_N} \begin{cases} \frac{m_\odot}{m_{\text{atm}}} & \text{for NO} \\ \frac{1}{2} & \text{for IO} \end{cases}, \tag{5.2.5}$$

where $m_\odot \simeq \sqrt{\Delta m^2_{21}}$, $m_{\text{atm}} \simeq \sqrt{\Delta m^2_{32}}$ for NO, $m_{\text{atm}} \simeq \sqrt{|\Delta m^2_{31}|}$ for IO, and M_N is the overall sterile neutrino mass scale. For $\mathcal{N} = 3$ sterile neutrinos, a lower bound is derived using the Casas-Ibarra parameterization [159]

$$|U_I|^2 \geq \frac{m_{\text{min}}}{M_I}, \tag{5.2.6}$$

where m_{min} is the lightest active neutrino mass. However, m_{min} can be as low as zero, meaning

the seesaw bound is, in general, weaker than the BBN bound. Therefore, we omit the seesaw bound here. Direct search experiments sets an upper limit on the active-sterile mixings; a review of the different experimental bounds is given in Ref. [154]. The flavored mixing elements $|U_{eI}|^2$ and $|U_{\mu I}|^2$ are well constrained in the mass range $0.1 - 2$ GeV with decreasing sensitivity for increasing mass, whereafter they reach a plateau at about $2 - 100$ GeV reported by the DELPHI Collaboration [160]. The mixing element $|U_{\tau I}|^2$ lacks the same stringent limit, and it is best constrained by the same plateau mentioned before. It has a worse limit due to the tau production threshold, meaning it is difficult to identify the tau neutrino by its associated charged lepton. As a consequence, we set the upper bound on the total mixing to be the $|U_{\tau I}|^2$ limit since this mixing element typically limits the sensitivity. The theoretical predictions are compared to the expected sensitivity of FCC only, since it measures the total mixing directly. We are not aware of any sensitivity studies from SHiP and DUNE on the total mixing in the absence of any assumptions, meaning we do not show their corresponding bounds[5].

Similar mixings are predicted by the two methods, and they occupy the same part of the parameter space. In principle, they can generate the whole shown parameter space (*cf.*, [154]), however it requires some fine-tuning. Expressing the total mixing using the Casas-Ibarra parameterization, we get [159]

$$|U_I|^2 = \frac{1}{M_I} \sum_{j=1}^{3} m_j |\mathcal{R}_{jI}|^2 \,, \tag{5.2.7}$$

where M_I is the sterile neutrino mass, m_j is the light neutrino mass, and $\mathcal{R}_{jI}$ is the matrix element in the matrix $\mathcal{R}$. For $\mathcal{N} = 2$ sterile neutrinos, $\mathcal{R}$ depends on one complex angle only, and the matrix element is $\mathcal{R}_{jI} \propto e^{|\mathrm{Im}(\omega)|}$ when $|\mathrm{Im}(\omega)| > 1$ [126, 144, 154]. Therefore, assuming $|\mathrm{Im}(\omega)| \gg 1$ means, in general, a large total active-sterile mixing. In our models with $\mathcal{N} = 3$ sterile neutrinos, the matrix elements behave similarly, but we have three complex angles rather than one. Having $|\mathrm{Im}(\omega)|$ (either one or multiple angles) too large, leads to violation of the upper experimental active-sterile mixing bound. Therefore, some fine-tuning is required to obtain predictions in the upper area of the parameter space.

Assuming specific relationships among the flavored mixings, means better constraints from the experiments. Here, the total mixing sensitivity is not necessarily limited by $|U_{\tau I}|^2$ if the tau element does not contribute significantly to the total mixing. We use the assumption of case 2 (Eq. (5.1.2)) in the following for illustrative purposes, meaning the sensitivity to the total

[5] A bound on the total mixing can be derived from the information of $|U_{eI}|^2$ and $|U_{\mu I}|^2$ if the $|U_{\tau I}|^2$ contribution is known. In the absence of any assumption, no sensitivity can be derived since $|U_{\tau I}|^2$ is not measured. A limit on the active-sterile mixing can be measured directly from processes such as $N_I \to \eta\nu \to \pi^+\pi^-\pi^0 + p^{\mathrm{miss}}$, however it may be weaker than the bounds frequently shown in the literature.

mixing is dominated by the muon flavor[6]. We take this assumption of the relationship among the individual active-sterile mixing elements into account in Fig. 5.1 bottom. Our predictions do generally follow the upper bound because the models are constrained by the upper limits on the flavored mixings from direct search experiments. However, the total mixing predictions are not produced using this active-sterile mixing ratio and can therefore violate it. Since we take the specific ratio among the flavored mixings into account, bounds from the SHiP and DUNE experiments are included now, as the individual mixing sensitivities can be translated into the total mixing sensitivity. These sensitivities should be interpreted with respect to the experimental limits. In the mass range $M \leq 2$ GeV, it is possible to improve the current total mixing bound by 2 orders of magnitude by SHiP, whereas it is frequently mis-interpretated in the literature when comparing them together with other bounds without taking the flavor mixing ratio assumptions into account. For the lower (BBN) bound, a ratio among the flavored mixing elements do not play a major role since it depends on the total mixing only. How the mixing is distributed into the three sectors is irrelevant, just as long that the total mixing is large enough so that $\tau_N < 0.1$ s.

5.3 Model-dependent view of total mixings

Flavor symmetries can explain the observed neutrino masses and mixings from first principles, and they usually leave an imprint of the size on the mass matrix entries. We investigate this in the lepton sector in the context of the FN mechanism, where the mass matrix entry size is given by the Cabibbo angle. Thereafter, we study the active-sterile mixings as they serve as model discriminators, making it possible for future experiments to distinguish between different scenarios.

5.3.1 The Froggatt-Nielsen mechanism in the lepton sector

We construct mass matrices in the lepton sector with the FN mechanism [162, 163], and we consider a flavor symmetry given by a direct product of cyclic groups, *i.e.* $\mathcal{G}_\mathcal{F} = Z_{n_1} \times Z_{n_2} \times ... Z_{n_m}$.

[6] Using the ratio in case 2 (Eq. (5.1.2)), one can derive each flavor's contribution to the upper total mixing bound

$$\frac{|U_{eI}|^2}{|U_I|^2} : \frac{|U_{\mu I}|^2}{|U_I|^2} : \frac{|U_{\tau I}|^2}{|U_I|^2} = 0.05 : 0.77 : 0.18. \tag{5.2.8}$$

The well-constrained electron and muon flavors are typically dominating when translating the individual bounds to the total mixing bound. Considering the case with a sterile neutrino mixing *only* with the tau flavor, means the upper bound will come directly from the upper bound on the tau mixing element.

The charge assignment of the leptons is

$$(e_R)_i \sim (p_1^i, p_2^i, ..., p_m^i) = \boldsymbol{p}^i\,, \quad \ell_i \sim (q_1^i, q_2^i, ..., q_m^i) = \boldsymbol{q}^i\,, \quad (N_R)_i \sim (r_1^i, r_2^i, ..., r_m^i) = \boldsymbol{r}^i \tag{5.3.1}$$

for the right-handed lepton $(e_R)_i$, the lepton doublet ℓ_i and the sterile neutrino $(N_R)_i$, respectively. The jth entry in each row vector denotes the Z_{n_j} charge of the particle, $i = 1, 2, 3$ is the generation index, m is the number of Z_n factors, and n_k $(k = 1, 2, ..., m)$ may be different. Therefore, using the FN mechanism as explained in Subsection 4.3.2, the lepton mass Lagrangian becomes

$$\begin{aligned}\mathcal{L}_{\text{lepton}} = &-\left(\prod_{k=1}^{m}\epsilon^{\alpha_{ij}^k}\right) x_{ij} H^* \ell_i (e_R)_j - \left(\prod_{k=1}^{m}\epsilon^{\beta_{ij}^k}\right) y_{ij} \tilde{H} \ell_i (N_R)_j \\ &- \frac{1}{2} m_R \left(\prod_{k=1}^{m}\epsilon^{\gamma_{ij}^k}\right) z_{ij} (N_R)_i (N_R^c)_j + \text{h.c.}\,,\end{aligned} \tag{5.3.2}$$

where x, y, z are independent order unity complex numbers, $\tilde{H} = i\sigma^2 H$ and $\epsilon \simeq v_f/M_F$ is a remnant from integrating out the flavons and the superheavy fermions. Therefore, the mass matrices will depend on the control parameter ϵ, and this leads to effective SM lepton masses that are suppressed by ϵ. The lepton mass matrix elements are given by

$$(M_\ell)_{ij} \simeq v \prod_{k=1}^{m}\epsilon^{\alpha_{ij}^k} x_{ij}\,, \quad (M_D)_{ij} \simeq m_D \prod_{k=1}^{m}\epsilon^{\beta_{ij}^k} y_{ij}\,, \quad (M_R)_{ij} \simeq m_R \prod_{k=1}^{m}\epsilon^{\gamma_{ij}^k} z_{ij}\,, \tag{5.3.3}$$

where v is the Higgs VEV and m_D (m_R) is the overall scale of the Dirac (Majorana) mass matrix. The exponent is given by the quantum numbers assigned to the leptons

$$\alpha_{ij}^k = \min[(p_i^k + q_j^k) \bmod n_k, (-p_i^k - q_j^k) \bmod n_k], \tag{5.3.4}$$

$$\beta_{ij}^k = \min[(q_i^k + r_j^k) \bmod n_k, (-q_i^k - r_j^k) \bmod n_k], \tag{5.3.5}$$

$$\gamma_{ij}^k = \min[(r_i^k + r_j^k) \bmod n_k, (-r_i^k - r_j^k) \bmod n_k]. \tag{5.3.6}$$

Therefore, the structure of the mass matrices (texture) arise as the leading order products of ϵ. One uses the term "texture" since it captures the overall magnitude of each matrix element and the mass matrix structure. Using this method, mass matrices such as those in Tab. 5.1 are obtained. For further in-depth discussion about the complete procedure of deriving the texture sets, see Refs. [80, 162, 163]. These texture sets are the basis of this analysis[7], and we study their active-sterile mixings and compare them to expected sensitivities.

[7] Note that we checked all examples from Ref. [163] but only show a few examples here for illustration.

#	$Y_\ell = M_\ell/v$	M_D/m_D	M_R/m_R	$\mathcal{G}_\mathcal{F}$
15	$\begin{pmatrix} \epsilon^4 & \epsilon^4 & \epsilon^2 \\ \epsilon^3 & \epsilon^4 & 1 \\ \epsilon^3 & \epsilon^2 & 1 \end{pmatrix}$	$\begin{pmatrix} \epsilon^2 & \epsilon & \epsilon^3 \\ \epsilon^2 & \epsilon & \epsilon^2 \\ \epsilon & \epsilon^2 & 1 \end{pmatrix}$	$\begin{pmatrix} \epsilon^2 & \epsilon^2 & \epsilon \\ \epsilon^2 & \epsilon & \epsilon^2 \\ \epsilon & \epsilon^2 & 1 \end{pmatrix}$	$Z_5 \times Z_7$
19	$\begin{pmatrix} \epsilon^4 & \epsilon^4 & \epsilon^2 \\ \epsilon^2 & \epsilon^2 & \epsilon^2 \\ \epsilon^4 & \epsilon^2 & 1 \end{pmatrix}$	$\begin{pmatrix} \epsilon & \epsilon^2 & \epsilon \\ \epsilon & 1 & \epsilon \\ \epsilon & 1 & \epsilon \end{pmatrix}$	$\begin{pmatrix} \epsilon & \epsilon^2 & \epsilon^5 \\ \epsilon^2 & 1 & \epsilon^3 \\ \epsilon^5 & \epsilon^3 & 1 \end{pmatrix}$	$Z_5 \times Z_6$
22	$\begin{pmatrix} \epsilon^4 & \epsilon^3 & \epsilon^2 \\ \epsilon^2 & \epsilon^2 & \epsilon^3 \\ \epsilon^5 & \epsilon & 1 \end{pmatrix}$	$\begin{pmatrix} \epsilon^2 & \epsilon & \epsilon^2 \\ 1 & \epsilon & 1 \\ 1 & \epsilon^3 & 1 \end{pmatrix}$	$\begin{pmatrix} 1 & \epsilon^3 & 1 \\ \epsilon^3 & \epsilon & \epsilon^3 \\ 1 & \epsilon^3 & 1 \end{pmatrix}$	$Z_3 \times Z_9$

Table 5.1: Selected examples for texture sets Y_ℓ, M_D, and M_R from flavor models [163], where the numbering of each texture set is kept from the original article. The last column shows the flavor symmetry extension of the SM symmetry, *i.e.*, $\mathcal{G}_\text{SM} \times \mathcal{G}_\mathcal{F} = SU(3) \times SU(2) \times U(1) \times \mathcal{G}_\mathcal{F}$, that realizes the structure of the matrices.

We set $\epsilon = 0.2$ such that the textures explains the mass spectrum for the charged leptons and neutrinos, however each matrix element has the freedom of an independent order one complex number c_{ij} (feature of the FN framework) with $|c_{ij}| = k_{ij}$ and $\arg(c_{ij}) = \phi_{ij}$ (before we used x, y and z as complex numbers in the lepton mass Lagrangian Eq. (5.3.2)). We need 24 complex numbers, the charged lepton Yukawa matrix and the Dirac mass matrix need 9 each, whereas the Majorana mass matrix only needs 6 due to the constraint $M_R = M_R^T$. The magnitude of the order one complex number cannot be arbitrary, since one could erase the structure of the mass matrices with the complex order one number. Therefore, we choose $k_i \in [\epsilon, 1/\epsilon]$, so each order one number can maximally change each matrix entry by one order of magnitude. This is the reason for our choice of $k_i \in [\epsilon, 1/\epsilon]$ in Section 5.2. The predicted parameter space for the HNLs is (roughly) a direct consequence of the flavor symmetry since it controls the magnitude of the matrix entries, which, in turn, controls the active-sterile mixings. The overall scale of the Majorana mass matrix is given by the interval $m_R \in [0.1, 100]$ GeV since we are interested of GeV sterile neutrinos. We use the "generate-and-tune" method introduced previously to obtain values for the phases ϕ_i and the overall scale of the Dirac mass matrix m_D. We use the same initial value range for the phases, however it is different for m_D since the Majorana mass matrix is non-diagonal. We choose the initial value range $m_D \in [0.5\sqrt{m_R}, 1.5\sqrt{m_R}]$ where the coefficients gives more freedom to the minimization compared to fixing $m_D = \sqrt{m_R}$. Even with this procedure, we are not guaranteed that the masses of the sterile neutrinos are in the interval

of interest, *i.e.* $M_I \in [0.1, 80]$ GeV. Therefore, we use the scaling symmetry

$$M_R \to z M_R \,, \qquad M_D \to \sqrt{z} M_D \tag{5.3.7}$$

with z being a real number if one (or multiple) masses are outside of the interval $M_I \in [0.1, 80]$ GeV.

In the minimization routine, we vary the phases and the Dirac mass scale to locally minimize the χ^2. In a general procedure, one would vary the magnitude of the complex number in addition, possibly obtaining a parameter set with a lower χ^2. However, this erases the structure in the mass matrix since one cannot control their final value. Additionally, the minimization procedure would take more time due to the larger parameter space. Therefore, we keep using the minimization procedure described previously.

5.3.2 Results

Our results are shown in Fig. 5.2 top, displaying each realization of the model predictions as dots. Lower and upper limits are given by BBN and direct search experiments, respectively. Again, the experimental sensitives assumes a specific ratio among the flavored mixings, meaning the model predictions can violate the upper bound since they are not produced under this assumption. However, they follow the trend of the upper bound.

The model predictions from the three different texture scenarios are shown, displaying the flavor symmetry's impact on the active-sterile mixings. Texture 15 tends to be within reach of future experiments, whereas texture 19 produces small mixings beyond this reach. Texture 22 is partially within reach. Therefore, the total active-sterile mixings can be used as a model discriminator, even though some of the cases are indistinguishable based on the total mixing as an observable only. One can deduce that all flavored mixing elements $|U_{\alpha I}|^2$ have to be small if the total mixing is small due to $|U_\alpha|^2 \leq |U_I|^2$, however it is more difficult in a scenario with large total mixings. Therefore, we study the individual flavor-dependent mixing elements in Section 5.4.

In our models, we introduce $\mathcal{N} = 3$ sterile neutrinos at the GeV scale, and each of them can be found experimentally. In case of degenerate sterile neutrinos, each experiment can discover all of them. However in the general case, the experiments are complementary to each other when excluding model predictions. As an example, we use texture 15, and we study DUNE's complementary to SHiP and FCC, even though it could be any of the texture sets and experiments. The model predictions of texture 15 within reach of DUNE are shown in red in Fig. 5.2 bottom left, whereas the blue points represent the predictions not within reach. This leads to two subsets of the model predictions for texture 15, and we study the heaviest sterile neutrino for both

subsets, as shown in Fig. 5.2 bottom right. Model predictions from both subsets occupy the region probed by FCC, thereby showing the complementary among the experiments. Therefore, excluding model predictions for the lightest sterile neutrino has consequences for the other two sterile neutrinos. In general, combining all bounds from DUNE, SHiP and FCC while including all three sterile neutrinos into the discussion, gives the strongest upper bound and excludes the most model predictions. Even in this situation, some cases cannot be excluded, and more sensitive experiments or experiments with the production of the sterile neutrinos from B-mesons are needed [136]. B-factories can probe the part of the parameter space situated between the SHiP and FCC bounds at mass range $3 - 7$ GeV, thereby closing this spot in the parameter space.

5.4 Flavor-dependent active-sterile mixings

In this section, we discuss the flavored active-sterile mixings $|U_{eI}|^2$ and $|U_{\mu I}|^2$ in both approaches[8], and compare the predictions to the experimental sensitivities.

In figure Fig. 5.3, no lower limit exist on the individual mixing elements since one can be very small if the others compensate for it, ensuring the lifetime constraint $\tau_N < 0.1$ s. While the FCC experiment is insensitive to the flavored mixings, their bound is still applicable since constraining the total mixing also limits the individual mixing. Therefore, we use the same sensitivity on the flavored mixings as on the total mixings. Additionally, we do not assume any specific ratio among the active-sterile mixings in the exclusion bounds as indicated by the statement "Assumption: None" in the top of the figure, meaning we use the appropriate sensitivities with a single dominating flavor for the SHiP and DUNE experiments. In this section, we focus on the lightest sterile neutrino only since SHiP and DUNE are most sensitive to this sterile neutrino (FCC is more sensitive to heavier sterile neutrinos). Additionally, their planned starting date is sooner than that of FCC.

Considering the model-independent approaches in Fig. 5.3 top, the Casas-Ibarra parameterization and the random case produces, in principle, the same region of the parameter space, even though the Casas-Ibarra parameterization occupies more of the parameter space. Additionally, some fine-tuning is needed to obtain large mixings (explained previously), and extremely small mixings are rarely predicted since it requires cancellations among the different terms in the flavored mixings. It seems that the muon flavored mixings are better probed, however SHiP and DUNE is also probing a large fraction of the electron flavored mixing parameter space. The

[8] In the SHiP and DUNE experiments, the main source of sterile neutrinos comes from charmed hadrons. They have similar mass as the tau-lepton, meaning $|U_{\tau I}|^2$ will contribute to the sterile neutrino production only due to the small mass difference between the charm meson and the tau-lepton. Therefore, it is considered irrelevant for subsequent sterile neutrino decays [164, 165], meaning we omit the mixing element $|U_{\tau I}|^2$ in this discussion.

FCC experiment is still excluding model predictions in spite it is intended to search for heavier sterile neutrinos. Note that no realizations are above the upper bound, since it directly applies here.

Discussing the model-dependent method, the flavored mixings are shown in Fig. 5.3 bottom. Interestingly, we observe the impact of the flavor symmetry on these observables. For example, texture 22 produces large mixing in the muon channel, whereas it is suppressed in the electron channel. Quite differently, large mixings are predicted by texture 15 for both the electron and the muon mixing elements. This example demonstrates that the information from different channels can be used as a model discriminator and tell something about the structure of the mass matrices.

5.5 Limitations, extensions, and outlook

There is no dark matter candidate in our models since we introduce three GeV sterile neutrinos. However, one could incorporate a fourth keV sterile neutrino or some other candidate, *i.e.* Weakly Interacting Massive Particles (WIMPs) or axions, as dark matter. There are limited constraints concerning the number of sterile neutrinos and their mass scale, which can easily be evaded, meaning it is a valid option to introduce a keV sterile neutrino. However, it has to be very weakly interacting due to experimental constraints, meaning it will not influence our computation. However, one has to explain the extra mass generation since it no longer reflects the symmetry seen in the quark sector. Considering WIMPs or axions, one can incorporate them without influencing our calculation since they do not (usually) interact with neutrinos. WIMPs are usually considered in many supersymmetry (SUSY) models with masses of $\sim$ 100GeV $-$ 10TeV [166, 167]. A different possibility is the axion, and estimates show it will have a μeV mass [168–170].

We did not compute the baryon asymmetry in our computation, however comparing the allowed νMSM parameter space in Fig. 4.2 with our model parameter space, one sees that they overlap. At the same time, our model parameter space is larger since we consider three GeV sterile neutrinos, meaning there are more possibilities in generating the baryon asymmetry. Therefore, it is, in principle, possible to generate the baryon asymmetry in our models. Since we introduce three GeV sterile neutrinos, means our case is not minimalistic as the νMSM. However, no mass degeneracy among the sterile neutrinos is needed in our case (meaning no fine-tuning problem).

Comparing the different experiments DUNE, SHiP, and FCC, a discussion about their strengths and weaknesses seem justified since it might be that only one (if none at all) is built in the end. SHiP's main competitor is DUNE in the context of searching for GeV sterile neutrinos due to

their similar sensitivity bounds. Therefore, it might be difficult to argue for the contruction of both experiments, meaning it is very important for both Collaborations to argue in favor of their experiment. The DUNE experiment is a prime candidate to measure the neutrino mass ordering and CP violation in the lepton sector, which are two observables needed to complete the 3ν framework. A possible drawback is DUNE's liquid-argon based detectors, which is a new experimental technology compared to the water-cherenkov based detectors. Therefore, experimental development of this new technology has to take place before building the detector [171, 172]. Additionally, there is no cost estimate and starting date of DUNE, but the Collaboration pursues a scope of work, cost, and time schedule by year 2020 [173]. Considering the SHiP experiment, it is based on current technology [143], meaning no research and development (R&D) has to take place in comparison to the DUNE experiment. At the same time, SHiP is suppose to start data taking by year 2025. According to its technical proposal [143], the complete cost of SHiP is roughly 200 million USD, divided into 136 million USD for the facility housing the experiment and 59 million USD for the detector [143]. However, SHiP seems limited in the context in a world-wide plan, whereas DUNE plays a central role in Fermilab's decision to focus on neutrino physics in the future with many new experiments. The FCC experiment is in a different class compared to DUNE and SHiP, especially cost-wise. It is a vision as the next step in the physics program at CERN. First of all, FCC is suppose to start much later than DUNE and SHiP, but it will explore a different part of the parameter space. Secondly, it starts as a lepton collider, whereafter it is turned into a hadron collider, meaning there are many uses for this experiment in a world-wide plan. One can explore the Higgs boson's couplings, flavor physics, and supersymmetry over a large energy range. However, the cost is emens, meaning each country in the CERN Collaboration has to invest a huge amount for many years. In summary, there are various strengths and weaknesses for the different experiments, and we will see in the future whether they are build or not.

Considering the texture sets in Tab. 5.1, there are many theory parameters entering the analysis, *i.e.* magnitude and phase of 24 complex numbers together with two mass scales. However, one could perform the same analysis with less theory parameters by assuming $\mathcal{O}(\epsilon^2) \simeq 0$ or $\mathcal{O}(\epsilon) \simeq 0$. Considering the mass matrices to a certain order of ϵ, smaller matrix entries are set to zero. Consequently, a higher predictability of the different observables is possible, however it might be that the texture sets cannot generate the neutrino oscillation parameters within their experimental range. Therefore, one might exclude some of the texture sets when assuming $\mathcal{O}(\epsilon^2) \simeq 0$ or $\mathcal{O}(\epsilon) \simeq 0$. This could be an improvement of the analysis compared to the original work, and one could pursue this in the future.

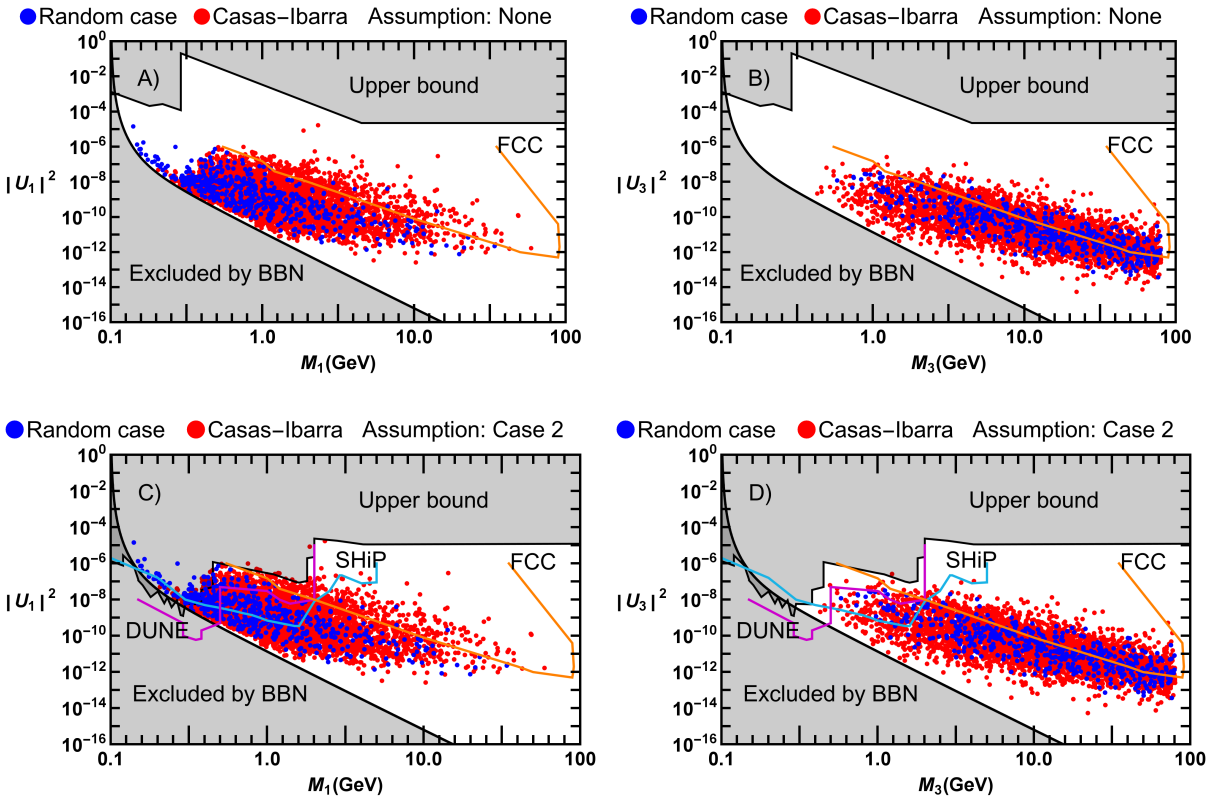

Figure 5.1: Total active-sterile mixing predictions for the lightest and heaviest sterile neutrino for the Casas-Ibarra parameterization (red points) and random case (blue points), where one dot represents one model. The sensitivities are from the experiments DUNE (purple), SHiP (cyan) and FCC (orange). A&B) No assumptions has been imposed on the ratio of the flavored mixings (indicated by "Assumption: None"), meaning SHiP and DUNE sensitivities are not displayed. C&D) Experimental bounds are shown for the assumption $|U_{eI}|^2 : |U_{\mu I}|^2 : |U_{\tau I}|^2 = 1 : 16 : 3.8$ (indicated by "Assumption:Case 2"). Figure taken from Ref. [161].

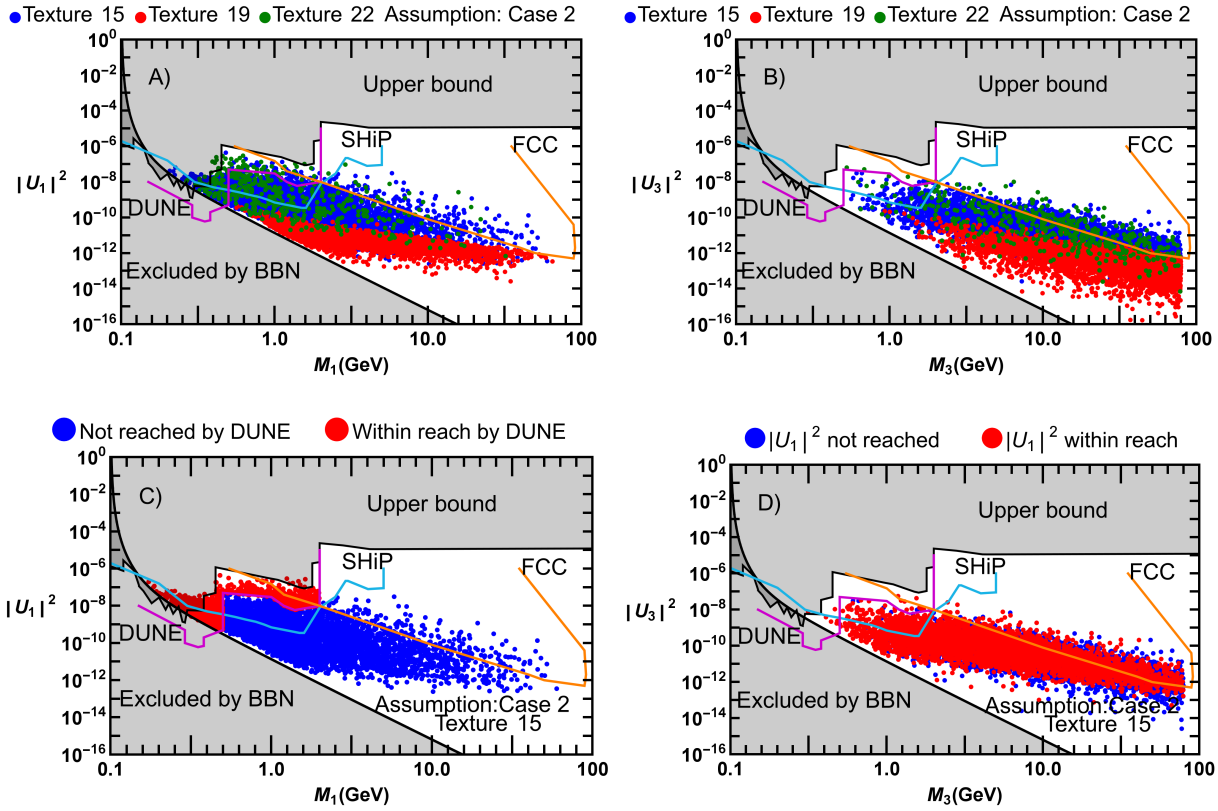

Figure 5.2: A&B) Similar to Fig. 5.1A&B) for the predictions of the total active-sterile mixings of the lightest and heaviest sterile neutrino from different texture sets (colors); see the figure legend. C&D) Complementary among the different experiments using texture 15 as an example. The red (blue) points are the model predictions with the mixing $|U_1|^2$ (not) reachable by the DUNE experiment, and the corresponding model predictions of $|U_3|^2$ for the same model, thereby showing that DUNE can exclude model predictions for the heaviest sterile neutrino which are out of reach by FCC, and vice versa. Figure taken from Ref. [161].

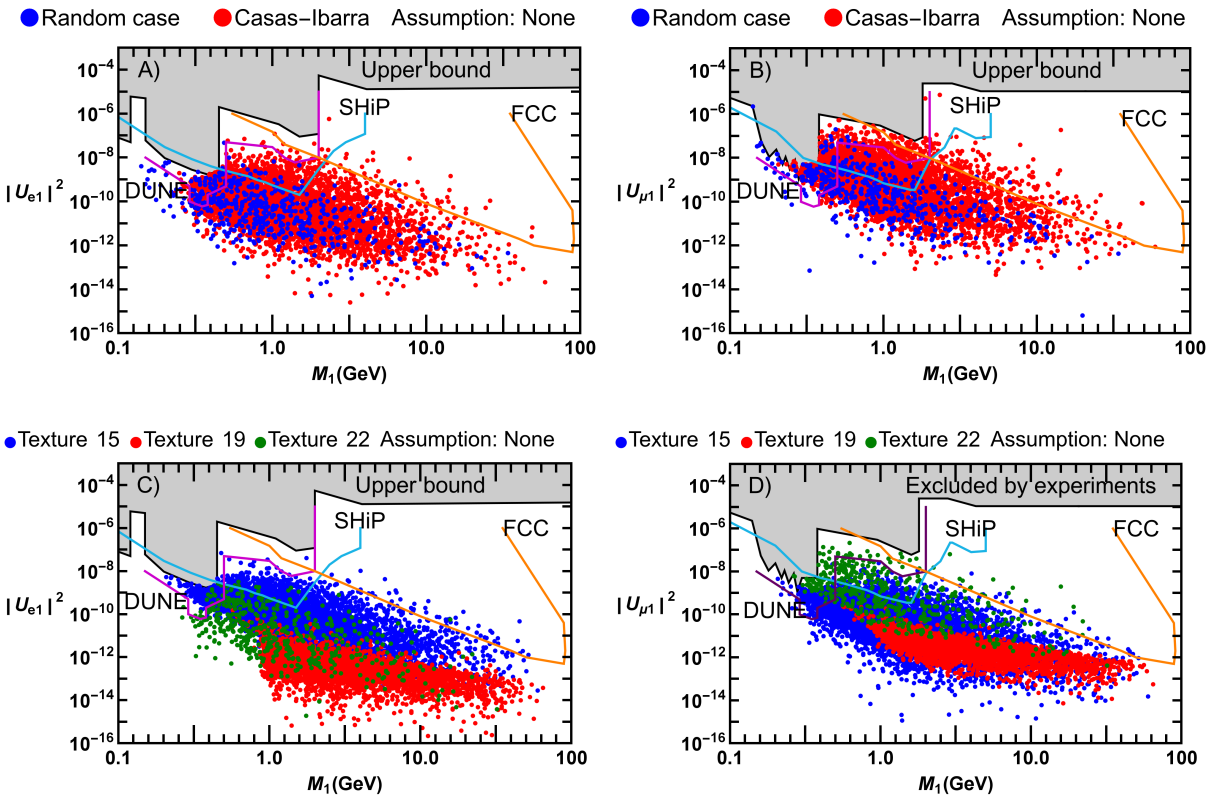

Figure 5.3: The flavored active-sterile mixings ($|U_{eI}|^2$ and $|U_{\mu I}|^2$) for the lightest sterile neutrino only. The upper bound from direct search experiments is shown as well, whereas no lower bound exists for three generations of sterile neutrinos (since one mixing element can be very small if an other is large enough to ensure the sterile neutrino lifetime bound from BBN. A&B) Model predictions for the Casas-Ibarra parameterization and random case. C&D) Model predictions for the different texture models. Figure taken from Ref. [161].

Chapter 6

Non-Abelian symmetries for Cabibbo mixing

In the previous chapter, we saw the use of Abelian flavor symmetries and their impact on the active-sterile mixings. However, it lacks the full quantization of the mixing matrix since it depends on a control parameter ϵ (indirectly from the mass matrices). We fix this parameter by hand (a good estimate is $\epsilon \simeq 0.22$). Using non-Abelian symmetries as the parent symmetry evades this issue, thereby allowing for precise predictions of the mixing matrix. Additionally, coupling it with other symmetries, helps organizing the fermion mass patterns. Therefore, we discuss non-Abelian flavor symmetries in this chapter.

We investigate Cabibbo mixing in the quark sector by utilizing a method, which effectively inverts the arrows in Eq. (4.2.2). We start by identifying the residual symmetries in the SM quark Yukawa sector, and thereafter we build the generators, which represents the symmetry. The generators depend on the same degrees of freedom which are present in the mixing matrices by construction, thereby linking the physical observables to the symmetry charge assignments. Scanning over these degrees, we obtain different combinations of the symmetry generators, whereafter we close the groups generated by the generators using the computational GAP program[1]. We consider small ordered groups that can predict the Cabibbo angle to leading order, meaning we adopt the philosophy explained previously in Section 4.5, suggesting that corrections might shift the leading order prediction value to the experimentally allowed range. This approach of "[re]constructing" finite flavor groups realizes an automation of the studies performed previously [174–177]. The authors of Ref. [178] considered the bottom-up approach in a non-automated fashion. This particular method is useful as a model-building tool since it identifies possible symmetries capable of describing the observed oscillation parameters.

6.1 Residual symmetries of the quark mass sector

The residual symmetries present in the SM Lagrangian is the starting ground to identify the original non-Abelian flavor symmetry, and several studies have investigated this issue both

[1] http://www.gap-system.org/. We use GAP4.7.

analytically and numerically over the last couple of years. The quark mass Lagrangian is given by [175]

$$-\mathcal{L} = \bar{U}_R \hat{M}_U U_L + \bar{D}_R M_D D_L + h.c.\,, \tag{6.1.1}$$

where $U_{L,R} \equiv (u,c,t)^T_{L,R}$, $D_{L,R} \equiv (d,s,b)^T_{L,R}$ and $\hat{M}_U \equiv diag\{m_u, m_c, m_t\}$. Hence, we choose the basis where the up quark mass matrix is diagonal. We identify the residual symmetries $\mathcal{G}_\mathrm{u}$ and $\mathcal{G}_\mathrm{d}$ from the quark mass Lagrangian, and for each mass generation, it remains invariant under a $U(1)$ symmetry. Therefore, the natural residual symmetry of both the up and down quark mass terms is $U(1)^3$, a product of the three $U(1)$ coming from each generation. We are currently only interested in discrete flavor symmetries, meaning we focus on discrete cyclic subgroups and their direct products

$$\mathcal{G}_\mathcal{Q} \to \begin{cases} \mathcal{G}_u \sim Z^u_n,\ Z^u_{n_1} \times Z^u_{n_2} \\ \mathcal{G}_d \sim Z^d_m,\ Z^d_{m_1} \times Z^d_{m_2} \end{cases} . \tag{6.1.2}$$

We investigate the different possible scenarios of the residual symmetries being a single cyclic group Z_n, a direct product $Z_n \times Z_m$ or a combination thereof. We choose these combinations since they are frequently choices in the lepton sector [179]. The residual symmetries transforms the left-handed fields by[2]

$$U_L \to T_l U_L\,, \quad D_L \to S_{Di} D_L\,, \tag{6.1.3}$$

where T_l (S_{D_i}) denotes the generator(s) of $\mathcal{G}_u$ ($\mathcal{G}_d$). The generator T_l is given by

$$T_l = \mathrm{diag}\left(e^{i\Phi_1}, e^{i\Phi_2}, e^{i\Phi_3}\right)_l\,, \tag{6.1.4}$$

where $\Phi_j = 2\pi\frac{\phi_j}{n}$. It has this form since we choose a basis, where the up quark mass matrix is diagonal. We treat ϕ_j and n as integers in our method (described later), and n represents the order of the generator T_l. The generator S_{Di} is rotated due to non-diagonal down quark mass matrix. In turn, it explicitly depends on the parameters in the unitary mixing matrix

$$S_{Di}(\{\Theta_k, \alpha_j\}) = U_{CKM}(\Theta_k)\, S_i(\alpha_j)\, U^\dagger_{CKM}(\Theta_k)\,, \tag{6.1.5}$$

where S_i are diagonal matrices analogous to Eq. (6.1.4) with phases α_j, and $\{\Theta_k\}$ are whatever mixing angles and CP-violating phases are present in U_{CKM}. We have the experimental allowed

[2] No physical right-handed mixing occurs in the SM, meaning their transformation properties are not important for this discussion.

range for the CKM mixing matrix elements [20]

$$|U_{\rm CKM}| \simeq \begin{pmatrix} 0.9741 - 0.9744 & 0.2248 - 0.2260 & 0.0034 - 0.0037 \\ 0.2246 - 0.2258 & 0.9733 - 0.9736 & 0.0402 - 0.0426 \\ 0.0085 - 0.0092 & 0.0393 - 0.0416 & 0.9991 - 0.9992 \end{pmatrix}. \tag{6.1.6}$$

This shows the explicit hierarchical nature of the quark mixing matrix, also displayed in Fig. 3.4. It is evident from Eq. (6.1.6) that the off-diagonal elements are one to two orders smaller in magnitude than the diagonal elements, and the upper 2×2 sub-matrix approximates nearly an $SO(2)$ rotation about the Cabibbo angle

$$U_{\rm CKM}^{\rm LO} \simeq \begin{pmatrix} \cos\theta_C & \sin\theta_C \\ -\sin\theta_C & \cos\theta_C \end{pmatrix}. \tag{6.1.7}$$

Considering the numerical values of Eq. (6.1.6) together with the null result from previous studies searching for discrete groups quantizing the full CKM mixing matrix, means studying Eq. (6.1.7) only with our bottom-up technique (discussed below) makes sense. By using Eq. (6.1.7) and Eq. (6.1.5), we find the explicit forms for the effective 2-generation of S_{D_i} to be

$$S_{D_i} = \begin{pmatrix} e^{i\alpha_{1i}}\cos^2\theta_C + e^{i\alpha_{2i}}\sin^2\theta_C & (e^{i\alpha_{2i}} - e^{i\alpha_{1i}})\cos\theta_C\sin\theta_C \\ (e^{i\alpha_{2i}} - e^{i\alpha_{1i}})\cos\theta_C\sin\theta_C & e^{i\alpha_{2i}}\cos^2\theta_C + e^{i\alpha_{1i}}\sin^2\theta_C \end{pmatrix}. \tag{6.1.8}$$

Having the charge assignment $\mathcal{G}_d \sim Z_m^d$ and not a direct product, means the index i is meaningless.

6.2 A bottom-up approach for closing flavor symmetry groups

Our procedure for finding non-Abelian discrete symmetries are discussed. After identifying the residual Abelian symmetries in the up and down sectors, we use a bottom-up method [111] to search for the non-Abelian symmetries by examining the possible groups closed by the combination of their associated generators.

Our script follows the basic steps:

1. **Discretization:** We have to discretize the continuous degrees of freedom $\{\Theta_k\}$ since our

generators depend on them. We use the discretization[3]

$$\Theta_k = c\pi\,, \tag{6.2.1}$$

where $c \equiv a/b$ and $(a, b) \in$ Integers. Here, we discretize the angle itself, however insisting that $\Theta \in [0, 2\pi]$ to avoid any degeneracies, meaning $a \leq 2b$. We have 3-5 degrees of freedom in the down sector,$\{\alpha_{1i}, \alpha_{2i}, \theta_C\}$, and 2-4 degrees of freedom in the up sector,$\{\phi_{1l}, \phi_{2l}\}$. We scan over different ranges of the parameters (a, b), and, as a consequence, the number of potential closed groups grows for increasing ranges of (a, b). For all phases α and ϕ, we restrict ourself to $a \in \{-1, 0, 1\}$ and $b \in \{2, ..., \text{Max}[\mathcal{O}(T_l, S_i)]\}$. For diagonal matrices, the parameter b represents the order of the generator. Its range starts at two in order to avoid degeneracies, and its maximum value is user-defined (specified below for each scans).

2. **Experimental Constraints:** With this huge parameter space, we use experimental data to constrain it in order to find groups which quantize phenomenologically mixing parameters. We apply the most general constraint on the matrix element

$$\min\left[|(U_{\text{CKM}})_{ij}|^2\right] \;\leqq\; |(U_{\text{CKM}}(c_k))_{ij}|^2 \;\leqq\; \max\left[|(U_{\text{CKM}})_{ij}|^2\right]\,, \tag{6.2.2}$$

where we use experimental data from Ref. [20]. Describing this in words, the matrix element cannot be greater (smaller) than the largest (smallest) experimentally determined element of U_{CKM}, since discrete groups can predict entries in the mixing matrix, however not their placement. Therefore, one can constrain *matrix elements* within an arbitrary number of sigmas, but not predict the mixing angles within the same number of sigmas, and an additional cut is required at the end of the search. In the lepton sector, it is a common practice to choose the mixing element U_{e3} as the smallest entry since it is the smallest according to observation for the standard parameterization of the neutrino mixing matrix. However in our case with the effective 2×2 mixing matrix $U^{\text{LO}}_{\text{CKM}}$, we take the off-diagonal elements as the smaller entries, just as suggested by observation. Therefore, no ambiguities of placing the matrix elements amongst row and columns are present.

3. **GAP Implementation:** We use the program GAP, which computes the generators, and whether a group closes or not. Therefore, we translate our parameterization of Θ_k into

[3] Our parameterization Eq. (6.2.1) is an inclusive scheme to discretize mixing angles for both quarks and Dirac neutrinos in the context of finite subgroups of $SU(3)$ [116]. Therefore, we consider this parameterization in this study only. Note, however, at least one relevant counterexample is $\tan(\Theta_k) = \sqrt{\frac{c}{1-c}}$ with $c = \frac{1}{3}$, leading to the TBM mixing matrix [111].

GAP objects[4]

$$\cos(c) = \frac{E(2b)^a + E(2b)^{-a}}{2}, \quad \sin(c) = \frac{E(2b)^a - E(2b)^{-a}}{2E(4)}, \tag{6.2.4}$$

where E returns the primitive N-th root of unity, $E(N) \equiv e^{\frac{2\pi i}{N}}$.

4. **Generator Formation:** Form the explicit representations of the generators T_l Eq. (6.1.4) and S_{Di} Eq. (6.1.8) via Eq. (6.2.4).

5. **Close the Groups:** With the representations of T_l and S_{Di} given by GAP for a specific interval of $(a, b, \phi_j, \alpha_j, n, m)$ and a user-defined experimental σ-range, we close the groups $\mathcal{G}_{F/Q/L}$ generated by them. Explicitly, it checks the four axioms in nummerations 1-4 in Chapter 4. We consider four cases with different combinations of residual symmetries and their associated generators

$$\begin{aligned}
\mathcal{G}_u \sim Z_n^u,\ \mathcal{G}_d \sim Z_m^d &\quad \rightarrow \quad \mathcal{G}_Q = \{T, S_D\}, \\
\mathcal{G}_u \sim Z_n^u,\ \mathcal{G}_d \sim Z_{m_1}^d \times Z_{m_2}^d &\quad \rightarrow \quad \mathcal{G}_Q = \{T, S_{D_1}, S_{D_2}\}, \\
\mathcal{G}_u \sim Z_{n_1}^u \times Z_{n_2}^u,\ \mathcal{G}_d \sim Z_m^d &\quad \rightarrow \quad \mathcal{G}_Q = \{T_1, T_2, S_D\}, \\
\mathcal{G}_u \sim Z_{n_1}^u \times Z_{n_2}^u,\ \mathcal{G}_d \sim Z_{m_1}^d \times Z_{m_2}^d &\quad \rightarrow \quad \mathcal{G}_Q = \{T_1, T_2, S_{D_1}, S_{D_2}\}.
\end{aligned}$$

6. **Analyze:** After obtaining all groups closed, we apply additional cuts since all groups closed will not be finite, of small-order, non-Abelian, etc. (primary interest for our study). Therefore, we identify the desired symmetry candidates with the *GroupID* and *StructureDescription* commands in GAP, and obtain the parameters $\{a, b, \alpha_j ...\}$ associated to the final group structure. This information on the representations of the residual generators is useful for model-builders to create explicit models.

6.3 Results

We discuss our results for the four different assignments of the residual symmetries $\mathcal{G}_{u/d}$. Our results are presented in tables containing the different groups found when searching within the

[4] Additional parameterizations are [111]

$$\cos(\Theta(c)) = ER\left(1 - \frac{a}{b}\right), \quad \sin(\Theta(c)) = ER\left(\frac{a}{b}\right), \tag{6.2.3}$$

where ER is a square root operation for a rational number N, $\sqrt{N}$. This parameterization is relevant with the discretization scheme $\tan(\Theta_k) = \sqrt{\frac{c}{1-c}}$ with $c = a/b$.

parameter ranges discussed earlier. The first column gives the parameter c, which is directly linked to the Cabibbo angle. Thereafter, the diagonal entries of the 2×2 matrix representations of T_l and S_i are given. After the diagonal entries, the GAP ID of the group closed is given, followed by the associated group structure. In the last column, we display the $\sin\theta_C$ value predicted by the group. The different group structures have specific names associated with them: the (Quasi)-Dihedral groups of order N are $(Q)D_N$ and quaternions of order N are represented as Q_N, and other groups consist of products such as $\Sigma(2N^2) \equiv (Z_N \times Z_{N'}) \rtimes Z_2$. Here, the prime in $Z_{N'}$ means the representations of its generators are different from that of Z_N, however they are both groups of order N. Additionally, we define the following group for simplicity: $\Psi(N, M) \equiv (Z_N \times Z_M) \rtimes Z_2$. In our raw data, the same group shows up multiple times due to reassignments of the generator charges or permutations of the parameter c. It can occur that the same group quantizes the same mixing matrix, but with different diagonal matrix elements in T_l or S_i, or it happens that c is different but predicts the same $\sin(c\pi)$. Therefore, we omit these duplicates from our results.

6.3.1 Case with residual symmetries $G_d \sim Z_m^d$ and $G_u \sim Z_n^u$

We consider the simplest scenario first with a single cyclic symmetry in both the up and down sectors, and we present our results in Tab. 6.1 and Tab. 6.2. In Tab. 6.1, we choose the input parameters as follows: the discretization parameter ranges are $a, b \in \{0, 1...50\}$, and we restrict the order of the residual generators to $\mathcal{O}(T, S) \leq 4$. From this, we obtain 52 values of the parameter c, whereas we have 19 unique diagonal generators for both the up and down sectors. This leads to $19 \cdot 52 = 988$ unique non-diagonal generators S_D, and, in turn, we have $19^2 \cdot 52 = 18772$ different scenarios which could potentially close non-Abelian finite groups. Firstly, we confirm that $\mathcal{O}(S_D \cdot T) < \infty$[5] since we are interested in finite groups. Additionally, we require the order of the parent group to $\mathcal{O}(\mathcal{G}_\mathcal{Q}) \leq 75$ since it is our primarily goal to search for small symmetry groups. Since it is our first simulation, we allow for a rather large range of the Cabibbo angle $0.2 \leq \sin\theta_C \leq 0.3$. We give our results for these "bottom-up" inputs, and many different group structures appear in Tab. 6.1. The groups providing the best prediction of $\sin\theta_C \simeq 0.2225$ ($c = 1/14$) are D_{14}, D_{28} and $Z_7 \rtimes Z_4$. The Dihedral groups D_n and D_{2n} predict the same Cabibbo angle, however, due to our discretization scheme, the order is given by an integer multiple of the denominator of the input parameter c, meaning it is not surprising at all that groups such as D_n nad D_{2n} appear in the same simulation. In addition, other less interesting predictions for $\sin\theta_C$ given by the groups Ψ and Q appear in Tab. 6.1.

There are two Dihedral groups generating two different Cabibbo angles, namely D_{46} (D_{62})

[5] We test all such combinations for other symmetry assignments, where more generators are considered.

quantizes $\sin\theta_C \simeq 0.2698$ (0.2994) and $\sin\theta_C \simeq 0.2035$ (0.2013). Every Dihedral group of order $2n$ predicts n angles, and for the particular cases of $2n = 46$ and $2n = 62$, we have 23 and 31 predictions available, respectively. Due to the Cabibbo angle window $0.2 \leq \sin\theta_C \leq 0.3$, it happens that two of the predictions are within this range.

In our procedure, we obtain Dihedral groups with an order described by the denominator b of the discretization parameter $c = \theta_C/\pi = a/b$. It is easy to understand from a geometrical interpretation. A Dihedral group has a 2×2 element g_{rot} with determinant $\det(g_{rot}) = 1$. In our case, $g_{rot} = TS_D$ since both T and S_D have determinant -1 (see Tab. 6.1), leading to $\det(g_{rot}) = \det(TS_D) = \det(T)\det(S_D) = -1 \cdot -1 = 1$. Using trigonometric identities, one can interpret the element g_{rot} as a rotation, where the angle is given by an integer multiple of $\frac{1}{b}\pi$ of order n; g_{rot}^n is the identity. The Dihedral group D_n has $2n$ elements; half being rotations and the other half being reflections. The n elements (with positive determinant) interpreted as rotations are obtained by taking the powers of g_{rot}. The other half (with negative determinant) are obtained by multiplying the distinct rotations by one of the reflections.

We tighten the Cabibbo angle range to $0.22414 \leq \sin\theta_C \leq 0.22658$ in Tab. 6.2 (closer to the experimental range) while increasing the discretization range $a, b \in \{0, 1...100\}$. Additionally, we restrict $\mathcal{O}(T, S) \leq 3$, but widen $\mathcal{O}(\mathcal{G}_\mathcal{Q}) \leq 1000$ since the ranges of a, b will intuitively generate groups with a larger order. Indeed, we find only larger Dihedral groups with the smallest ones being D_{110} and D_{138}; a total of 8 groups. All groups except D_{110} and D_{220} predict angles within the experimental range, however one can trivially predict ever more precise mixing angles from Dihedral groups by increasing its order and the gridding of a/b (see next paragraph for explanation).

Dihedral groups such as D_{14} and others have been known in the literature for some time [117, 118]. They are trivially generated by our procedure, and the reason is as follow. The mixing matrix Eq. (6.1.7) can be thought of an SO(2) rotation of a circle in the Cabibbo plane, and using our discretization scheme for θ_C corresponds to carving regular polygons out of the circle. Dihedral groups are symmetries of polygons (e.g., D_8 is the symmetry of a square), so it is no surprise that we find them in our procedure. Additionally, making a finer gridding generates large ordered groups, meaning the number of sides of the associated polygons increases. This justifies our requirement $\mathcal{O}(\mathcal{G}_\mathcal{F}) \lesssim 75$ introduced earlier since a Dihedral group will always be able to trivially predict a mixing angle in a given range (as seen in Tab. 6.2), if the order is high enough. Additionally, no Dihedral groups were found in more universal, top-down scans like that in Ref. [116] because most such studies insist that $\mathcal{G}_\mathcal{Q}$ contain 3-dimensional representations — polygons are, after all, 2 dimensional objects.

Given the results in Tab. 6.1 and Tab. 6.2, one can reconstruct the generator representations

to build a flavor model. As an example, we consider line 13 of Tab. 6.1, obtaining

$$U_{\rm CKM}^{LO} \simeq \begin{pmatrix} 0.9749 & 0.2225 \\ -0.2225 & 0.9749 \end{pmatrix} \tag{6.3.1}$$

from the non-Abelian finite group $Z_7 \rtimes Z_4$. It is generated by the matrix representations

$$T^{Z_7\rtimes Z_4} = \begin{pmatrix} -i & 0 \\ 0 & i \end{pmatrix} \quad \text{and} \quad S_D^{Z_7\rtimes Z_4} = \begin{pmatrix} -i\cos\frac{2\pi}{14} & i\sin\frac{2\pi}{14} \\ i\sin\frac{2\pi}{14} & i\sin\frac{2\pi}{14} \end{pmatrix}, \tag{6.3.2}$$

where we use some trigonometric identities.

As a final note, one can question the diversity of the group structures[6] in Tab. 6.1 and Tab. 6.2. A well-known example is the alternating symmetry of the tetrahedron A_4, which predicts unit (*i.e.* trivial) mixing in the quark sector [83–87]. This is a reasonable first-order approximation, however this prediction is impossible with our approach. Unit mixing translates to a diagonal down-sector generator, which commutes with the diagonal up-sector generator — it will never close an non-Abelian finite group. Another example is the symmetry group of the triangle S_3. We do not find it, however it can be generated by two matrices with the forms of Eq. (6.1.4) and Eq. (6.1.5). Its absence is due to the range of the Cabibbo angle — S_3 predicts $\sin\theta_C = 0.7071$, a much larger value than 0.3. In Appendix A, we investigate other mixing angles (not associated with the Cabibbo angle) using our method, and we show that many other group structures can be found.

6.3.2 Case with residual symmetries $G_d \sim Z_{m1}^d \times Z_{m2}^d$ and $G_u \sim Z_n^u$

In this section, we study the symmetry assignment $G_d \sim Z_{m1}^d \times Z_{m2}^d$ in the down sector while keeping a single cyclic group $G_u \sim Z_n^u$ in the up sector. We consider $a, b \in \{0, 1...50\}$, $\mathcal{O}(T, S_1, S_2) \leq 4$, and $\mathcal{O}(\mathcal{G}_\mathcal{Q}) \leq 75$, but restrict the Cabibbo window to $0.2 \leq \sin\theta_C \leq 0.24$ to obtain predictions closer to the experimental value. We follow the same procedure as before, however now with two generators in the down sector. The results are presented in Tab. 6.3, however we find only one new group $Z_3 \times D_{14}$ in comparison to Tab. 6.1. It also predicts $\sin\theta_C \simeq 0.2225$. The result is highlighted in blue together with an arrow pointing at the group structure. The eigenvalues of S_{i1} are clearly degenerate, meaning one cannot distinguish the two generations[7]. From the model-building perspective, this group do not more work than D_{14}.

[6] In both Tab. 6.1 and Tab. 6.2, we consider the same maximum value of the order of the generators T and S. However, more interesting structures might have subgroups with different maximum order. Therefore, we perform a scan with $\mathcal{O}(T) \leq 6$, but $\mathcal{O}(S) \leq 4$. We put $a, b \in \{0, 1...50\}$, $0.2 \leq \sin\theta_C \leq 0.24$, and restrict $(\mathcal{G}_\mathcal{Q}) \leq 75$. With these inputs, we find no new group structures.

[7] We have otherwise filtered results where generators carry degenerate eigenvalues since every group could have been generated by these redundant matrices.

c	T_{diag}	S_i	GAP-ID	Group Structure	$\sin\theta_C$
$\frac{1}{11}$	[-1, 1]	[-1, 1]	[22, 1]	D_{22}	0.2817
$\frac{1}{11}$	[1, -1]	[-1, 1]	[44, 3]	D_{44}	0.2817
$\frac{1}{11}$	[-i, i]	[-i, i]	[44, 1]	$Z_{11} \rtimes Z_4$	0.2817
$\frac{1}{12}$	[-1, 1]	[-1, 1]	[24, 6]	D_{24}	0.2588
$\frac{1}{12}$	[-i, i]	[-1, 1]	[24, 8]	$\Psi(6,2)$	0.2588
$\frac{1}{12}$	[-i, i]	[-i, i]	[24, 4]	$Z_3 \rtimes Q_8$	0.2588
$\frac{1}{13}$	[-1, 1]	[-1, 1]	[26, 1]	D_{26}	0.2393
$\frac{1}{13}$	[1, -1]	[-1, 1]	[52, 4]	D_{52}	0.2393
$\frac{1}{13}$	[-i, i]	[-i, i]	[52, 1]	$Z_{13} \rtimes Z_4$	0.2393
$\frac{1}{14}$	[-1, 1]	[-1, 1]	[28, 3]	D_{28}	0.2225
$\frac{1}{14}$	[-i, i]	[-1, 1]	[56, 4]	$Z_4 \times D_{14}$	0.2225
$\frac{1}{14}$	[1, -1]	[-1, 1]	[14, 1]	D_{14}	0.2225
$\frac{1}{14}$	[-i, i]	[-i, i]	[28, 1]	$Z_7 \rtimes Z_4$	0.2225
$\frac{1}{15}$	[-1, 1]	[-1, 1]	[30, 3]	D_{30}	0.2079
$\frac{1}{15}$	[1, -1]	[-1, 1]	[60, 12]	D_{60}	0.2079
$\frac{1}{15}$	[-i, i]	[-i, i]	[60, 3]	$Z_{15} \rtimes Z_4$	0.2079
$\frac{2}{21}$	[-1, 1]	[-1, 1]	[42, 5]	D_{42}	0.2948
$\frac{2}{23}$	[-1, 1]	[-1, 1]	[46, 1]	D_{46}	0.2698
$\frac{2}{25}$	[-1, 1]	[-1, 1]	[50, 1]	D_{50}	0.2487
$\frac{2}{27}$	[-1, 1]	[-1, 1]	[54, 1]	D_{54}	0.2306
$\frac{2}{29}$	[-1, 1]	[-1, 1]	[58, 1]	D_{58}	0.2150
$\frac{2}{31}$	[-1, 1]	[-1, 1]	[62, 1]	D_{62}	0.2013
$\frac{3}{31}$	[-1, 1]	[-1, 1]	[62, 1]	D_{62}	0.2994
$\frac{3}{32}$	[-1, 1]	[-1, 1]	[64, 52]	D_{64}	0.2903
$\frac{3}{32}$	[-i, i]	[-1, 1]	[64, 53]	QD_{64}	0.2903
$\frac{3}{32}$	[-i, i]	[-i, i]	[64, 54]	Q_{64}	0.2903
$\frac{3}{34}$	[-1, 1]	[-1, 1]	[68, 4]	D_{68}	0.2737
$\frac{3}{34}$	[1, -1]	[-1, 1]	[34, 1]	D_{34}	0.2737
$\frac{3}{34}$	[-i, i]	[-i, i]	[68, 1]	$Z_{17} \rtimes Z_4$	0.2737
$\frac{3}{35}$	[-1, 1]	[-1, 1]	[70, 3]	D_{70}	0.2660
$\frac{3}{37}$	[-1, 1]	[-1, 1]	[74, 1]	D_{74}	0.2520
$\frac{3}{38}$	[1, -1]	[-1, 1]	[38, 1]	D_{38}	0.2455
$\frac{3}{46}$	[1, -1]	[-1, 1]	[46, 1]	D_{46}	0.2035

Table 6.1: Flavor symmetries of U_{CKM}^{LO} using the charge assignment $\mathcal{G}_d \sim Z_m$, $\mathcal{G}_u \sim Z_n$ with $m, n < 5$ and $\mathcal{O}(\mathcal{G}_\mathcal{Q}) \leq 75$. We display outcomes with distinct groups and $\sin\theta_C$ (duplicates with different T and S generators from the ones shown, but same group and same physical angle are omitted). Table taken from Ref. [180].

c	T_{diag}	S_i	GAP-ID	Group Structure	$\sin\theta_C$
$\frac{4}{55}$	[-1, 1]	[-1, 1]	[110, 5]	D_{110}	0.2265
$\frac{4}{55}$	[1, -1]	[-1, 1]	[220, 14]	D_{220}	0.2265
$\frac{5}{69}$	[-1, 1]	[-1, 1]	[138, 3]	D_{138}	0.2257
$\frac{5}{69}$	[1, -1]	[-1, 1]	[276, 9]	D_{276}	0.2257
$\frac{6}{83}$	[-1, 1]	[-1, 1]	[166, 1]	D_{166}	0.2252
$\frac{6}{83}$	[1, -1]	[-1, 1]	[332, 3]	D_{332}	0.2252
$\frac{7}{97}$	[-1, 1]	[-1, 1]	[194, 1]	D_{194}	0.2248
$\frac{7}{97}$	[1, -1]	[-1, 1]	[388, 4]	D_{388}	0.2248

Table 6.2: Flavor symmetries of U^{LO}_{CKM} using charge assignment $\mathcal{G}_d \sim Z_m$, $\mathcal{G}_u \sim Z_n$ with $m, n \leq 3$ and $\mathcal{O}(\mathcal{G}_\mathcal{Q}) \leq 1000$. We display only outcomes with distinct groups and $\sin\theta_C$ (duplicates are omitted). Table taken from Ref. [180].

Therefore, this group is not an interesting result.

No new quantizations of $\sin\theta_C$ are found using similar (or contained within) parameter ranges as those used for Tab. 6.1. Additionally, we are not concerned that, for example, D_{28} is "generated" by three matrices since other Dihedral groups are closed by two generators only. After all, a finite group $\mathcal{G}_\mathcal{F}$ can be "generated" by all of its elements! However, the *smallest* set of elements generating the Dihedral group is 2. Indeed, three elements are returned

$$\text{GeneratorsOfGroup}(\text{SmallGroup}(28,3)) = [f_1, f_2, f_3] \tag{6.3.3}$$

when asking GAP for the generators f_i of SmallGroup$(28,3)$ corresponding to D_{28}. However, we can also ask GAP for the smallest subset of these three "generators" that will do the same job

$$\text{MinimalGeneratingSet}(\text{SmallGroup}(28,3)) = [f_1, f_2 \cdot f_3]\,. \tag{6.3.4}$$

Similarly but in reverse order, one would normally assign three generators to the group $\Psi(6,2)$ in Tab. 6.1 to better reveal its structure in terms of the three cyclic symmetries $((Z_6 \times Z_2) \rtimes Z_2)$, however it can be generated by two only. An other example is $\Delta(27) = ((Z_3 \times Z_3) \rtimes Z_3) \in \Delta(3N^2)$, a popular group for model-building in the leptonic sector [181–183].

6.3.3 Additional findings

Changing the symmetry assignment to $G_d \sim Z^d_m$ and $G_u \sim Z^u_{n1} \times Z^u_{n2}$, gives similar results as the case $G_d \sim Z^d_{m1} \times Z^d_{m2}$ and $G_u \sim Z^u_n$ since physical observables are basis-independent. Additionally, we investigate the symmetry assignment $G_d \sim Z^d_{m1} \times Z^d_{m2}$ and $G_u \sim Z^u_{n1} \times Z^u_{n2}$. More groups are closed due to the larger number of generators, however we obtain the

c	T_{diag}	S_{i1}	S_{i2}	GAP-ID	Group Structure	$\sin\theta_C$
$\frac{1}{13}$	[-1, 1]	[-1, 1]	[1, -1]	[52, 4]	D_{52}	0.2393
$\frac{1}{13}$	[-i, i]	[-i, i]	[i, -i]	[52, 1]	$Z_{13} \rtimes Z_4$	0.2393
$\frac{1}{14}$	[-1, 1]	[-1, 1]	[1, -1]	[28, 3]	D_{28}	0.2225
$\frac{1}{14}$	[-1, 1]	[-1, 1]	[-i, i]	[56, 4]	$Z_4 \times D_{14}$	0.2225
$\frac{1}{14}$	[-i, i]	[-i, i]	[i, -i]	[28, 1]	$Z_7 \rtimes Z_4$	0.2225
$\frac{1}{14}$	[1, -1]	[E(3)^2, E(3)^2]	[-1, 1]	[42, 4]	$\rightarrow Z_3 \times D_{14}$	0.2225
$\frac{1}{15}$	[-1, 1]	[-1, 1]	[1, -1]	[60, 12]	D_{60}	0.2079
$\frac{1}{15}$	[-i, i]	[-i, i]	[i, -i]	[60, 3]	$Z_{15} \rtimes Z_4$	0.2079

Table 6.3: Flavor symmetries of U^{LO}_{CKM} using charge assignment $\mathcal{G}_d \sim Z_{m_1} \times Z_{m_2}$, $\mathcal{G}_u \sim Z_n$ with $m, n < 5$, $\mathcal{O}(T, S) < 5$ and $\mathcal{O}(\mathcal{G}_\mathcal{Q}) \leq 75$. We display outcomes with distinct groups and $\sin\theta_C$ (duplicates are omitted). Table taken from Ref. [180].

same results as in the previous two subsections. Within the parameter ranges, the additional generators does nothing for us. Therefore, we omit both findings here.

The procedure is ignorant about the physical meaning of the generators, *i.e.* the symmetry of the Lagrangian. Hence, from a completely agnostic perspective, the bottom-up approach could study the consequence of a simple rewriting of the mixing matrix, *i.e.*one expands about the Cabibbo angle $\sin^2\theta_C \approx \lambda^2 + \mathcal{O}(\lambda^3)$ and $\cos^2\theta_C \approx (\lambda^2/2 - 1)^2 + \mathcal{O}(\lambda^3)$ with $\lambda = 0.225$. It only changes the numerical values by a small amount, meaning it is plausible that it generates different parent groups $\mathcal{G}_Q$. One might interpret it as a "broken-symmetry". However, as a result of the expansion, the mixing matrix is only unitary up to $\mathcal{O}(\lambda^4)$, resulting in the order of the associated generator is infinite. Hence, the generator will never close a group, meaning it does not generate a symmetry of the Lagrangian. Indeed, upon running our script, we find no closed flavor groups (at least not for our computational input).

6.4 General discussion and limitations

The bottom-up technique is a powerful tool to identify symmetry groups useful for model-building, however it is important to discuss its limitations. Only direct or semi-direct models can be constructed from the matrix representations of the generators using the method since it either predicts all angles in the mixing matrix or a column of the mixing matrix. Indirect models *cannot* be constructed since the residual symmetries are not subgroups of the actual flavor symmetry.

A number of user-defined parameters serves as input in the procedure, including the ranges of a/b (related to the discretization of the phases and θ_C), the allowed range of the Cabibbo angle $\sin\theta_C$, the maximum order of the residual symmetries $\mathcal{G}_{u/d}$, and the maximum order of

the parent symmetry $\mathcal{G}_\mathcal{F}$. Widening or increasing any of these parameters produces more group closures, and Fig. 6.1 shows a qualitative illustration of the growth of group closures. In each subfigure[8], we vary one of the four "tunes" independently while fixing the others to a specified value.

There is roughly a linear increase in group closures when increasing $a_{\max}$ (upper limit on a, and thereby b, giving a finer gridding of θ_C) or the range of the Cabibbo angle $\sin\theta_C$ (see Fig. 6.1A and Fig. 6.1B, respectively). In Fig. 6.1D, the closures eventually plateaus for an increasing order of the parent symmetry, and this feature is sensible; a finite number of constraints will limit the group closures. Increasing $a_{\max}$ to 35 in Fig. 6.1D, the plateau would occur at 120 groups for $\text{MaxOrder}(\mathcal{G}_\mathcal{F}) \geq 170$.

Seen in Fig. 6.1C, a plateau also appears, however it is an artifact of our constraint on $\sin\theta_C$. This is verified by studying the table in Appendix A, where un-physical Cabibbo angle predictions appear together with generators of order 3. Therefore, widening the allowed Cabibbo angle range, increases the number of group closes between $\mathcal{O}(T,S) \leq 2$ and $\mathcal{O}(T,S) \leq 3$, meaning the plateau would disappear. We confirm this by running two additional scans, where the effective number of c's are reduced to four and one (there are 10 active c's in Fig. 6.1C). For both cases, plateaus begin at $\mathcal{O}(T,S) \leq 2$ and $\mathcal{O}(T,S) \leq 4$. Additionally, for the single-c scan, the final plateau remains up to $\mathcal{O}(T,S) \leq 8$ (we only ran up to $\mathcal{O}(T,S) \leq 7$ for the four-c scan). From this, we deduce that plateaus appear at $4^1 \times (\#\ of\ c's)$ and $4^2 \times (\#\ of\ c's)$, meaning there are plateaus at 4 and 16 group closures for one active c, 16 and 64 group closures for four active c's, and 40 and 160 group closures for 10 active c's. We checked that there are more closures of *Abelian* groups as $\mathcal{O}(T,S)$ increases, however no additional non-Abelian group closes (primary goal of our study).

Not necessarily associated to the bottom-up technique, an other difficulty arises when the angles considered are very small. Increasing the group order, means a more precise Cabibbo angle prediction. This is given in Tab. 6.2, showing the correlation between group order and associated mixing angle. This is clear to understand for Dihedral groups due to the geometric interpretation in terms of polygons. Small c parameters means small mixing angles, and from this, we can infer that we need Dihedral groups with $\text{Order}(\mathcal{G}_\mathcal{F}) \gtrsim \mathcal{O}(1000)$ to quantize the smallest quark mixing angle, $\theta^q_{13} \approx \pi/900$. This acts as a lower bound on the order of the group necessary to quantize the full CKM matrix. We perform a dedicated "bottom-up" scan to search for discrete symmetries capable to quantize the full CKM matrix, yet non were found. We considered a computation time of a few days when performing this dedicated scan. This result is consistent with previous studies, and our approach should also be able to find it, as long as a finite group has an order smaller than $\mathcal{O}(1000)$.

[8] We use the symmetry assignment in Section 6.3.1

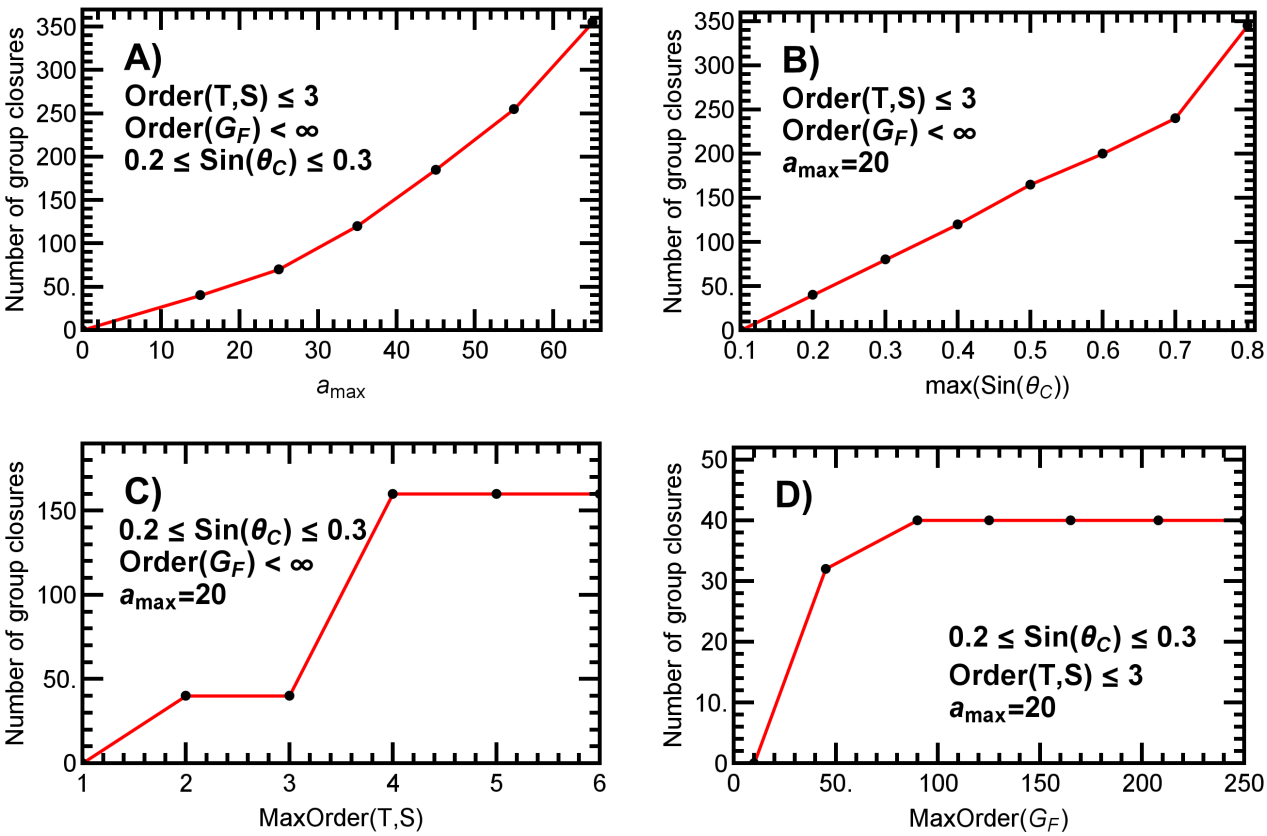

Figure 6.1: Figures showing the number of parent group closures $\mathcal{G}_\mathcal{F}$ found when varying four inputs in the "bottom-up" method, namely the discretization parameters a and b (A), the allowed quantization range of $\sin\theta_C$ (B), the maximum order of the residual Abelian symmetry groups $\mathcal{O}(\mathcal{G}_u, \mathcal{G}_d)$ (C), and the maximum allowed of the parent non-Abelian symmetry group $\mathcal{O}(\mathcal{G}_\mathcal{F})$ (D). In each case, we fix the 3 other inputs to the values shown in the figures. We display our raw data, meaning we include duplicates in these figures. The curves represent first-order interpolations of the data, and are present as a visual aid only — they do not represent any theory. Figure taken from Ref. [180].

Chapter 7

Symmetric or anarchical approach to thermal leptogenesis

In the two previous chapters, we considered the possibility of flavor symmetries as origin of the fermion mixing parameters. Beside this, one can also consider the generation of a baryon asymmetry in the same context. In this chapter, we discuss the generation of a baryon asymmetry, where sterile neutrinos with masses of 10^{12} GeV are introduced. We use the same texture sets introduced in Section 5.3. Additionally, we consider the anarchy hypothesis, making a comparison between the two frameworks. As a result, different sterile mass distributions are predicted, meaning there is a clear difference between the two frameworks.

7.1 Thermal leptogenesis

There are many possibilities to generate a baryon asymmetry, depending on the nature of baryon/lepton number non-conservation, CP-violation and departure from thermal equilibrium. We discussed an example involving GeV sterile neutrinos in the context of the νMSM introduced in Section 4.5, however the sterile neutrinos can also be heavier than the Fermi scale. An example is thermal leptogenesis [184], which requires sterile neutrinos with mass of 10^{12} GeV. A resonant variant with degenerate TeV sterile neutrinos is also possible, meaning it is testable at the LHC compared to the original non-resonant leptogenesis version (we discuss this difference later).

It is possible to generate a lepton asymmetry from heavy neutrino decay due to an interference among the tree-level diagram and one-loop diagrams (shown in Fig. 7.1), which gets converted to a baryon asymmetry via the sphaleron processes. To leading order, the lepton asymmetry is [186]

$$\begin{aligned}\epsilon_{i\alpha} = &\frac{1}{8\pi}\frac{1}{(Y^\dagger Y)_{ii}}\sum_{j\neq i}\mathrm{Im}[(Y^\dagger Y)_{ij}Y_{\alpha i}Y^*_{\alpha j}]g\left(\frac{M_j^2}{M_i^2}\right)\\ &+\frac{1}{8\pi}\frac{1}{(Y^\dagger Y)_{ii}}\sum_{j\neq i}\mathrm{Im}[(Y^\dagger Y)_{ji}Y_{\alpha i}Y^*_{\alpha j}]\frac{M_i^2}{M_i^2-M_j^2}\,,\end{aligned} \tag{7.1.1}$$

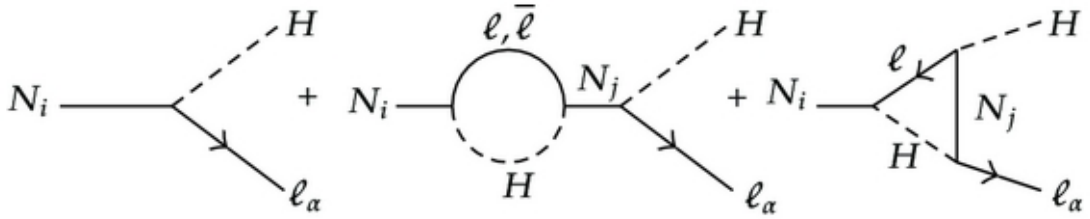

Figure 7.1: Tree level and one-loop diagrams contributing to heavy neutrino decay whose inferences leads to a lepton asymmetry. Figure taken from Ref. [185]

where $Y_{\alpha i}$ is the neutrino Yukawa matrix, M_i is the sterile neutrino mass, and the loop function reads

$$g(x) = \sqrt{x}\left[\frac{1}{1-x} + 1 - (1+x)\ln\left(\frac{1+x}{x}\right)\right]. \tag{7.1.2}$$

The second term in Eq. (7.1.1) dominates the production of the asymmetry if $M_i \approx M_j$ (resonant leptogenesis), meaning one can shift the masses to a lower mass scale (usually TeV scale), but it requires a mass degeneracy of 10^{-9} between two sterile neutrinos. This can be compared to the original idea of thermal leptogenesis, where the asymmetry is generated by the first term in Eq. (7.1.1), which requires masses of 10^{12} GeV with an arbitrary mass degeneracy. In general, there are three different regimes where the washout of the asymmetry is either strong, average or weak. To quantify this, we define the decay parameter [187]

$$K_i = \frac{\tilde{m}_i}{m_*}, \tag{7.1.3}$$

where $\tilde{m}_i$ is the effective neutrino mass defined as

$$\tilde{m}_i = \frac{(Y^\dagger Y)_{ii} v^2}{M_i} \tag{7.1.4}$$

with $m_* \equiv \frac{16\pi^2 v^2}{3M_{\text{Planck}}}\sqrt{\frac{g_*\pi}{5}} \simeq 10^{-3}$ eV. The regimes are given by $K_i \ll 1$ (weak washout), $K_i \approx 1$ (intermediate washout) and $K_i \gg 1$ (strong washout). The baryon asymmetry is expressed with respect to the entropy [188]

$$\frac{n_{\mathcal{B}}}{s} = \frac{24 + 4n_H}{66 + 13n_H}\frac{n_{\mathcal{B}-\mathcal{L}}}{s}, \tag{7.1.5}$$

where n_H is the number of Higgs doublets ($n_H = 1$ for SM), and the factor in-front is the

sphaleron conversion factor [189, 190]. It is related to the lepton asymmetry via [188]

$$\frac{n_{\mathcal{B}-\mathcal{L}}}{s} = Y^{\rm eq} \sum_i \epsilon_i \eta_i(\tilde{m}_i)\,, \tag{7.1.6}$$

where $\epsilon_i \equiv \sum_\alpha \epsilon_{i\alpha}$ is the asymmetry parameter in the sterile neutrino decay, η is the efficiency factor of the asymmetry washout, $Y^{\rm eq} = 135\zeta(3)/(4\pi^4 g_*)$, g_* counts the effective number of spin-degrees of freedom in thermal equilibrium ($g_* = 106.75$ in SM at temperatures larger than the electroweak phase transition), and $\zeta(3) \simeq 1.202$. The measurement of the baryon asymmetry is given by [131–133]

$$\frac{n_b - n_{\bar{b}}}{n_\gamma} = \eta_B = (6.10 \pm 0.04) \times 10^{-10}\,, \quad \frac{n_b - n_{\bar{b}}}{s} = (0.87 \pm 0.01) \times 10^{-10}\,, \tag{7.1.7}$$

with respect to the photon density and the entropy, respectively, where the conversion factor is $s = 7.04 n_\gamma$ between the two expressions. The generation of the baryon asymmetry occurs as the temperature of the expanding Universe decreases. As a consequence, flavor effects become important since the charged lepton Yukawa couplings equilibrate, meaning we must study this effect next.

7.1.1 Flavor effects

It is possible to study leptogenesis in three separate regions, namely the one-, two- and three-flavor regimes [191] (not to be confused with the washout regimes). One can estimate the specific temperature when flavor effects become important by requiring the flavored decay rate Γ_α ($\alpha = e, \mu, \tau$) being faster than the Universe expansion rate $H(T)$, *i.e.* $\Gamma_\alpha(T) > H(T)$ when $T < T_\alpha$, where $\Gamma_\alpha(T) \simeq 10^{-2} h_\alpha^2 T$ [192], $H(T) = 2/3\sqrt{g_*\pi^3/5}T^2/M_{\rm Planck}$, $M_{\rm Planck} = 1.22 \cdot 10^{19}$ GeV is the Planck mass, and h_α is the flavored charged lepton Yukawa coupling. We obtain the temperatures $T_e \simeq 4 \cdot 10^4$ GeV, $T_\mu \simeq 2 \cdot 10^9$ GeV and $T_\tau \simeq 5 \cdot 10^{11}$ GeV which defines the boundary of the three different regions. Notice that to fully distinguish the three flavors, it is sufficient that the τ and μ Yukawa reactions attain thermal equilibrium. For the one-flavor regime, *i.e.* sterile neutrino mass is larger than T_τ, one uses Eqs. (7.1.5)-(7.1.6) to obtain the baryon asymmetry (remember conversion factor). In the case of the two-flavor regime, the baryon asymmetry becomes [191]

$$\frac{n_{\mathcal{B}}}{s} \simeq \frac{24 + 4n_H}{66 + 13n_H} Y^{\rm eq} \left(\epsilon_{oi}\eta \left(\frac{417}{589}\tilde{m}_{oi} \right) + \epsilon_{\tau i}\eta \left(\frac{390}{589}\tilde{m}_{\tau i} \right) \right) \tag{7.1.8}$$

with $\epsilon_{oi} = \epsilon_{ei} + \epsilon_{\mu i}$, $\tilde{m}_{oi} = \tilde{m}_{ei} + \tilde{m}_{\mu i}$, and $\tilde{m}_{\alpha i} = v^2 Y_{i\alpha} Y_{i\alpha}^\dagger / M_i$. At $T < 10^9$ GeV, the baryon asymmetry is [191]

$$\frac{n_{\mathcal{B}}}{s} \simeq \frac{24 + 4n_H}{66 + 13n_H} Y^{\rm eq} \left(\epsilon_{ei} \eta \left(\frac{151}{179} \tilde{m}_{ei} \right) + \epsilon_{\mu i} \eta \left(\frac{344}{537} \tilde{m}_{\mu i} \right) + \epsilon_{\tau i} \eta \left(\frac{344}{537} \tilde{m}_{\tau i} \right) \right) . \tag{7.1.9}$$

7.1.2 General remarks in the context of thermal leptogenesis

There are many aspects in this subject, however we consider the following question for discussion:

- How many sterile neutrinos contribute to the baryon asymmetry, and what are their masses?

Before discussing it, we describe the time period prior to the baryon asymmetry time period since it has an important impact on the generation of the baryon asymmetry. In the beginning of the Universe, reheating occurs, and without it, inflation would leave the Universe empty of matter. Reheating happens through coupling of the inflation field ϕ, the scalar field generating the accelerated expansion of space, to SM matter, and the associated temperature is usually defined as the temperature of the plasma assuming an instantaneous conversion of the inflaton's energy density into radiation. It is given by $T_{\rm rh} = \left(\frac{90}{8\pi^3 g_*}\right)^{1/4} \sqrt{\Gamma_\phi M_{\rm Planck}}$ [193, 194] at time $H(T) \approx \Gamma_\phi$, where $H(T)$ is the Hubble rate, and Γ_ϕ is the decay rate of the inflaton ϕ. The decay rate of the inflaton is rather unknown, so the reheating temperature can vary in the interval $T_{\rm rh} \in [10^6, 10^{16}]$ GeV [194].

With this information, we discuss the question given above. This is a rather general question since there are many different answers, depending on the specific model in mind. The masses are not constrained in the seesaw mechanism, and due to a scaling symmetry, one can shift the masses without changing the neutrino oscillation parameters. However, it relates to the reheating temperature since the production of sterile neutrinos with mass M_i larger than $T_{\rm rh}$ are suppressed, whereas they are thermally produced for $M_i < T_{\rm rh}$. Due to the range of $T_{\rm rh}$, a rather large mass window is allowed. In addition, $T_{\rm rh}$ can control the number of sterile neutrinos contributing to the baryon asymmetry. Setting $M_{2,3} > T_{\rm rh}$ but $M_1 < T_{\rm rh}$, means the lightest sterile neutrino contribute to the baryon asymmetry only since the production of the two heavier sterile neutrinos is negligible. This is the most common case studied in the literature. However, there are counterexamples such as the second heaviest sterile neutrino dominating the asymmetry production or all three contributing to the baryon asymmetry [195–198].

We consider the scenario with the lightest sterile neutrino generating the baryon asymmetry only. Additionally, we investigate all three flavor regimes. This means one has to replace all indices i with 1 in the previous discussion. We use numerical fits for the washout efficiency η

instead of solving Boltzmann equations as the method to compute the baryon asymmetry since a similar study [199] found an agreement of seven percent between solving the Boltzmann equations and using the numerical fits of the washout efficiency factor in obtaining the baryon asymmetry. Therefore, this is only a conservative estimation of the baryon asymmetry. The efficiency factor η, that takes into account the washout effect of the total lepton charge asymmetry produced by the out-of-equilibrium decays, is parameterized as [188]

$$\eta(X) \simeq \left(\frac{3.3 \cdot 10^{-3}\text{eV}}{X} + \left(\frac{X}{0.55 \cdot 10^{-3}\text{eV}} \right)^{1.16} \right)^{-1} \tag{7.1.10}$$

for the one-flavor regime. In the flavored scenario, such efficiency factors are approximated by the expression [191]

$$\eta(X) \simeq \left(\frac{8.25 \cdot 10^{-3}\text{eV}}{X} + \left(\frac{X}{2 \cdot 10^{-4}\text{eV}} \right)^{1.16} \right)^{-1} . \tag{7.1.11}$$

7.2 Method

Given the discussion about thermal leptogenesis and flavor effects, we take the same texture sets given in Tab. 5.1, and compute their predictions for the baryon asymmetry. It was not the original idea of Ref. [80] for the texture sets to generate a viable baryon asymmetry, meaning we are entering new territories when computing the baryon asymmetry for the texture sets. We use the same method given in Section 5.2, obtaining viable neutrino oscillation parameters via the minimization of the χ^2, but we have to change the Dirac and Majorana mass matrix scales to generate GUT-scaled sterile neutrino masses. However, considering the scaling symmetry

$$M_R \to z M_R \,, \quad Y_{\alpha i} \to \sqrt{z} Y_{\alpha i} \,, \quad \eta_B \to z \eta_B \tag{7.2.1}$$

with z being a real number, one can obtain a baryon asymmetry within its experimental limit. As a result, a mass distribution is obtained for the different texture sets, and a comparison can be made. If the sterile neutrino mass is larger than 10^{16} GeV (upper bound on the reheating temperature), one can exclude whether the texture sets can generate a baryon asymmetry since its production is suppressed.

Beside considering the texture sets, one can also consider the anarchy hypothesis as the origin of the entry values in the matrices. We draw matrix entries from a Gaussian distribution with mean zero and variance one, and compute the baryon asymmetry for the anarchy hypothesis. Again, we use the scaling symmetry to obey the experimental baryon asymmetry limit, and study this impact on the sterile neutrino mass distribution. We dub this scenario the **anarchy** case.

Beside this scenario, we study two additional cases using the Wishart method with $N = 4$ and $N = 30$. Again, we choose a Gaussian distribution with zero mean and variance one to generate the matrix elements of F and G. We choose $M_0 \sim 10^6 - 10^{16}$ GeV and $m_D \sim 10^3 - 10^8$ GeV to generate masses in the interval of interest. To obtain the Dirac and Majorana mass matrices, we use Eq. (4.4.2), and thereafter we compute the baryon asymmetry. We can make use of the scaling symmetry again if the baryon asymmetry is outside of its experimental limit. We dub these two new cases **Wishart N=4** and **Wishart N=30**, respectively, and compare the distribution of the lightest sterile neutrino mass to the other cases.

7.3 Results

We present our findings of the lightest sterile neutrino mass distribution shown in Fig. 7.2 for both symmetry and anarchy cases, and the black dashed lines indicates the transition between the three different flavor regimes. The mass range goes from 10^6 GeV to 10^{16} GeV, the lower and upper bound of the reheating temperature. For the flavor symmetry cases, a broad distribution is obtained for all texture sets, meaning a large overlap among the different distributions, even though they are peaking at different mass values. Texture 22 tends to favor the two flavor regime, having roughly 2/3 of its area in this region. In contrary, texture 19 favors the one flavor regime, whereas the distribution for texture 15 is between the two other distributions. Additionally, the distributions are not occupying the three flavor regime much. However, this is due to the mass degeneracy needed to generate a successful baryon asymmetry. For the anarchy cases, they have nearly the same distribution, *i.e.* same width and sterile neutrino mass peak value. The measure of the mass eigenvalues might dictate the mass distribution shape for the anarchy cases, giving a possible explanation of their similar shape. They tend to have the largest overlap with the one flavor regime, whereas it is more sparse with predictions in the other flavor regimes. Comparing the anarchy cases with the flavor symmetry cases, one sees a clear difference in width for the distributions. This means the flavor symmetry cases can generate a baryon asymmetry at lower masses compared to the anarchy cases, even though the Wishart anarchy method can generate degenerate sterile neutrinos for large N. Therefore, one should expect its distribution occupying the three flavor regime. A dedicated scan for the Wishart method with large N shows realizations in the three flavor regime are possible, even though rare due to the fine-tuning of the mass degeneracy needed to generate the correct amount of baryon asymmetry and keeping the lightest sterile neutrino mass below 10^8 GeV. We do not exclude the degenerate mass cases for both flavor symmetric and anarchical mass models, however these cases are mor rare and need special attention to construct such models. Additionally, for both the flavor symmetry cases and the anarchy cases, we study the correlation among the CP-violating phases and the baryon

asymmetry. No direct correlations were found, but the whole parameter space was occupied.

7.4 Outlook

In this study, we consider GUT-scaled sterile neutrinos, which are not within experimental reach in the near future. However, it is already possible to test its resonant version with degenerate TeV sterile neutrinos at the LHC. Mentioned earlier, GeV sterile neutrinos can also generate the baryon asymmetry, and they are within experimental reach by several future experiments. Therefore, one could test whether the texture sets or the anarchy hypothesis can generate the right amount of baryon asymmetry with GeV sterile neutrinos. There are model-independent studies with three GeV sterile neutrinos in the literature[135, 200], and the allowed parameter space coincide with our model parameter space given in Chapter 5. Therefore, in principle, it is possible to generate the baryon asymmetry using the texture sets considered earlier, however a full calculation is needed to clearly settle this argument. One cannot necessary use the same approach as in this chapter since it relies on computations for thermal leptogenesis. Considering the anarchy hypothesis, one can incorporate thermal leptogenesis into this framework [81, 201]. However, no one has considered GeV sterile neutrinos as the origin of the baryon asymmetry in the anarchy hypothesis. The Haar measure sets strong limits on the matrix entries, meaning one might not be able to generate the baryon asymmetry with GeV sterile neutrinos in the anarchy hypothesis. This could be another analysis worth pursuing in the future.

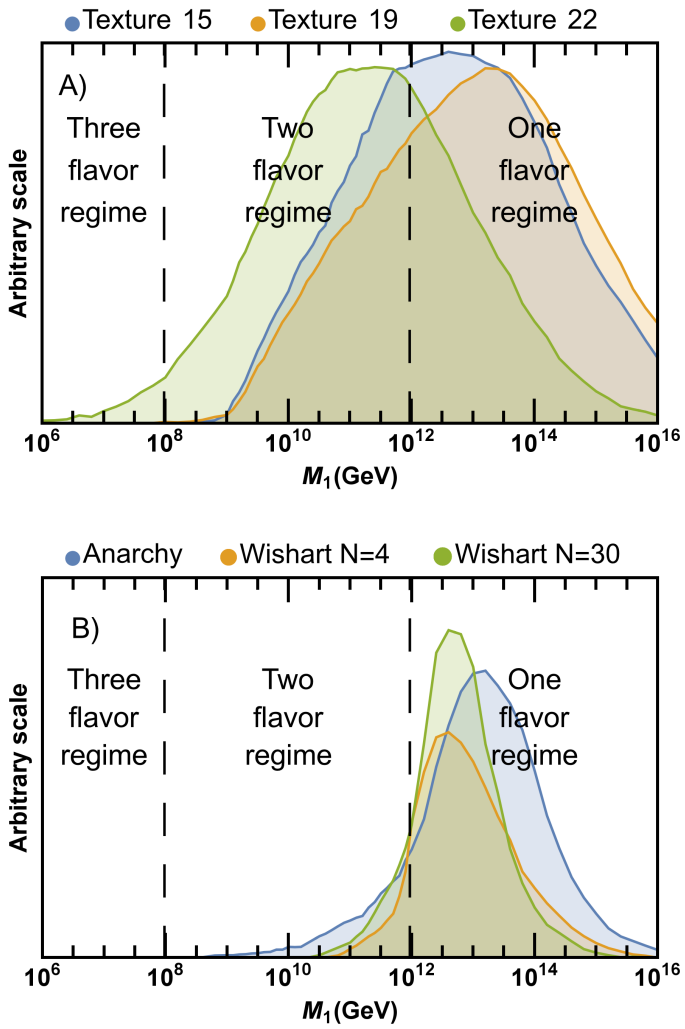

Figure 7.2: Mass distribution for successful baryon asymmetry generation. The three different flavor regions are separated by dashed black lines, while the coloring is displayed in the figure legend. (A) Mass distributions for the texture sets in Tab. 5.1. (B) Mass distributions for the anarchy cases.

Chapter 8

Anarchy with eV sterile neutrinos

We discussed two examples of sterile neutrinos with GeV or 10^{12} GeV masses and the consequences of their introduction. Beside these scenarios, anomalous neutrino data reported by LSND [202], MiniBooNE [203, 204], the Gallium experiment [205], and reactor anomaly [206], suggesting the existence of eV sterile neutrinos. Since there is no decisive answer to the anomalous neutrino data, additional experiments searching for eV sterile neutrinos have been proposed. A major push in this direction is the Short Baseline Neutrino (SBN) experimental program at Fermilab, which will have three detectors at different baselines in their experimental setup [207]. This means that they can make quite accurate measurements, thereby limiting the current allowed eV sterile neutrino parameter space in the future. Considering there exist no final answer to the anomalous neutrino data, we study the phenomenology of eV sterile neutrinos in this chapter.

8.1 Method

We consider the anarchy hypothesis as origin of the Dirac and Majorana mass matrices, and we follow Ref. [208] as our guideline. The authors of Ref. [208] consider the minimal setup with two eV sterile neutrinos within the anarchy hypothesis and display distributions of the neutrino masses, the active mixing elements, the active-sterile mixing elements, and the effective beta decay mass. We consider the next-to-minimal setup with three eV sterile neutrinos and discuss differences between the different scenarios.

Rather than relying on the seesaw formula, we consider the full neutrino mass matrix since this method works even outside the seesaw limit, *i.e.* having a much larger Majorana mass matrix than the Dirac mass matrix. The full neutrino mass matrix is given by

$$M_\nu = \begin{pmatrix} 0 & vV_L^* D_Y V_R^T \\ vV_R D_Y V_L^\dagger & M_R \end{pmatrix} = U_{6\times 6}\mathrm{diag}(m_1, m_2, m_3, m_4, m_5, m_6)(U_{6\times 6})^\dagger \,, \tag{8.1.1}$$

where v is the Higgs VEV, $D_Y = \mathrm{diag}(y_1, y_2, y_3)$ is the Yukawa matrix, $M_R = \mathrm{diag}(M_1, M_2, M_3)$

is the Majorana mass matrix[1], $V_{L,R}$ are unitary matrices, $U_{6\times6}$ is the full mixing matrix, and m_i is the neutrino mass. We assume a neutrino mass hierarchy of $m_1 < m_2 < ... < m_6$, and the unitary matrices $V_{L,R}$ are distributed according to the Haar measure Eq. (4.4.1). The eigenvalues of D_Y and M_R are distributed according to [7, 209]

$$dM_R \propto |M_3^2 - M_1^2||M_2^2 - M_1^2||M_3^2 - M_2^2|M_1M_2M_3dM_1dM_2dM_3\,, \tag{8.1.2}$$

$$dD_Y \propto (y_3^2 - y_1^2)^2(y_2^2 - y_1^2)^2(y_3^2 - y_2^2)^2y_1y_2y_3dy_1dy_2dy_3\,, \tag{8.1.3}$$

with the overall scales (y_0 and M_0) being unknown. They are not dictated by the formulas given above, meaning they are, in general, free parameters. However, we constrain the eigenvalues according to $\sum_i y_i^2 \leq y_0^2$ and $\sum_i M_i^2 \leq M_0^2$, fixing the overall scales y_0 and M_0 such that $m_3 \simeq 0.05$ eV and $m_6 \simeq 1$ eV, respectively. This means $M_0 = 1.6$ eV and $y_0 = 1.5 \times 10^{-12}$, similar to Ref. [208]. Beside considering the anarchy hypothesis using a linear measure for the eigenvalues, we consider the Wishart method with $N = 30$ in addition. The Dirac and Majorana matrices are obtained via Eq. (4.4.2), whereafter they are placed into the full neutrino mass matrix Eq. (8.1.1). Thereafter, we obtain the neutrino masses and the active-sterile mixings for the Wishart method.

8.2 Results

Our findings are displayed in Fig. 8.1, showing the mass distributions on the left side and the flavored active-sterile mixings on the right side. Ensuring our method works, we reproduce the results of Ref. [208]. Additionally, this result acts as our basis when computing the other scenarios. Therefore, we must discuss the results more in-depth. With two sterile neutrinos only, the lightest active neutrino is massless, meaning no distribution for m_1 appears in Fig. 8.1A. Again, the two unknown mass scales are used to fix the heaviest of the active and sterile neutrinos to $m_3 \simeq 0.05$ eV and $m_5 \simeq 1$ eV, respectively, thereby narrowing the mass distributions. This is compared to the board mass distributions of m_2 and m_4, even though there is no overlap between the active and sterile neutrino mass distributions. Concerning the active-sterile mixing distributions, they follow an universal distribution, *i.e.* the distributions are independent of flavor. This is an interesting finding, however the flavored mixing elements can still have different values in Nature.

Now, considering three eV sterile neutrinos in the anarchy hypothesis using a linear measure for picking the mass eigenvalues, their mass distributions are shown in Fig. 8.1C. Obviously as

[1] Due to basis-independence of anarchy, we choose a diagonal Majorana mass matrix containing the masses of the sterile neutrinos.

expected, the mass distributions for m_2 and m_3 become more peaked due to the non-zero m_1 distribution, whereas the same occurs for the sterile neutrino mass distributions. Additionally, one can obtain both a hierarchical and a degenerate mass spectrum for the active and sterile neutrinos. Considering the active-sterile mixings, the distribution for the lightest sterile neutrino is independent of flavor only, whereas the other distributions are different from each other. Difficult to notice in Fig. 8.1D, the $|U_{\mu 5}|$ distribution peaks at a larger value compared to the $|U_{e5}|$ and $|U_{\tau 5}|$ distributions. For the heaviest sterile neutrino, it is the tau mixing element distribution which peaks at a larger mixing element value compared the electron and muon distributions. This suggest that the intermediate (heaviest) sterile neutrino mix more with the muon (tau) flavor, even though there is no significant statistical preference for this claim.

Lastly, we consider three eV sterile neutrinos using the Wishart method. The mass distributions move closer to each other, and are more narrow for both the active and sterile neutrinos, meaning a degenerate mass spectrum is more expected rather than a hierarchical spectrum for the case of $N = 30$. Considering the active-sterile mixings, the distributions are, again, independent of flavor, *i.e.* there is an universal active-sterile mixing distribution for each sterile neutrino. This is a direct prediction for the Wishart method, thereby distinguishing itself from a linear anarchy method with 3 sterile neutrinos.

In general, the active-sterile mixing distribution for the lightest sterile neutrino has the largest possible value, meaning experimental searches might discover it first or exclude parts of its parameter space. Quite recently, IceCube has reported limits on the muon and tau mixing elements in a combined fit [210], displaying the allowed parameter space. With limits of $|U_{\mu 4}| \simeq \sqrt{0.1} \simeq 0.34$ for $|U_{\tau 4}| = 0$, one tends to constrain the upper part of the distributions, however they are limited in excluding more of the distributions. This analysis is performed with one sterile neutrino in mind, meaning introducing more sterile neutrinos would worsen their limits due to more degrees of freedom. Therefore, the limits should be taken as a guideline when studying two or three sterile neutrinos. Increasing the sensitivity by an order of magnitude would cut right in the middle of the distributions, meaning nearly half of the parameter space could be potentially excluded. This might be possible with the DUNE experiment [211], however they assumed certain requirements such as CP-conservating δ_{24} and $\sin^2\theta_{34} = 0.1$ in order to obtain a limit $|U_{\mu 4}|^2 \simeq \sin^2\theta_{24} \leq 10^{-2}$. In a more general analysis, the limits might worsen, meaning one cannot set as stringent limits on the active-sterile mixings.

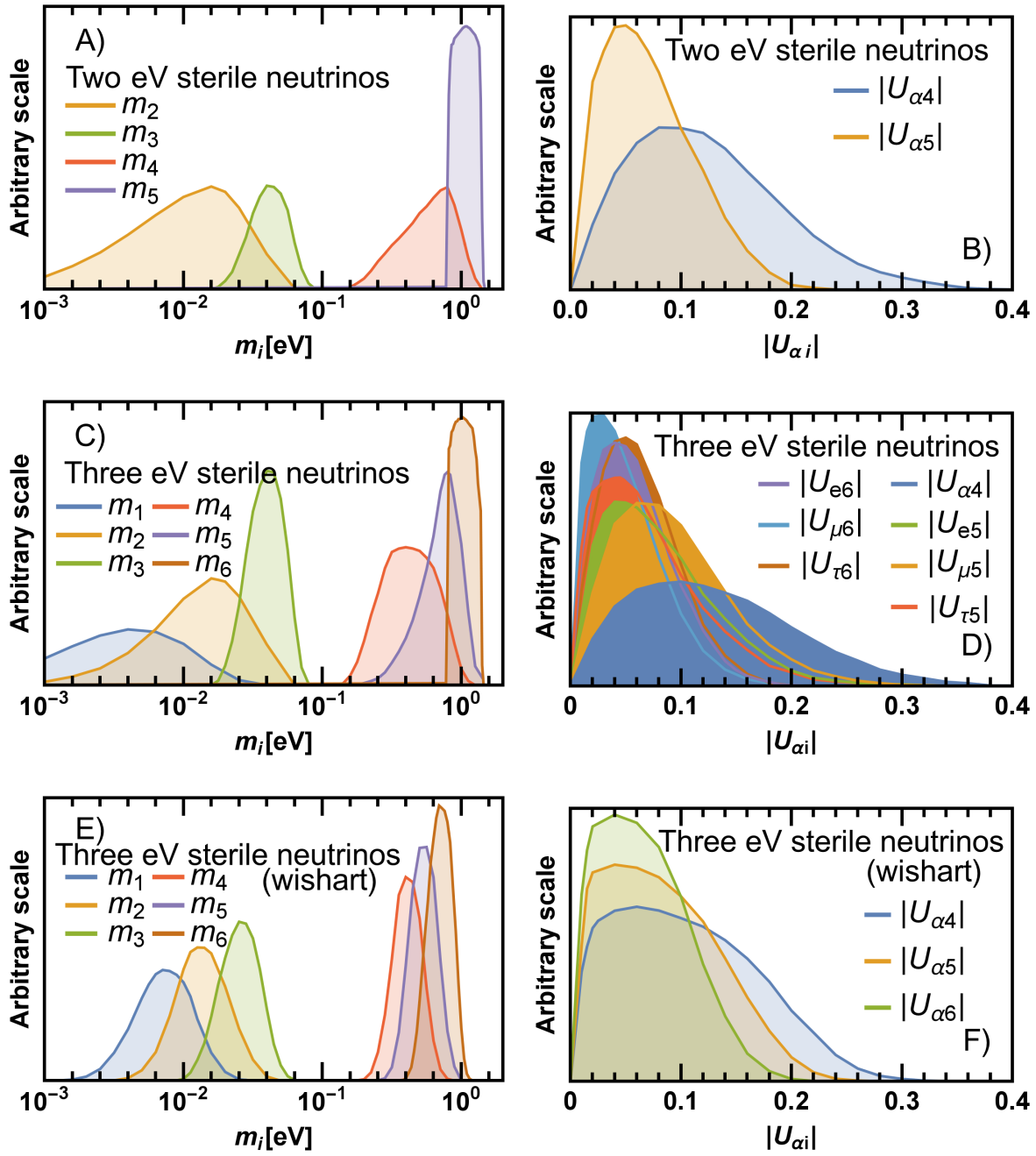

Figure 8.1: (Left) Mass distribution for the active and sterile neutrinos. (Right) The active-sterile mixing of the sterile neutrinos. (Upper) Scenario with two eV sterile neutrinos. (Middle) Scenario with three eV sterile neutrinos. (Bottom) Scenario with three eV sterile neutrinos using the Wishart method when picking the Dirac/Majorana mass matrix.

Chapter 9

Flavor composition of astrophysical neutrinos

Exploring BSM physics indirectly with astrophysical neutrinos, acts as a different alternative to the particle physics experiments considered previously in the dissertation. Astrophysical neutrinos come with a variety of different energies and baselines, making them ideal to study neutrino oscillations under more extreme conditions (higher energies and baselines). Due to their low cross section, means we can look into star's interior and test propagational effects over cosmological distances. Therefore, they are perfect messengers to test BSM physics, and a possible observable is the neutrino flavor composition. We obtain the theoretically allowed parameter space expected from BSM physics, meaning a comparison to the experimental sensitivity of future neutrino telescopes such as IceCube-Gen2 can be made. As a result, a large part of the BSM parameter space can be excluded in the future.

9.1 Method

We explain our logic behind the method used in this chapter and apply it to standard neutrino oscillations. This acts as our basis before we introduce the different BSM scenarios and investigate their allowed theory parameter space. However, there are several uncertainties present in describing the allowed neutrino flavor composition parameter space.

1. Each oscillation parameter is only known to a certain precision.

2. The initial (source) flavor composition is unknown.

3. Unknown theory parameters coming from the BSM scenarios.

We define a coherent approach in order to make a direct comparison among the theory parameter space and the expected precision from future neutrino telescopes. Obtaining BSM parameter space, we display, in principle, the whole allowed theory envelope without weighting certain regions to be more or less likely.

9.1.1 Neutrino mixing and oscillation parameter uncertainties

Neutrinos oscillate while traveling from the astrophysical source to Earth, see Section 3.2 for description of neutrino oscillations. Considering astrophysical neutrinos, the distance is large (roughly of astrophysical scale), meaning the neutrinos lose their coherence while propagating. Therefore, the neutrino oscillation probability becomes[212]

$$\begin{aligned} P_{\alpha\beta} &= \delta_{\alpha\beta} - 2\sum_{i>j=1}^{3} \mathrm{Re}[(U_{\mathrm{PMNS}})_{\alpha i}(U_{\mathrm{PMNS}})^*_{\beta i}(U_{\mathrm{PMNS}})^*_{\alpha j}(U_{\mathrm{PMNS}})_{\beta j}] \\ &= \sum_{i=1}^{3} |(U_{\mathrm{PMNS}})_{\alpha i}|^2 |(U_{\mathrm{PMNS}})_{\beta i}|^2 . \end{aligned} \tag{9.1.1}$$

This means that the flavor mixing is independent of the neutrino mass square differences, while it depends on the mixing parameters $\theta_{12}, \theta_{23}, \theta_{13}$ and δ.

To obtain the allowed parameter space, we choose the neutrino oscillation parameters, however they carry uncertainties themselves, leading to uncertainties in the neutrino flavor composition parameter space. We control the neutrino oscillation parameter uncertainties by defining

$$\chi^2 = \sum_{j>i} \left(\frac{\sin^2\theta_{ij} - \sin^2\theta_{ij}^{\mathrm{bf}}}{\sigma_{\sin^2\theta_{ij}}} \right)^2 , \tag{9.1.2}$$

where the best-fit and uncertainties are taken from Ref. [68], and we allow for an arbitrary value of the CP-violating phase. Requiring $\chi^2 \leq 11.83$ (99% confidence level (CL) for two-dimensional fit), means we obtain the allowed set of neutrino oscillation parameters. Otherwise, we disregard the set of oscillation parameters. Using this setup, we obtain the allowed neutrino flavor mixing.

Beside investigating the currently allowed parameter space, we are also studying the expected flavor composition parameter space allowed in the future. The volume upgrade IceCube-Gen2 [213] is a proposed extension of IceCube with better detector capabilities, meaning a better measurement of the neutrino flavor composition is possible. The expected sensitivity of IceCube-Gen2 is obtained from Ref. [214] and assumes 15 years of data taking. At the start of IceCubeGen2, the neutrino oscillation parameters are known to a higher precision. Therefore, we define a benchmark "Gen2 scenario", and we extrapolate that

$$\begin{aligned} \sin^2\theta_{12} &= 0.306 \pm 0.002 , \qquad \sin^2\theta_{23} = 0.441 \pm 0.01 , \\ \sin^2\theta_{13} &= 0.0217 \pm 0.0005 , \qquad \delta = 261^\circ \pm 15^\circ , \end{aligned} \tag{9.1.3}$$

where the best-fit values are taken from Ref. [68]. The uncertainties are obtained in the following

way: future neutrino oscillation experiments have been proposed, which are supposed to measure the neutrino oscillation parameters with higher precision. A possible first measurement of δ would come from the DUNE experiment, together with a better measurement of θ_{23}. It is estimated that it will constrain these two parameter to $\sigma_{\theta_{23}}^{\mathrm{DUNE}} \simeq 1^\circ$ and $\delta^{\mathrm{DUNE}} \simeq 15^\circ$, respectively, by 2027–2028 [173]. At a similar time (roughly 2026), the JUNO experiment would constrain $\sin^2(\theta_{12})$ to $\sigma_{\sin^2\theta_{12}}^{\mathrm{JUNO}} \simeq 0.003$ [215, 216]. Assuring a common level for the oscillation parameters, means we extrapolate them to the year 2030 by assuming that they scale $\propto 1/\sqrt{\text{exposure}}$. Lastly, we assume that the systematic uncertainty on θ_{13} from short baseline (SBL) reactor experiments will dominate in the end. Therefore, we get a conservative estimate $\sigma_{\sin^2(2\theta_{13})}^{\mathrm{SBL}} = 0.0019$ using the current best measurement from the Daya Bay experiment [217]. As a sidenote, the oscillation parameter δ enters in the χ^2 (similar to θ_{12}, θ_{13} and θ_{23}) in the "Gen2 scenario".

We display our results for normal neutrino mass ordering ($\Delta m^2_{32} > 0$) only. For standard neutrino oscillations, we expect small changes for inverted mass ordering ($\Delta m^2_{32} < 0$) due to the shift of the θ_{23} best-fit value from 40° for normal mass ordering to 50° for inverted mass ordering, see *e.g.* Ref. [218]. Considering the BSM models, most of them have identical parameter space for either mass ordering, except for two scenarios. The cases of neutrino decay and pseudo-Dirac neutrinos change due to the best-fit value of θ_{23} is different for the inverted ordering.

9.1.2 Initial and final neutrino flavor composition

The initial neutrino flavor composition is essential for this study since it defines the allowed range of the final flavor composition within the standard mixing framework. The initial flavor composition of neutrinos and antineutrinos are given by ξ_α and $\xi_{\bar{\alpha}}$, respectively. Usually their sum $\xi_{\alpha+\bar{\alpha}} = \xi_\alpha + \xi_{\bar{\alpha}}$ is used since neutrino telescopes cannot distinguish between neutrinos and antineutrinos. There are a variety of ideal neutrino production channels. The pion decay chain with the initial flavor ratio $(\xi_{e+\bar{e}} : \xi_{\mu+\bar{\mu}} : \xi_{\tau+\bar{\tau}}) = (1/3 : 2/3 : 0)$ is the most used case. However, the muon decay may be damped by magnetic field effects on the secondaries or enhanced to a muon pile-up, leading to $(\xi_{e+\bar{e}} : \xi_{\mu+\bar{\mu}} : \xi_{\tau+\bar{\tau}}) = (0 : 1 : 0)$ [219] or $(\xi_{e+\bar{e}} : \xi_{\mu+\bar{\mu}} : \xi_{\tau+\bar{\tau}}) = (1/2 : 1/2 : 0)$ [220], respectively. Other possibilities considered in the literature include neutrino production by neutron decay $(1 : 0 : 0)$ [221] or charmed meson decays $(1/2 : 1/2 : 0)$ [222] at the highest energies.

From the examples shown above, no significant contribution of tau neutrinos is expected at the source [223]. Due to the large tau lepton mass, it is difficult to produce tau neutrinos at the source. If tau neutrinos are desired at the source, one must also explain its significant contribution to the neutrino flavor composition. Energywise, it is more beneficial to produce pions, kaons and muons at the source, resulting in a flavor composition given by a mixture of

electron and muon neutrinos. Therefore, we parameterize the neutrino flavor composition at the source as $(\xi_{e+\bar{e}} : \xi_{\mu+\bar{\mu}} : \xi_{\tau+\bar{\tau}}) = (x : 1-x : 0)$ with $0 \leq x \leq 1$ (unless stated otherwise) to model realistic source compositions. A different initial flavor composition points to BSM physics.

The neutrino flavor composition at Earth is

$$\xi_{\beta+\bar{\beta},\oplus} = \sum_{\alpha} P_{\alpha\beta}\xi_{\alpha+\bar{\alpha}}\,, \tag{9.1.4}$$

where $\xi_{\beta+\bar{\beta},\oplus} = \xi_{\beta,\oplus} + \xi_{\bar{\beta},\oplus}$ is the final (neutrino+antineutrino) flavor composition, and $\xi_{\beta,\oplus}$ ($\xi_{\bar{\beta},\oplus}$) define the final flavor composition of neutrinos (antineutrinos) only.

9.1.3 Theory model parameters

There are various theory parameters in the different BSM scenarios of either continuous or discrete origin. Take, for example, the scenario of neutrino decay where the neutrino is an unstable particle. In this scenario, there are $2^3 = 8$ different cases (discrete possibilities), since each mass eigenstate can be stable or unstable. Additionally, there are continuous parameters such as their lifetimes and the branching ratios into lighter mass eigenstates.

Therefore, we scan over the continuous parameters in their allowed ranges, whereas we show the impact of different discrete choices. In addition for several cases, we display the "complete envelope" for all possible (discrete and continuous) parameter choices to show the allowed parameter space, and later compare different theories with each other.

9.1.4 Graphical representation

We present our findings for standard mixing as shown in Fig. 9.1, where it is compared to the current (left panel) and future (right panel) IceCube bounds. It displays the electron fraction of the flavor composition along the bottom axis of the triangle, the muon fraction on the right axis, and the tau fraction on the left axis. It varies from zero to one, meaning a specific flavor could contribute nothing at all or solely to the neutrino flavor composition. Additionally, the graphical representation ensures $\sum_{\alpha} \xi_{\alpha+\bar{\alpha},\oplus} = 1$, meaning two of the fractions are independent only. The grey lines (not the IceCube contours) helps decipher the neutrino flavor composition at a given point in the parameter space. Choosing a constant electron fraction from the bottom axis, one must follow the grey lines parallel to the tau fraction axis to keep the electron fraction constant. For a constant muon (tau) flavor, grey lines parallel to the electron (muon) fraction axis have to be followed. Following this procedure, we deduce the best fit point of the currently allowed IceCube bounds at $(\xi_{e+\bar{e},\oplus} : \xi_{\mu+\bar{\mu},\oplus} : \xi_{\tau+\bar{\tau},\oplus}) = (0.5 : 0.5 : 0)$.

In the standard mixing case, the currently published data from the IceCube experiment can

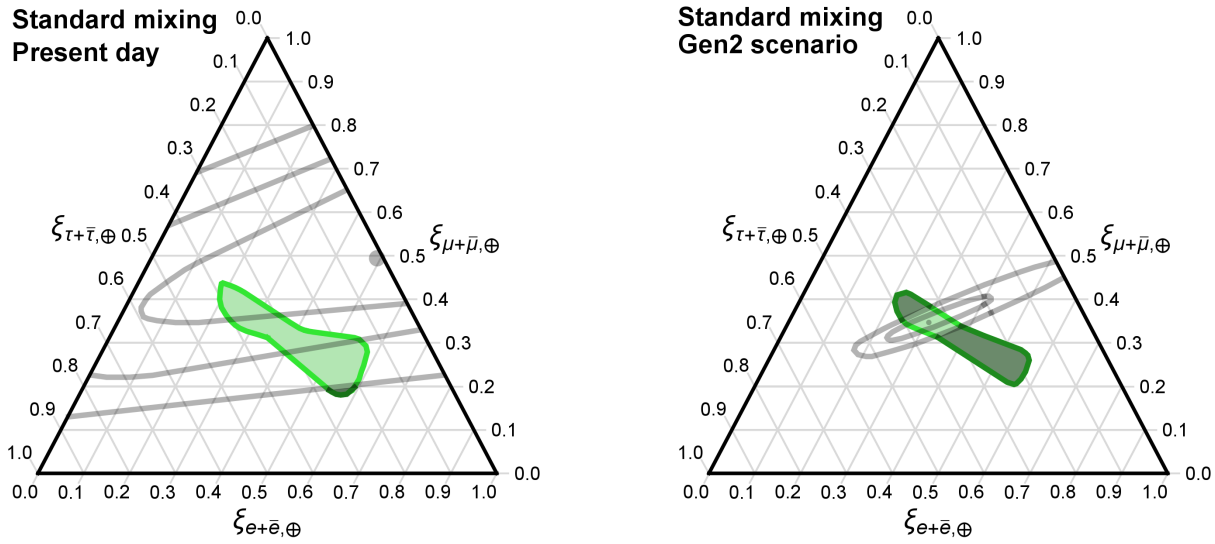

Figure 9.1: The expected flavor composition parameter space from standard neutrino mixing (green shaded region) using current uncertainties (left) and our "Gen2 scenario" benchmark scenario (right). The flavor contours are displayed in grey, showing the 1σ, 2σ (omitted for IceCube-Gen2), and 3σ (2 d.o.f.) allowed regions given by IceCube (current) [224] and IceCube-Gen2 (expected) [214], respectively. The bestfit point is marked by a dot. Figure taken from Ref. [225].

exclude 2% of the parameter space at 99% CL, while IceCube-Gen2 will be able to exclude 73% of the standard mixing region in the future[1]. The darker shaded green regions in Fig. 9.1 show the parts of the parameter space outside the 3σ allowed contours.

Evidently from Fig. 9.1, IceCube is limited in constraining the theory parameter space. Therefore, we show the "Gen2 scenario" only in the rest of the thesis. However, some models, such as those including sterile neutrinos or non-standard neutrino production, have been derived with dedicated models in the literature, making it difficult to extrapolate current uncertainties. In these cases, which we explicitly point out, we use the current uncertainties. Hereafter, we discuss the specific BSM physics and their impact on the neutrino flavor composition.

[1] Decomposing the flavor triangle into smaller triangles, means one can compute the parameter space area within the IceCube-Gen2 region, allowing for an exclusion percentage estimate. Increasing the number of small triangles, gives a more precise estimate.

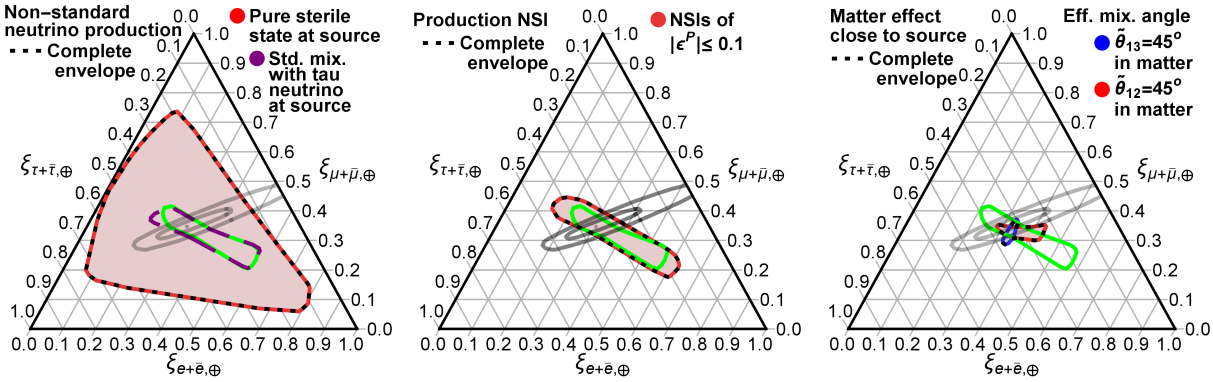

Figure 9.2: The neutrino flavor composition for source effects: non-standard neutrino production (left), non-standard interactions (middle) and matter effect conversions (right). Standard mixing is displayed by the green region, whereas the expected (1σ, 3σ) IceCube-Gen2 flavor bounds are given by the grey contours. The best-fit points are given by a dot. The "complete envelope" shows, in principle, the whole allowed parameter space, and it is shown as the dashed contours. Figure taken from Ref. [225].

9.2 BSM effects at the source

We discuss BSM effects at neutrino production or close to the source, namely non-standard interactions and non-standard neutrino production (production of tau or sterile neutrinos). We describe their impact on the neutrino mixing, and display the allowed neutrino flavor composition parameter space. Not BSM physics, matter effects can also influence the neutrino flavor composition. Therefore, we also investigate this additional effect here.

9.2.1 Non-standard neutrino production

New production channels can occur due to BSM physics, leading to a significant amount of tau or sterile neutrinos at the source. Introducing the tau neutrino flavor at the source within standard neutrino mixing, we parameterize the initial flavor composition as $(\xi_{e+\bar{e}} : \xi_{\mu+\bar{\mu}} : \xi_{\tau+\bar{\tau}}) = (x : y : 1-x-y)$ with $0 \leq x \leq 1$ and $0 \leq y \leq 1-x$, and use the method described previously. Considering production of sterile neutrinos at the source, one must incorporate the sterile neutrino into the method to obtain the allowed parameter space. We construct a 4×4 mixing matrix using the parameterization

$$U_{4\times4} = U_{23}\bar{U}_{13}U_{12}\bar{U}_{14}\bar{U}_{24}U_{34}\,, \tag{9.2.1}$$

where U_{ij} ($\bar{U}_{ij}$) is a real (complex) rotation matrix in the ij plane. Assuming the oscillations averages out, the flavor mixing becomes $P_{\alpha\beta} = \sum_{i=1}^{4} |(U_{4\times4})_{\alpha i}|^2 |(U_{4\times4})_{\beta i}|^2$, and the initial flavor

composition is $(\xi_{e+\bar{e}} : \xi_{\mu+\bar{\mu}} : \xi_{\tau+\bar{\tau}} : \xi_{s+\bar{s}}) = (x : y : z : 1-x-y-z)$ with $0 \leq x \leq 1$, $0 \leq y \leq 1-x$ and $0 \leq z \leq 1-x-y$. However, our χ^2 (Eq. (9.1.2)) depends on an unitary 3×3 mixing matrix, meaning we must define a different procedure to control the oscillation parameters in this scenario. Therefore, we construct a new χ^2 given by

$$\chi^2 = \sum_{\alpha=e,\mu,\tau} \sum_{i=1,2,3} \left(\frac{|U_{\alpha i}| - |U_{\alpha i}|^{\text{bf}}}{\sigma_{|U_{\alpha i}|}} \right)^2 , \tag{9.2.2}$$

where the best-fit values and 1σ uncertainties of the PMNS mixing elements are taken from Ref. [69]. Introducing new physics such as sterile neutrinos, means the mixing matrix becomes larger than the usual 3×3 matrix. In turn, the PMNS mixing matrix is non-unitary since it is a submatrix of the complete mixing matrix, and this will impact the allowed range on the PMNS mixing elements. The authors in Ref. [69] preformed an analysis, constructing a χ^2 depending on the non-unitary neutrino oscillation and use neutrino oscillation data as input to constrain the allowed range of the PMNS mixing matrix elements. We use their results to obtain the parameter space allowed in cases with a sterile neutrino. Note that we did not extrapolate the uncertainties to 2030 in this case. Our method gives results similar to those shown in Fig. 3 of Ref. [226]. Using the enlarged mixing matrix and constraining its mixing elements via Eq. (9.2.2), one obtains the allowed parameter space of this scenario.

From Fig. 9.2 left panel, the allowed parameter space is shown together with the standard mixing expectation and compared to IceCube-Gen2 sensitivity bounds. Including tau neutrinos at the source for standard mixing, affects the parameter space very little due to the large θ_{23} mixing. However, a substantial amount of sterile neutrinos at production leads to clear deviations from the standard mixing parameter space. Potentially, 93 % of the (currently) allowed parameter space can be excluded by IceCube-Gen2.

9.2.2 Non-standard interactions at production

Higher dimensional operators might lead to effective non-standard interactions (NSIs), meaning BSM physics occurs at production directly. Since neutrino production and detection are usually different, means this BSM scenario might affect either one or both. We discuss NSIs at production, where the neutrino states are [227]

$$|\nu_\alpha^P\rangle = (1+\epsilon^P) U_{\text{PMNS}} |\nu_i\rangle \quad \text{and} \quad \langle \nu_\beta^D| = \langle \nu_i | U_{\text{PMNS}}^\dagger \,, \tag{9.2.3}$$

where $|\nu_\alpha^P\rangle$ ($\langle \nu_\beta^D|$) represents the neutrino at production (detection), $|\nu_i\rangle$ is the mass eigenstate, U_{PMNS} is the PMNS mixing matrix, and ϵ^P are the NSIs at production. Over astrophysical

distance, the flavor mixing becomes [227]

$$P_{\alpha\beta} = \sum_i |\mathcal{J}^i_{\alpha\beta}|^2 \quad \text{with} \quad \mathcal{J}^i_{\alpha\beta} = (U_{\text{PMNS}})^*_{\alpha i}(U_{\text{PMNS}})_{\beta i} + \sum_\gamma \epsilon^P_{\alpha\gamma}(U_{\text{PMNS}})^*_{\gamma i}(U_{\text{PMNS}})_{\beta i}. \tag{9.2.4}$$

We consider complex production NSIs, requiring $|\epsilon^P| \leq 0.1$ as suggested by current experimental constraints [227, 228], and we quantify the allowed neutrino oscillation parameters by Eq. (9.1.2). Using this procedure, we obtain the flavor composition which is shown in Fig. 9.2 (middle panel). As seen from the figure, given the current experimental data, small deviations are possible.

9.2.3 Constant matter effects close to source

Not necessarily BSM physics, matter effects [70–72] close to the source might affect the neutrino flavor composition. It can, for instance, occur for hidden astrophysical jets [229–233]. Therefore, we consider this standard mechanism as exceptional, since it couples standard neutrino mixing with a special astrophysical environment. For simplicity, we consider a constant SM matter density close to the source with the Hamiltonian

$$\mathcal{H}_{\text{tot}} = \frac{1}{2E} U_{\text{PMNS}} \begin{pmatrix} 0 & 0 & 0 \\ 0 & \Delta m^2_{21} & 0 \\ 0 & 0 & \Delta m^2_{32} \end{pmatrix} U^\dagger_{\text{PMNS}} + \begin{pmatrix} V_e & 0 & 0 \\ 0 & 0 & 0 \\ 0 & 0 & 0 \end{pmatrix}, \tag{9.2.5}$$

where $V_e = 2\sqrt{2} G_F E N_e$ is the matter potential, G_F is the Fermi coupling constant and N_e is the electron density. We fix the neutrino energy to $E = 100$ TeV, and the mass square differences are chosen from their 3σ ranges [68]. Due to constant matter effects, the flavor mixing simplifies to

$$P_{\alpha\beta}\left(L_{\text{vac}}, L_{\text{m}}\right) = |\langle \nu_\beta | U_{\text{PMNS}} e^{-i\mathcal{H}_{\text{vac}} L_{\text{vac}}} U^\dagger_{\text{PMNS}} U_{\text{m}} e^{-i\mathcal{H}_{\text{m}} L_{\text{m}}} U^\dagger_{\text{m}} | \nu_\alpha \rangle|^2 , \tag{9.2.6}$$

where $\mathcal{H}_{\text{m}} = U^\dagger_{\text{m}} \mathcal{H}_{\text{tot}} U_{\text{m}} = \frac{1}{2E}\text{diag}(0, \Delta m^2_{21,\text{m}}, \Delta m^2_{32,\text{m}})$ with "m" as subscript for matter, $\mathcal{H}_{\text{vac}} = \frac{1}{2E}\text{diag}(0, \Delta m^2_{21}, \Delta m^2_{32})$ and L_{vac} (L_{m}) is the distance in vacuum (matter). We use the procedure described in Section 9.1 to obtain the neutrino oscillation parameters. Including decoherence effects and different neutrino production areas within the source, means we average the flavor mixing over distance

$$\bar{P}_{\alpha\beta} = \int_0^{L_{\text{vac}}} \int_0^{L_{\text{m}}} P_{\alpha\beta}\left(L'_{\text{vac}}, L'_{\text{m}}\right) \frac{dL'_{\text{vac}}}{L_{\text{vac}}} \frac{dL'_{\text{m}}}{L_{\text{m}}}.$$

We have no information about the matter distance, meaning an arbitrary L_{m} is allowed. However, in practice, we use the range $L_{\text{m}} \in [0, 10^{10}]$ km. The vacuum distance L_{vac} obeys

$L_{\text{vac}} \gg L_{\text{coh}} \simeq 2E/\Delta m^2_{21} \simeq 5 \cdot 10^9$ km to include decoherence, therefore we parameterize $L_{\text{vac}} = [10, 100] L_{\text{coh}}$. Ensuring decoherence, gives the lower limit. The upper limit can be arbitrary, and changing it does not influence the flavor composition (we checked this numerically) in our study. We consider either $\theta_{12}^{\text{matter}} = 45°$ or $\theta_{13}^{\text{matter}} = 45°$ for a 100 TeV neutrino, meaning we set the electron matter density equal to $N_e = 2 \cdot 10^{18}$ cm^{-3} or $N_e = 8.7 \cdot 10^{19}$ cm^{-3}, respectively. These electron densities are found in Gamma Ray Bursts (GRBs) and Supernovae (SNe) at radii $r \approx 10^{12}$ cm [234–237], however they are fairly low compared to the Earth density, $N_e^{\text{Earth}} \approx 10^{24}$ cm^{-3}, and GRB/SNe core density, $N_e^{\text{core}} \approx 10^{33}$ cm^{-3}. Additionally, we consider $\theta_{23}^{\text{matter}} = 45°$ using our method, but very little changes the flavor composition. Due to θ_{23} being compatible with 45° in vacuum, means $\theta_{23}^{\text{matter}} \simeq 45°$ in our case.

The allowed parameter space of the neutrino flavor composition is displayed in Fig. 9.2 (right) for the two cases described above. Due to the fine-tuned value of N_e, the regions are smaller than the standard mixing expectation, however they might slightly leave it.

Besides this result, we scanned for various values of N_e and computed the neutrino flavor composition parameter space (not shown here). The result of the scans was the following: for a low electron density, the standard mixing term dominates in the Hamiltonian Eq. (9.2.5), leading to the standard mixing parameter space. Increasing the electron density, the parameter space becomes a small circular region as in Fig. 9.2 due to the resonant behavior. Increasing the electron density further, the matter term dominates, meaning no oscillations occur inside the matter, *i.e.* they keep their flavor until they reach vacuum. Thereafter, they undergo standard mixing, leading to the same parameter space as standard mixing. Therefore, a varying matter density may alter the flavor composition, however it requires a resonant matter density and a minimum matter width/distance [234] for matter effects to be important. Considering astrophysical sources, one can define them as optically thin or optically thick. In the former (latter) case, the neutrino is (not) accompanied by an electromagnetic counterpart. For optically thick source, it is dense enough to satisfy the requirements given above, whereas it is not for optically thin sources [235]. A source with a choked jet is a possible example, and it has been studied in the context of GRBs [238, 239], SNe [240] and Active Galactic Nuclei (AGNs) [241, 242]. These and other studies [229, 235] find a significant change in flavor composition due to matter effects. Therefore, varying matter effects may considerably modify the flavor composition, whereas, as in our case, a constant matter density has some effect.

9.3 BSM effects during propagation

There are many BSM scenarios which can affect the neutrino propagation, leading to a different neutrino flavor composition parameter space. Scenarios includes pseudo-Dirac neutrinos,

neutrino decay, quantum decoherence, mixing with sterile neutrinos during propagation, new physics entering via effective operators, neutrino-DM interactions, and sterile neutrino shortcut through extra dimensions. We describe them individually in each subsection and display the allowed parameter space in Fig. 9.3.

9.3.1 Pseudo-Dirac neutrinos

Assuming neutrinos being Dirac particles, one must introduce sterile partners in order to write a Dirac mass m_D. The active and sterile neutrino mix maximally, but no oscillations occurs among them since they have the same mass, *i.e.* their mass square difference is $\delta m^2 = 0$. However, assuming a small Majorana mass between the sterile neutrinos, *i.e.* $M_R \ll m_D$, lifts the mass degeneracy. This leads to the scenario of pseudo-Dirac neutrinos [243–245]. This example can be generated by assuming lepton number being an approximate fundamental symmetry, thereby fulfilling the condition $M_R \ll m_D$. If neutrinos are pseudo-Dirac particles, the mass square difference between the active and sterile neutrino pair is very small, and due to the astrophysical baseline, neutrino telescopes can ideally constrain this scenario [246–248]. After averaging the mass square differences Δm^2_{21} and Δm^2_{32}, the flavor mixing in the pseudo-Dirac scenario becomes [246]

$$P_{\alpha\beta}(L, \delta m^2_1, \delta m^2_2, \delta m^2_3) = \sum_{j=1}^{3} |(U_{\rm PMNS})_{\alpha j}|^2 |(U_{\rm PMNS})_{\beta i}|^2 \left[1 - \sin^2\left(\frac{\delta m^2_j L}{4E}\right)\right] , \tag{9.3.1}$$

where $\delta m^2_j = (m^+_j)^2 - (m^-_j)^2$ with m^+_j (m^-_j) being the heavier (lighter) of the active-sterile neutrino pair j. Due to the smallness of δm^2_j, they do not (necessarily) averaged out over astrophysical distances. We introduce three sterile neutrinos, meaning three δm^2_js, however one or several might be zero if the active and sterile neutrino have identical mass or one reduces the number of sterile neutrinos. The mass square differences δm^2_j and the energy E are unknown, however we choose $E \in [10, 10^4]$ TeV and $\delta m^2_j \in [10^{-17}, 10^{-19}]$ eV^2, the range neutrino telescopes can probe [248]. Additionally, the baseline is unknown, but we average over the baseline, obtaining the flavor mixing

$$\bar{P}_{\alpha\beta} = \int_0^L P_{\alpha\beta}(L', \delta m^2_1, \delta m^2_2, \delta m^2_3) \frac{dL'}{L}. \tag{9.3.2}$$

We require $L \gg L_{\rm coh} \simeq 2E/\Delta m^2_{21} \simeq 5 \cdot 10^9$ km to average Δm^2_{21} and Δm^2_{32} out (requirement for Eq. (9.3.1) to be valid). There are $2^3 = 8$ different possibilities since we can either scan over the mass square differences or set it equal to zero. Standard mixing is obtained if all mass square differences are equal to zero. Therefore, we omit this specific scenario. The other remaining

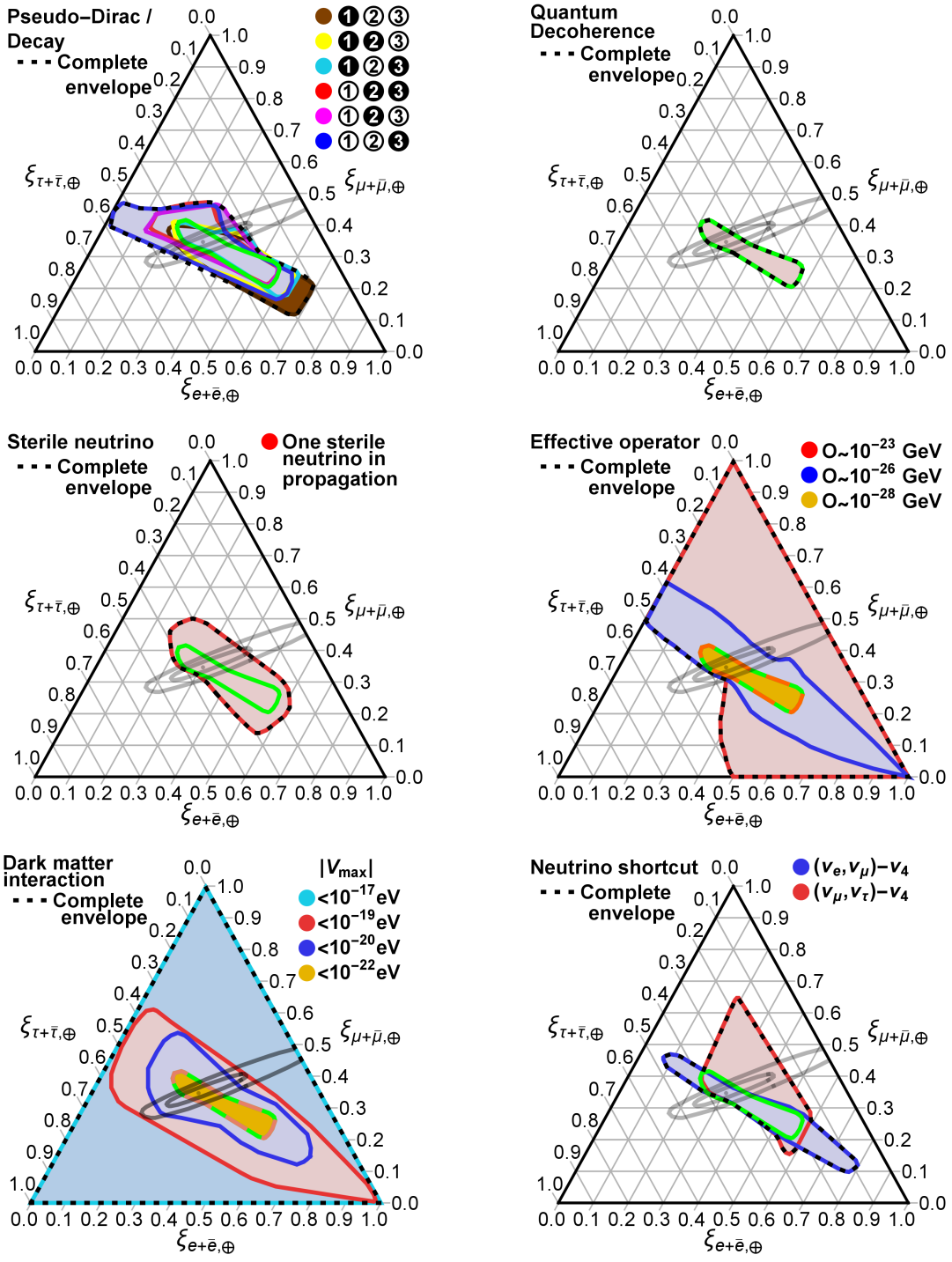

Figure 9.3: The allowed flavor compositions for six different BSM propagation effects. Standard mixing is displayed by the green region, whereas the expected (1σ, 3σ) IceCube-Gen2 flavor bounds are given by the grey contours. The best-fit points are given by a dot. The "complete envelope" shows, in principle, the whole allowed parameter space, and it is shown as the dashed contours. Figure taken from Ref. [225].

cases are represented using the disk notation (except one), where a filled disk corresponds to $\sin^2 = 0$ and we scan for the mass square difference for an unfilled disk. For example, "❶②③" means that $\sin^2(\delta m_1^2 L/(4E)) = 0$, and the other two $\sin^2 \neq 0$. We do not show the disk notation for the scenario '①②③" in the figure, but the complete envelope is given by this scenario since all three mass square differences are present in the flavor mixing.

Our results are shown in the upper left panel of Fig. 9.3, including the envelope of all possible scenarios. The figure demonstrates that large deviations from the standard mixing can be expected.

9.3.2 Neutrino decay

In this subsection, we consider neutrinos being unstable particles, meaning they decay during their propagation toward Earth. Neutrinos decaying incompletely into invisible decay products alters the flavor mixing. It is then given by [249]

$$P_{\alpha\beta} = \sum_{i=3}^{3} |(U_{\text{PMNS}})_{\alpha i}|^2 |(U_{\text{PMNS}})_{\beta i}|^2 \exp\left(-\frac{L m_i}{E \tau_i}\right), \tag{9.3.3}$$

where the rest frame lifetime τ_i of the ν_i mass eigenstate is boosted into the laboratory frame by $\gamma = E/m_i$. The baseline L and energy E are determined experimentally, and one usually quotes τ_i/m_i as the neutrino lifetime since the neutrino mass m_i is unknown. The current limits are the following: $\tau_1/m_1 \gtrsim 10^5$ s/eV for ν_1 from SN1987A [250], $\tau_2/m_2 \gtrsim 10^{-4}$ s/eV for ν_2 from solar neutrinos [251–254], and atmospheric and long-baseline neutrino oscillation data provides $\tau_3/m_3 \gtrsim 10^{-10}$ s/eV for ν_3 [255]. Possible lifetimes of $\tau/m \gtrsim 10^2 \frac{L}{\text{Mpc}} \frac{\text{TeV}}{E}$ s/eV [256] might be probed by neutrino telescopes.

We describe neutrino decay by the Hamiltonian [257]

$$\mathcal{H}_{\text{tot}} = \frac{1}{2E} U_{\text{PMNS}} \left[\begin{pmatrix} 0 & 0 & 0 \\ 0 & \Delta m_{21}^2 & 0 \\ 0 & 0 & \Delta m_{32}^2 \end{pmatrix} + i \begin{pmatrix} -\lambda_1 & \lambda_2 \text{Br}_{2\to1} & \lambda_3 \text{Br}_{3\to1} \\ 0 & -\lambda_2 & \lambda_3 \text{Br}_{3\to2} \\ 0 & 0 & -\lambda_3 \end{pmatrix} \right] U_{\text{PMNS}}^\dagger , \tag{9.3.4}$$

where standard mixing is given by the first term and neutrino decay is given by the second term. We define $\lambda_i = m_i/\tau_i$, and an effective branching ratio between the j and i mass eigenstate is given by $\text{Br}_{j\to i}$. Due to kinematics, the decay term is an upper triangular matrix (lighter mass eigenstates can not decay into heavier mass eigenstates), whereas for inverted mass ordering, it is a lower triangular matrix. We use Eq. (9.3.4) instead of Eq. (9.3.3), since the latter equation has a shortcoming, namely the possibility of the heavier mass eigenstates repopulating the lighter mass eigenstates. This is included in Eq. (9.3.4) by the off-diagonal elements in the second term.

Setting the branching ratios equal to zero, one obtains Eq. (9.3.3) from Eq. (9.3.4). We scan in the intervals $\Delta m^2_{21} \in [7.03, 8.09] \cdot 10^{-5}$ eV, $\Delta m^2_{32} \in [2.41, 2.64] \cdot 10^{-3}$ eV and $E \in [10, 10^4]$ TeV for the theory parameters, and compute the flavor mixing via

$$\bar{P}_{\alpha\beta} = \frac{1}{L} \int_0^L |\langle \nu_\beta | V e^{-i\tilde{\lambda} L'} V^\dagger | \nu_\alpha \rangle|^2 dL', \tag{9.3.5}$$

where $\mathcal{H}_{\rm tot} = V\tilde{\lambda}V^\dagger$, V is an unitary matrix and $\tilde{\lambda} = {\rm diag}(\tilde{\lambda}_1, \tilde{\lambda}_2, \tilde{\lambda}_3)$ with $\tilde{\lambda}_i$ being real. We require $L \gg L_{\rm coh} \simeq 2E/\Delta m^2_{21}$ to include decoherence effects, where $L_{\rm coh}$ is the coherence distance, however L can not exceed the Hubble distance, see Ref. [258] for explanation. There are $2^3 = 8$ possibilities of neutrino decays, since either neutrino may be stable or not; intermediate unstable states can be integrated out [259]. We investigate seven cases out of eight possible since one obtains standard mixing when all neutrinos are stable. We use the disk notation again, for instance, "❶②③" means ν_1 stable and ν_2, ν_3 unstable. Possible scenarios and branchings for the different mass orderings are discussed in Ref. [259].

In Fig. 9.3 upper left, the expected flavor composition for each neutrino decay scenario is shown. The complete envelope is generated by assuming all neutrinos being unstable, however they cannot decay completely since an astrophysical neutrino flux is seen at Earth. Roughly 85% of the complete neutrino decay envelope can be excluded by IceCube-Gen2.

Considering a comparison between neutrino decay and pseudo-Dirac, shows they generate the same envelope in the neutrino flavor composition parameter space. Essentially, Eq. (9.3.1) looks similar to Eq. (9.3.3) with $[1 - \sin^2(\delta m^2_i L/(4E))] = \exp(-Lm_i)/(E\tau_i)$. Therefore, a specific set of parameters for neutrino decay and pseudo-Dirac will generate the same flavor composition. Scanning over different parameters, means one obtain the same complete envelope for both scenarios. While we use Eq. (9.3.4) for decay, due to marginalization of decay rates and branchings, averaging the flavor mixing over astrophysical distances, and the off-diagonal elements in the decay term being smaller than the diagonal elements, *i.e.* $|\lambda_i| \geq |\lambda_i {\rm Br}_{i\to j}|$, means re-occupations of mass eigenstates are equivalent to use Eq. (9.3.3) with lower decay rates. Therefore, one reproduces the same parameter space for the decay and pseudo-Dirac cases, even though we use Eq. (9.3.4) instead of Eq. (9.3.3).

9.3.3 Quantum decoherence

A different BSM scenario is quantum decoherence [260, 261], and the flavor mixing is given by [262]

$$P_{\alpha\beta} = \frac{1}{3} + \frac{1}{2}(|U_{\alpha1}|^2 - |U_{\alpha2}|^2)(|U_{\beta1}|^2 - |U_{\beta2}|^2)\mathrm{e}^{-2\Psi LE^n} + \frac{1}{6}(|U_{\alpha1}|^2 + |U_{\alpha2}|^2 - 2|U_{\alpha3}|^2)(|U_{\beta1}|^2 + |U_{\beta2}|^2 - 2|U_{\beta3}|^2)\mathrm{e}^{-2\Gamma LE^n}\,, \tag{9.3.6}$$

where Ψ and Γ are quantum decoherence parameters. The energy dependence of the specific model is given by n, and usual values are $n = -1, 0, 2$ [263]. Interestingly, quantum decoherence can occur as a high energy effect such as a remnant of a quantum theory of gravity. Rather than choosing a specific model with its theory parameters, we choose the exponential factors between zero and one together with mixing elements constrained by Eq. (9.1.2). In Fig. 9.3 upper right corner, we display the allowed parameter space. Evidently, it generates a similar envelope as standard mixing, meaning it is difficult to distinguish them. However, quantum decoherence might produce interesting energy-dependent effects, as we will discuss later.

9.3.4 Sterile neutrinos

We consider mixing between active and sterile neutrinos during their propagation and the impact on the flavor composition. Using the same method as in Section 9.2.1, we restrict the initial flavor composition to be a mixture of electron and muon neutrinos. From this procedure, we obtain the allowed parameter space shown in the middle left panel of Fig. 9.3. This region is significantly larger than the standard mixing region, and IceCube-Gen2 can exclude 86% of it. As a sidenote, we use the current bounds on the mixing matrix elements, meaning the region will slightly shrink in the future.

9.3.5 Effective operators

New physics may originate from higher-dimensional effective operators in a high-energy scale theory. Due to the general method of effective operators, possible new physics examples includes Lorentz and CPT violation, non-standard neutrino interactions, and neutrino-DM interactions with constant potential, just to mention a few examples. The Hamiltonian is given by [264]

$$\begin{aligned} H_{\rm tot} &= \frac{1}{2E}U_{\rm PMNS}\mathrm{diag}(0, \Delta m^2_{21}, \Delta m^2_{32})U^\dagger_{\rm PMNS} + \sum_n \left(\frac{E}{\Lambda_n}\right)^n \tilde{U}_n \mathcal{O}\mathrm{diag}(O_{n,1}, O_{n,2}, O_{n,3})\tilde{U}^\dagger_n \\ &= V\mathrm{diag}(\Delta_1, \Delta_2, \Delta_3)V^\dagger\,, \end{aligned} \tag{9.3.7}$$

where V is the mixing matrix that diagonalizes H_{tot} and $O_{n,i} \sim \mathrm{O}(1)$ for $i \in [1,3]$. We choose $n = 1$ since the lower terms are more relevant in a renormalizable quantum field theory, *i.e.* $(E/\Lambda_n) \ll 1$ for every n. We choose $\tilde{U}_1$ in a parameterization-independent way (similar to the anarchy hypothesis), meaning we obtain the whole allowed parameter space. Current neutrino oscillation data gives an upper limit on the effective operator coupling strength $\mathcal{O} \sim 10^{-23}$ GeV [265, 266]. We study three specific cases:

- Coupling strength $\mathcal{O} \sim 10^{-23}$ GeV with $\Lambda_1 = 1$ TeV
- Coupling strength $\mathcal{O} \sim 10^{-26}$ GeV with $\Lambda_1 = 35$ TeV
- Coupling strength $\mathcal{O} \sim 10^{-28}$ GeV with $\Lambda_1 = 2$ PeV

The first case represents the current limit, whereas the latter two cases are interesting since new physics is similar in magnitude as the mass term in the Hamiltonian with a neutrino energy of $E = 35$ TeV and $E = 2$ PeV, respectively [264]. This means one can investigate whether IceCube-Gen2 can set stronger limits on the coupling strength for the measured neutrino energy range. The flavor mixing depends on the matrix V since it diagonalizes the Hamiltonian, meaning $P_{\alpha\beta} = \sum_{i=1}^{3} |V_{\alpha i}|^2 |V_{\beta i}|^2$ for this BSM scenario.

In Fig. 9.3 middle right, the effective operator parameter space is shown for different cases. Almost everything is covered, except the ν_τ corner. This is due to an unitary V and excluding the initial tau flavor composition. If one allows for tau neutrinos at the source or a non-unitary V, the lower left corner is probed [264]. Nearly 94% of the complete envelope can be excluded by IceCube-Gen2.

9.3.6 Interaction with dark matter

Neutrinos might interact with dark matter (DM) when propagating from the source to Earth. The effect of neutrino-DM interactions introduces a potential in the Hamiltonian [267]

$$\mathcal{H}_{\text{tot}} = \frac{1}{2E} U_{\text{PMNS}} \begin{pmatrix} 0 & 0 & 0 \\ 0 & \Delta m^2_{21} & 0 \\ 0 & 0 & \Delta m^2_{32} \end{pmatrix} U^{\dagger}_{\text{PMNS}} + \mathcal{V}\,, \tag{9.3.8}$$

where $\mathcal{V}_{\alpha\beta} = \lambda_{\alpha\beta} G_F N_\chi$ describes the interaction between neutrinos and DM, $\lambda_{\alpha\beta}$ is a Hermitian matrix containing the $\pm O(1)$ coupling between neutrinos and DM, G_F is the Fermi constant, and N_χ is the dark matter number density, which is related to the energy density by $N_\chi = \rho_{\text{DM}}/m_{\text{DM}}$. We use the Navarro-Frenk-White (NFW) DM distribution for ρ_{DM}, and it is given

by $\rho_{\rm NFW}(r) = \rho_{\rm DM}(r, 20\ {\rm kpc}, 1, 3, 1)$ [268, 269] with the general parameterization

$$\rho_{\rm DM}(r, r_s, \alpha, \beta, \gamma) = \rho_\oplus \left(\frac{r_\oplus}{r}\right)^\gamma \left(\frac{1 + (r_\oplus/r_s)^\alpha}{1 + (r/r_s)^\alpha}\right)^{(\beta-\gamma)/\alpha} . \tag{9.3.9}$$

Spherical symmetry is assumed in the derivation, and $r = 0$ corresponds to the Galactic Center (GC). The solar system is roughly $r_\oplus = 8.5$ kpc from the GC, and several studies show $\rho_\oplus = 0.4\ {\rm GeV/cm^3}$ [270–272]. Most dark matter distribution profiles are described using the distance from the GC to the neutrino, however we are not sitting in the GC. Therefore, we relate this distance to the line of sight distance l and the angle ϕ with respect to the solar system via $r^2 = r_\oplus^2 + l^2 - 2r_\oplus l\cos\phi$. We scan for the ranges $\phi \in [\pi/2, \pi]$ and $l \in [0, 20]$ kpc, ensuring decoherence effects. The flavor mixing depends on these two quantities

$$P_{\alpha\beta} = |\langle\nu_\beta|\Pi_{i=1}^n U_f(l_i, \phi)|\nu_\alpha\rangle|^2 = |\langle\nu_\beta|\Pi_{i=1}^n U(l_i, \phi)e^{-i\mathcal{H}_{\rm diag}l_i}U^\dagger(l_i, \phi)|\nu_\alpha\rangle|^2 , \tag{9.3.10}$$

where $U_f(l_i, \phi) = U(l_i, \phi)e^{-i\mathcal{H}_{\rm diag}l_i}U^\dagger(l_i, \phi)$ is the transportation matrix and $\mathcal{H}_{\rm diag} = U^\dagger(l_i, \phi)\mathcal{H}_{\rm tot}U(l_i, \phi) = \frac{1}{2E}{\rm diag}(0, (\Delta m^2_{21,{\rm eff}})_i, (\Delta m^2_{32,{\rm eff}})_i)$. Here, i is the specific timestep in our computation of diagonalizing the Hamiltonian, whereas n defines the total number of timesteps. According to Ref. [267], the flavor mixing simplifies since the neutrino propagation is adiabatic, meaning

$$P_{\alpha\beta} = |\langle\nu_\beta|U(0, \phi)e^{-i\mathcal{H}_{\rm diag}l}U^\dagger(l, \phi)|\nu_\alpha\rangle|^2. \tag{9.3.11}$$

By scanning for different distances and angles, the allowed flavor composition is computed, and the flavor composition for this case is shown in Fig. 9.3 (lower left panel) for various neutrino-DM coupling strengths. This BSM effect is unique since it is the only scenario covering the entire flavor triangle.

Comparing this scenario to the effective operator case, seems interesting since they, phenomenologically speaking, look similar at first sight. Adding a potential governing the new physics, means one can generate the allowed theory envelope. However, the two scenarios occupy different percentages of the whole parameter space. It should be understood the following way: the DM density varies as a function of distance from the GC, whereas the potential is constant for the effective operator case. If the potential in the DM scenario is constant, the parameter space becomes the same as for the effective operator parameter space.

Additional information can be derived for this scenario using the arrival direction of the neutrinos. Many DM density profiles expect a higher density at the GC, whereas one have a lower density far away from the GC. In turn, one expects larger deviations in the flavor composition when looking towards the GC. Therefore, one can, in principle, discriminate this

model by investigating the arrival direction.

9.3.7 Sterile neutrino shortcut through extra dimension

Extra dimensions are introduced in many string-like BSM models, and it embeds a four dimensional (time + spatial dimensions) brane in an extra-dimensional bulk [273–278]. The SM particles are confined to the brane by the SM's symmetries, whereas any singlet particle, *i.e.* sterile neutrino, may travel off the brane, thereby changing the flavor composition. The line element is given by [279–281]

$$ds^2 = dt^2 - \sum_{i=1}^{3} \eta^2(u)(dx^i)^2 - du^2 \,, \tag{9.3.12}$$

where the extra dimension is given by u, and $\eta^2(u)$ describes the brane's embedding in the bulk. Having a flat brane embedding, means the geodesics of the sterile and active neutrinos are the same. However, a curved brane embedding, results in a different trajectory for the sterile neutrino. In turn, its dispersion relation is altered, meaning the sterile neutrino will experience a shorter propagation time. Therefore, the effective two-flavor mixing angle becomes [273]

$$\sin^2(2\tilde{\theta}) = \frac{\sin^2(2\theta)}{\sin^2(2\theta) + \cos^2(2\theta)\left[1 - \left(\frac{E}{E_{\rm res}}\right)\right]^2} \,, \tag{9.3.13}$$

where $E_{\rm res} = \sqrt{\delta m^2 \cos(2\theta)/(2\epsilon)}$ denotes the resonance energy. Here δm^2 is the mass square difference in vacuum between the sterile and active neutrino state, θ is the active-sterile mixing angle in vacuum and ϵ is the shortcut parameter, $\epsilon = \delta t/t$, defined as the normalized difference of propagation times on the brane and in the bulk. This scenario leads to an energy-dependent mixing matrix, namely $E \gg E_{\rm res}$ and $E \ll E_{\rm res}$ resembles standard mixing if no significant mixing between the active and sterile state occurs, whereas the PMNS mixing matrix becomes non-unitary for $E \to E_{\rm res}$ (we discuss this feature in detail later). With this in mind, we compute the flavor composition at $E = E_{\rm res}$, meaning $\tilde{\theta} = 45°$, to investigate the maximal impact for this scenario.

We follow Ref. [282], which assumes that the active-sterile mixing angles in a four neutrino framework are described by Eq. (9.3.13), and we adopt their scenarios only. Therefore, this is a conservative estimation of the allowed parameter space for this scenario, whereas one must describe this effect by a 4×4 Hamiltonian to begin with in order to obtain the complete parameter space in a four neutrino framework. However, at least to our knowledge, there is no such Hamiltonian available in the literature. Again, we set $E = E_{\rm res}$ to study the maximal

impact on the flavor composition, meaning the active-sterile mixing angles are $\tilde{\theta} = 45°$. If $E \neq E_{\rm res}$, then $\tilde{\theta}$ is computed by Eq. (9.3.13) and depends on θ, similar to Ref. [282]. We use Eq. (9.1.2) to constrain the neutrino oscillation parameters, and we parameterize the mixing matrix as $U_{4\times4} = U_{23}\bar{U}_{13}U_{12}\bar{U}_{14}\bar{U}_{24}U_{34}$. We investigate two cases taken from Ref. [282], where $\tilde{\theta}$ refers to the mixing angle including the extra dimension shortcut:

- Sterile neutrino mixes with the electron and muon neutrino at the same strength, *i.e.* $\tilde{\theta}_{14} = \pi/4$, $\tilde{\theta}_{24} = \pi/4$ and $\tilde{\theta}_{34} = 0$.
- Sterile neutrino mixes with the muon and tau neutrino at the same strength, *i.e.* $\tilde{\theta}_{14} = 0$, $\tilde{\theta}_{24} = \pi/4$ and $\tilde{\theta}_{34} = \pi/4$.

In the lower right panel of Fig. 9.3, the parameter space of these two cases shows large deviations from standard mixing, and it is possible for IceCube-Gen2 to exclude 80% of the combined parameter space of these two cases. Additionally, we tested other cases with effective maximal mixing between the sterile neutrino and all of the active ones. It produces even larger flavor composition deviations, however, given the effective two-flavor description used in our method, these cases might not be true when implemented in a four neutrino framework (see Section 9.9 for further discussion).

9.4 BSM effects at detection

Lastly, we consider BSM physics near or close to the detector in this section. Examples includes NSIs at detection and Earth matter NSIs, and we investigate their allowed neutrino flavor composition parameter space.

9.4.1 Non-standard interactions in Earth matter

Transversing Earth, neutrinos experience matter effects before they are detected, however it is neglectable for TeV neutrinos (more important for GeV neutrinos due to the high electron density) [283]. However, NSIs in Earth matter is possible, and it alters the flavor composition. The most general matter potential Hamiltonian with NSIs is given by [284]

$$H_{\rm mat}^{\rm NSI} = \sqrt{2}G_F N_e(r) \begin{pmatrix} 1+\epsilon_{ee} & \epsilon_{e\mu} & \epsilon_{e\tau} \\ \epsilon_{e\mu}^* & \epsilon_{\mu\mu} & \epsilon_{\mu\tau} \\ \epsilon_{e\tau}^* & \epsilon_{\mu\tau}^* & \epsilon_{\tau\tau} \end{pmatrix}, \tag{9.4.1}$$

where G_F is the Fermi coupling, $N_e(r)$ is the electron density at distance r and $\epsilon_{\alpha\beta}$ are dimensionless parameters encoding the deviation from standard interactions. They are given by

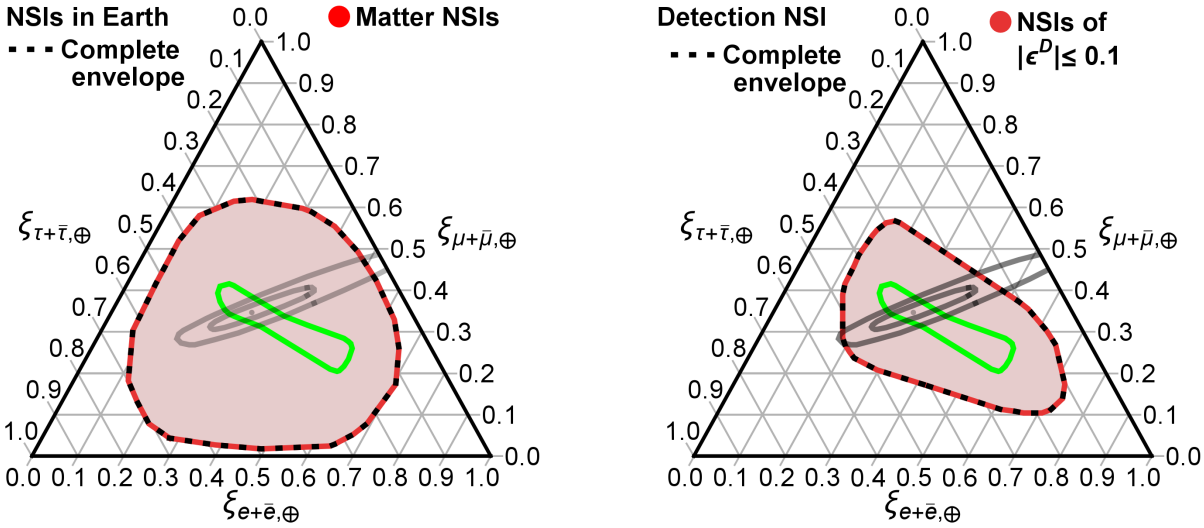

Figure 9.4: The allowed flavor composition parameter space for non-standard interactions in Earth matter (left panel) or at detection (right panel). Standard mixing is displayed by the green region, whereas the expected (1σ, 3σ) IceCube-Gen2 flavor bounds are given by the grey contours. The best-fit points are given by a dot. The "complete envelope" shows, in principle, the whole allowed parameter space, and it is shown as the dashed contours. Figure taken from Ref. [225].

$\epsilon_{\alpha\beta} = \epsilon^e_{\alpha\beta} + Y_u \epsilon^u_{\alpha\beta} + Y_d \epsilon^d_{\alpha\beta}$ [284], where $Y_u = 3.051$ ($Y_d = 3.102$) is the average up-quark/electron (down-quark/electron) ratio in the Preliminary Reference Earth Model (PREM) [285]. Here $\epsilon^e_{\alpha\beta}, \epsilon^u_{\alpha\beta}, \epsilon^d_{\alpha\beta}$ are the individual NSIs involving the electron, up-quark and down-quark, respectively. The electron NSI ($\epsilon^e_{\alpha\beta}$) is omitted since it enters the complete NSI $\epsilon_{\alpha\beta}$ and the neutrino cross section, meaning it is difficult to determine its origin. We assume the individual NSIs being complex, and the current constraints on the real part of $\epsilon^u_{\alpha\beta}$ and $\epsilon^d_{\alpha\beta}$ are summarized in Ref. [284]. We vary the real part within their 3σ allowed range and multiply it with an arbitrary complex phase factor. The flavor mixing over astrophysical distances from the source to the detector is given by Ref. [286], which we marginalize over all possible trajectories through Earth matter.

Our result is shown in Fig. 9.4, left panel. In this case, a relatively large region of the parameter space is covered, however it depends on the trajectory through Earth matter. Therefore, the allowed region has to be interpreted in a zenith-angle-dependent way, meaning one can, in principle, distinguish it from other BSM scenarios. However, we consider this beyond the scope of this work, and we recommend the reader to the original work Ref. [286]. Additional information comes from different directions since neutrinos propagating through Earth experience matter

NSIs, whereas neutrinos coming directly above the neutrino telescope would not experience this effect. Therefore, comparing the neutrino flux from different directions (such as up-going versus down-going) is vital when studying this BSM scenario.

9.4.2 Non-standard interactions at detection

The neutrino states with NSIs at detection are given by [227]

$$|\nu_\alpha^P\rangle = U_{\text{PMNS}}|\nu_i\rangle \quad \text{and} \quad \langle\nu_\beta^D| = \langle\nu_i|U_{\text{PMNS}}^\dagger(1+\epsilon^D)^\dagger\,, \tag{9.4.2}$$

where $|\nu_\alpha^P\rangle$ ($\langle\nu_\beta^D|$) represents the neutrino at production (detection), $|\nu_i\rangle$ is the mass eigenstate, U_{PMNS} is the PMNS mixing matrix and ϵ^D represents the NSIs at detection. Similar as in Subsection 9.2.2, the flavor mixing is $P_{\alpha\beta} = \sum_i |\mathcal{J}^i_{\alpha\beta}|^2$, however now with

$$\mathcal{J}^i_{\alpha\beta} = (U_{\text{PMNS}})^*_{\alpha i}(U_{\text{PMNS}})_{\beta i} + \sum_\gamma \epsilon^D_{\gamma\beta}(U_{\text{PMNS}})^*_{\alpha i}(U_{\text{PMNS}})_{\gamma i} \tag{9.4.3}$$

(note the difference in indices compared to NSIs at production). We assume $|\epsilon^D| \leq 0.1$, similar to in Section 9.2.2, and the neutrino oscillation parameters are constrained by χ^2. Our findings are given in the right panel of Fig. 9.4, showing a larger parameter space than that of production NSI. The production effect acts similar to a different initial flavor composition, and it averages out over astrophysical distances, meaning it has less impact on the flavor composition compared to detection NSI. IceCube-Gen2 can exclude 89% of the allowed parameter space.

9.5 Discrimination by flavor

Considering all BSM scenarios investigated, we compare their allowed parameter space for source (left panel), propagation (middle panel), and detection (right panel) effects in Fig. 9.5. Large deviations from the standard mixing expectation are possible, and examples include: ν_s produced at the source, dark matter interactions, effective operators and non-standard interactions in Earth matter. Note that some effects, such as non-standard interactions in Earth matter and dark matter interactions, provide arrival direction information, which can constrain the allowed parameter space further. Additionally, only the dark matter interactions scenario occupies the lower left corner of the flavor triangle.

In Tab. 9.1, we estimate the parameter space exclusion by IceCube and IceCube-Gen2 at 3σ CL. It is possible to exclude 42% of the parameter space by current constraints, however it is expected to be 96% in the future. Reading off the table, IceCube-Gen2 excludes a large fraction of the following BSM parameter spaces: ν-DM interaction, effective operator, significant

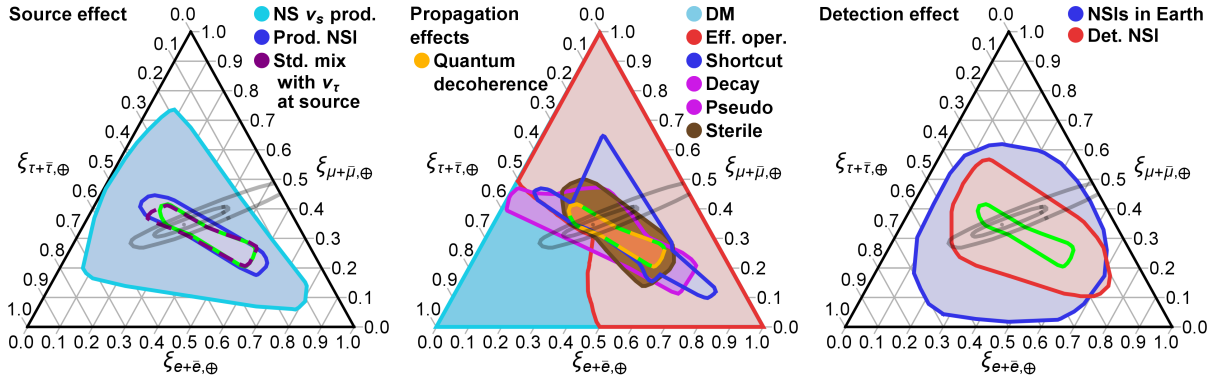

Figure 9.5: Complete flavor composition parameter space for source (left panel), propagation (middle panel), and detection BSM effects (right panel), showing the complete envelopes for all scenarios. Standard mixing is displayed by the green region, whereas the expected (1σ, 3σ) IceCube-Gen2 flavor bounds are given by the grey contours. The best-fit points are given by a dot. Figure taken from Ref. [225].

non-standard neutrino production and Earth matter NSIs. In the other end of the spectrum, scenarios with a low exclusion percentage include standard mixing, quantum decoherence and constant matter effects. As a sidenote, IceCube-Gen2 is capable to constrain the initial flavor composition considerably in the standard mixing scenario.

Disentangling the different scenarios using flavor is interesting since it tells the percentage of discriminating between two BSM parameter spaces. The parameter space overlap is presented in Tab. 9.2, where "data" represents the true scenario in nature and "theory" represents our perception of nature. It should be understood the following way with this example. Considering standard neutrino mixing to be correct, means we can compare its parameter space to that of the effective operator scenario. The discriminating percentage is 0% since the standard mixing parameter space lies within the effective operator parameter space. Considering the opposite situation, results in a discriminating percentage of 96% because the parameter space of standard mixing covers only a small fraction of the effective operator parameter space. This supports the table being asymmetric since either a large or small parameter space is predicted for the different scenarios. As seen in Tab. 9.2, it is very asymmetric. Some cases with a high discriminating factor include: standard mixing vs. ν-DM interaction, constant matter effects vs. decay, and quantum decoherence vs. effective operators[2], meaning one can, at least in principle, distinguish between them.

[2]The former cases (standard mixing, constant matter effects and quantum decoherence) represent the test scenarios, and we analyze them against the true cases (ν-DM interaction, decay and effective operator), respectively.

Scenario	Exclusion by IceCube	Exclusion by IceCube-Gen2
Complete flavor triangle	42%	96%
Standard mixing	2%	73%
Non-standard neutrino production	17%	93%
NSI at production	5%	84%
Matter effects	0%	71%
Pseudo-Dirac neutrino	14%	85%
Decay	14%	85%
Quantum decoherence	2%	73%
Sterile neutrino	10%	86%
Effective operator	36%	94%
Interaction with DM	42%	96%
Shortcut through extra dimension	11%	80%
NSI in Earth matter	30%	92%
NSI at detection	11%	89%

Table 9.1: Parameter space percentage excluable at 3σ by IceCube and IceCube-Gen2. In this table, the complete envelope acts as the parameter space, meaning not individual sub-parameter spaces have been considered. Table taken from Ref. [225].

A different visualization of Tab. 9.2 is shown in Fig. 9.6 where the discrimination percentage is given as a fraction of 100 % (colored legend on the right). Similar as in Tab. 9.2, the row gives the true scenario ("data"), and the column represents our perception of nature ("theory"). A darker (lighter) shading of blue means a higher (lower) discrimination percentage between the scenarios. Take the same example as given in the previous paragraph, namely standard neutrino mixing and the effective operator case. The former (latter) case has a small (large) parameter space, meaning it is difficult (easy) to distinguish between the scenarios when the former (latter) case is the true case. Obviously in the opposite situation, the words difficult and easy change when replacing the word true with test in the previous sentence. Therefore, standard mixing has a light row and dark column, whereas the effective operator case has a dark row and a light column. Considering half-dark squares, means partially overlapping parameter spaces. This gives a discriminating percentage of 50%, and it is independently of the choice of true scenario. This possibility can be compared to the extreme cases studied previously. No comparison is possible for the diagonal elements (symbolized by pink color and x symbol across the matrix element).

Theory → Data ↓	Standard mixing	Non-standard neutrino production	Production NSI	Matter effects	Pseudo-Dirac neutrino	Decay	Quantum decoherence	Sterile neutrino	Effective operator	Interaction with DM	Shortcut through extra dimension	NSI in Earth matter	Detection NSI
Standard mixing	...	0%	0%	73%	0%	0%	0%	0%	0%	0%	0%	0%	0%
Non-standard neutrino production	94%	...	89%	98%	73%	73%	94%	78%	45%	0%	96%	2%	49%
Production NSI	46%	0%	...	85%	0%	0%	46%	67%	0%	0%	0%	0%	0%
Matter effects	0%	0%	0%	...	0%	0%	0%	0%	0%	0%	0%	0%	0%
Pseudo-Dirac neutrino	77%	0%	58%	94%	...	0%	77%	20%	10%	0%	10%	5%	86%
Decay	77%	0%	58%	94%	0%	...	77%	20%	10%	0%	10%	5%	86%
Quantum decoherence	0%	0%	0%	73%	0%	0%	...	0%	0%	0%	0%	0%	0%
Sterile neutrino	72%	0%	48%	92%	25%	25%	72%	...	0%	0%	80%	0%	0%
Effective operator	96%	31%	92%	99%	81%	81%	96%	85%	...	0%	97%	29%	65%
Interaction with DM	97%	53%	95%	99%	87%	87%	97%	90%	32%	...	98%	52%	76%
Shortcut through extra dimension	71%	0%	46%	92%	28%	28%	71%	2%	0%	0%	...	2%	5%
NSI in Earth matter	94%	2%	89%	98%	73%	73%	94%	79%	42%	0%	96%	...	51%
Detection NSI	88%	0%	77%	97%	46%	46%	88%	57%	15%	0%	92%	2%	...

Table 9.2: Quantification of the parameter space overlap between two scenarios. Here "data" refers to the scenario implemented by Nature, and "theory" to the model to be discriminated. The numbers give the percentage of the parameter space of "data" which can be discriminated from (lies outside) the "theory" allowed parameter space in principle (for an ideal measurement). Table taken from Ref. [225].

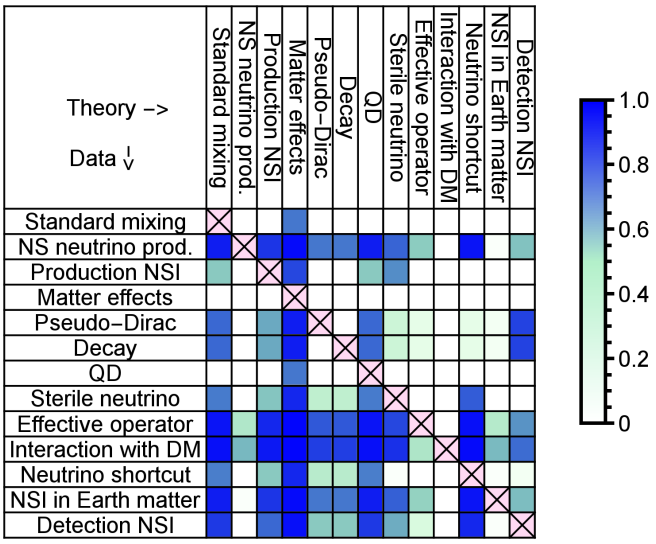

Figure 9.6: Different visualization of Tab. 9.2 with "data" referring to the scenario implemented by Nature, and "theory" to the model to be discriminated. The discrimination percentage is given as a fraction of 100%, where a darker (lighter) shading means a higher (lower) discrimination percentage between the scenarios. Abbreviations: Quantum decoherence (QD), non-standard neutrino production (NS neutrino prod.), sterile neutrino shortcut through extra dimensions (neutrino shortcut). Figure taken from Ref. [225].

9.6 Discrimination by energy dependence

It is possible for energy-dependent imprint in the neutrino flavor composition, and some specific cases reveals their BSM effect via the energy. Therefore, we study the flavor composition at three different energies [214]: 10 TeV, 100 TeV, 1000 TeV (potential capability of IceCube-Gen2), and we choose neutrino decay, quantum decoherence, effective operators and neutrino shortcuts through the extra dimension as examples. We fix all theory parameters, see Tab. 9.3 for the chosen parameter values, to investigate the energy dependence of these scenarios, and our findings for these four scenarios are presented in Fig. 9.7.

Strongest at lower energies, the effect of neutrino decay influences the flavor composition due to the low Lorentz factor, whereas standard mixing is approached for higher energies. At high energies, the effective operator case shows large flavor composition deviations, whereas for quantum decoherence, it depends on the chosen energy scaling. In our case, quantum decoherence appears at high energies. Considering the energy scaling $\sim e^{-2\kappa L E^n}$ with $n = 1$ for quantum decoherence, means effects appear at low energies. Shortcuts through extra dimensions are an example for a resonant effect present in a particular energy range, but the details (where the

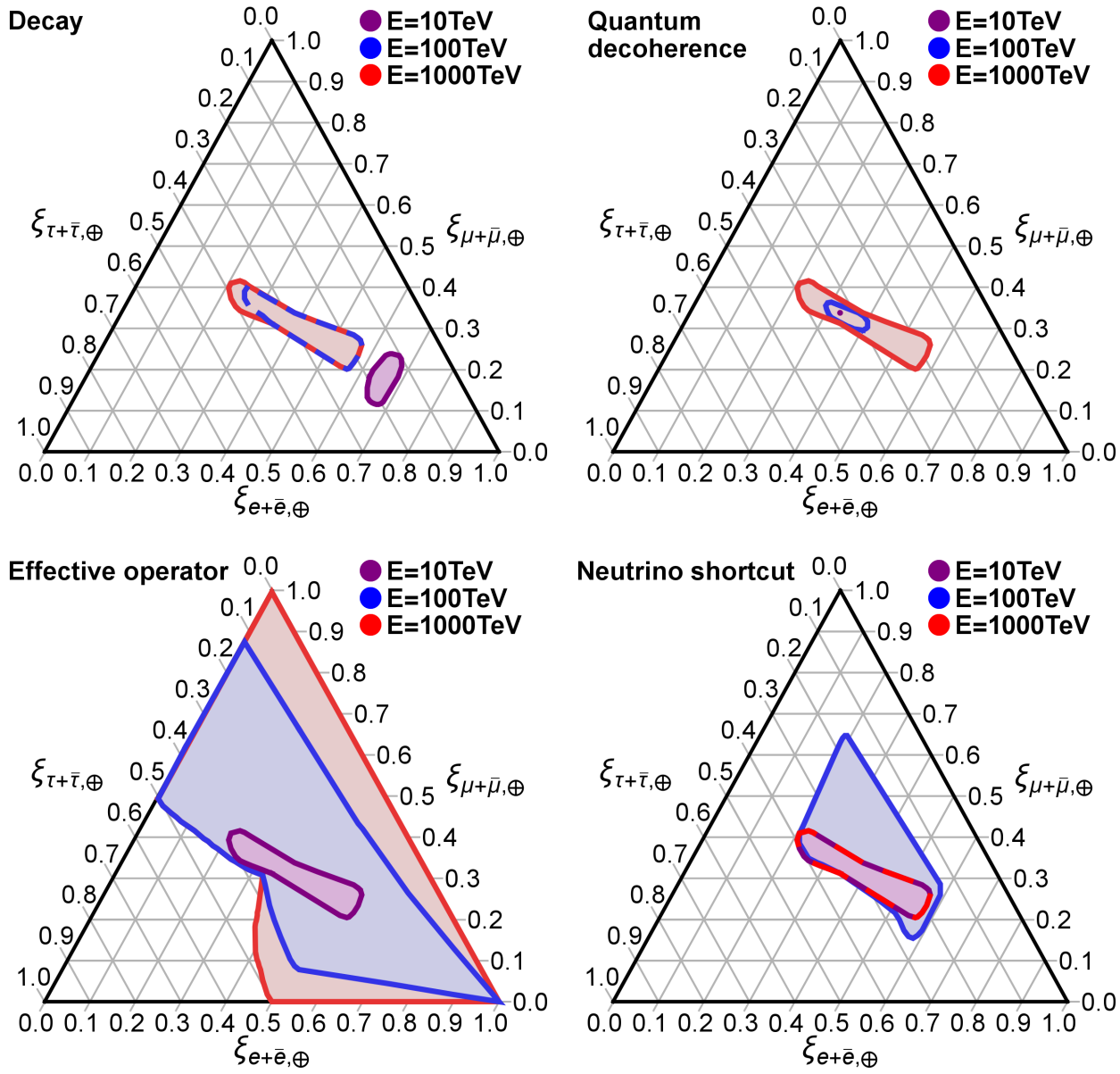

Figure 9.7: Energy-dependence of the flavor composition parameter space for four specific BSM models using the theory parameters in Tab. 9.3. Given the standard mixing parameter space in the previous figures, one notice it coincide with the red contour for neutrino decay, the red contour for quantum decoherence, the purple contour for effective operator and the red/purple contour for sterile neutrino shortcut through extra dimensions. Figure taken from Ref. [225].

Scenario	Input parameters
Decay	$\lambda_2 = \lambda_3 = 100$ s/eV, $\mathrm{Br}_{3\to1} = \mathrm{Br}_{3\to2} = 0.4$, $\mathrm{Br}_{3\to\mathrm{I}} = 0.2$ $\mathrm{Br}_{2\to1} = 0.8$, $\mathrm{Br}_{2\to\mathrm{I}} = 0.2$, $\lambda_1 = 1000$ s/eV, $\mathrm{Br}_{1\to\mathrm{I}} = 1$ $\chi^2 \leq 11.83$, $L = 100$ Mpc
Quantum decoherence	$\Gamma = 3 \cdot 10^{-39}$ GeV^2, $\Psi = 5 \cdot 10^{-39}$ GeV^2, $L = 100$ Mpc, $\chi^2 \leq 11.83$, Chosen energy scaling: $\mathrm{e}^{-2\kappa L E^{-1}}$ where $\kappa \in [\Gamma, \Psi]$
Effective operator	$O = 9 \cdot 10^{-27}$ GeV, $\Lambda = 100$ TeV, $n = 1$ operator, $\chi^2 \leq 11.83$,
Shortcut through extra dimension	$\theta_{14} = 0, \theta_{24} = \theta_{34} = 10°$, $\delta_{24}, \delta_{34} \in [0, 2\pi]$, $\chi^2 \leq 11.83$, $E_{\mathrm{res}} = 100$ TeV

Table 9.3: Input parameters used in this section to investigate the energy dependence of the four different scenarios chosen. Table taken from Ref. [225].

transitions occur) depend on the chosen model parameters. All of these examples demonstrate the additional information coming from energy-dependent effects, which, in turn, can be used to study the BSM scenarios further.

9.7 Discrimination by Glashow resonance

The Glashow resonance, $\bar{\nu}_e + e^- \to W^- \to$ (anything), at $E_\nu = m_W^2/(2m_e) \simeq 6.3$ PeV [287] is a different tool to distinguish among BSM scenarios, and the number of Glashow resonance events is an indicator for the electron antineutrino contribution to the total flux

$$G = \frac{\xi_{\bar{e},\oplus}}{\xi_{e+\bar{e},\oplus} + \xi_{\mu+\bar{\mu},\oplus} + \xi_{\tau+\bar{\tau},\oplus}} \,. \tag{9.7.1}$$

The BSM scenarios alter the neutrino flavor composition, thereby altering the allowed range of G, making a possible comparison among the standard mixing expectations and the BSM scenarios interesting. Additionally, the Glashow resonance can potentially discriminate between pp and pγ interactions, indicating the neutrino source as starburst galaxies (pp) or AGNs/GRBs (pγ), respectively [288]; for a critical discussion see Ref. [289].

We compute every scenario again with an arbitrary initial electron/muon neutrino flux and neutrino-antineutrino composition in the spirit of the work, separating the flavor mixing into two channels, one for particles and the other for antiparticles. This means we get $\xi_{\beta,\oplus}$ and $\xi_{\bar{\epsilon},\oplus}$ rather than $\xi_{\beta+\bar{\beta},\oplus}$, thereby obtaining the allowed range of G. For one scenario (NSIs in Earth matter), special attention is needed since neutrinos and antineutrinos experience different matter potentials due to the present of electrons (and not positrons) in Earth, see Ref. [286]

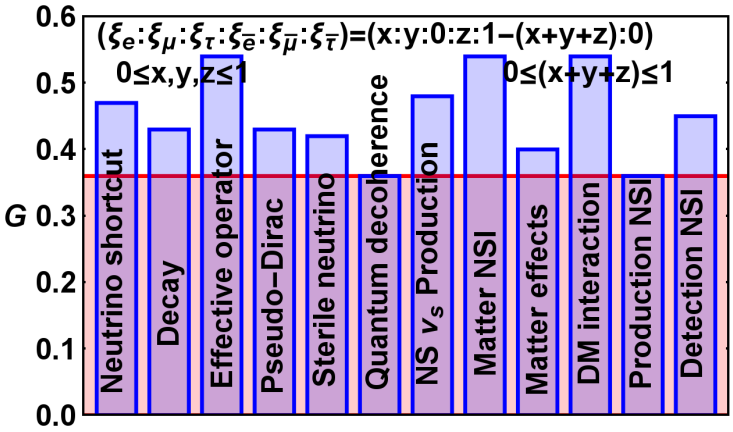

Figure 9.8: Standard mixing (red band) for the electron antineutrino fraction for an arbitrary flavor and neutrino-antineutrino composition at the source, in comparison to the ranges for different BSM scenarios and constant matter effects (bars). Figure taken from Ref. [225].

for further details. We apply the IceCube-Gen2 contours as a constraint, excluding parts of the parameter space by flavor discrimination, and thereafter obtaining the range for G. In Fig. 9.8, the allowed range of G is shown as a blue bar for the different scenarios, while the overlapping red shaded band displays the allowed range for standard mixing. There is no lower bound on G since the neutrino-antineutrino composition at the source is unknown, however a lower bound appears if this quantity is fixed. Evidently from the figure, the additional information from the Glashow resonance is limited compared to the flavor information. However, more events are predicted for some BSM scenarios, meaning it is a clear signature compared to the standard mixing prediction.

9.8 Discrimination by direct tau neutrino detection

The best known signatures of tau neutrino events are double bang [290], lollipop [291, 292] and double pulse [293], however other methods [294] to tag tau neutrinos can also be used. An immense experimental effort has gone into discovering a tau neutrino event, but no signal has been detected yet. However, as seen in Fig. 9.5, a large tau flavor composition is allowed, even after applying the IceCube-Gen2 contours as a constraint. Therefore, we present the tau flavor composition in Fig. 9.9 separately and discuss it in detail here. The allowed range of standard mixing is shown as the red band, and it has a lower bound since we consider $\xi_{\tau+\bar{\tau},\oplus}$ rather than $\xi_{\tau,\oplus}$ or $\xi_{\bar{\tau},\oplus}$. The blue bars represent the different scenarios, and there are clear deviations in

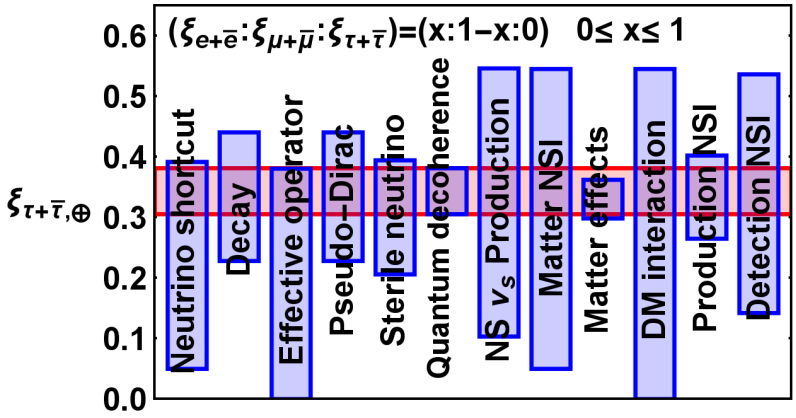

Figure 9.9: The allowed range of the tau flavor composition fro standard mixing (red band) compared to the range allowed for the other scenarios (blue bars). Due to large deviations, this additional information helps constraining the parameter space further. Figure taken from Ref. [225].

the tau flavor composition in comparison to the standard mixing predictions.

Recently, the IceCube Collaboration has presented a search for tau neutrinos among the high-energy starting track sample [295], and as a result, they expect to identify 2 tau neutrinos within 6 years of IceCube data. Non were found, however, using this expectation, we can scale the amount of possible tau neutrino events to the IceCube-Gen2 scenario. The event rate of IceCube-Gen2 is about 10 times that of IceCube for a contained event sample of 200 TeV [214], meaning 45 tau neutrino events are expected for a IceCube-Gen2 lifetime of 15 years (years needed for the IceCube-Gen2 flavor contours). This gives a relative error of 15%, meaning it is possible to measure large deviations coming from the BSM scenarios. The number of tau neutrino events from BSM scenarios are obtained using the 45 tau neutrino events expected from standard mixing and the flavor composition shown in Fig. 9.9. From this, one can constrain the flavor composition parameter space further.

9.9 Discussion and outlook

In our computation of the allowed parameter space, we derived the parameter space under certain assumptions. Considering non-standard interactions at production and/or detection, a mediator might govern this effect. For a specific mass range of this mediator, one cannot integrate it out, meaning one must take it into account in a full calculation. This could influence the neutrino flavor composition. Considering the sterile neutrino shortcut scenario, assumptions

were also made. The active-sterile mixing angle was parameterized as given in the two-flavor framework, meaning we had to assume that the sterile neutrino was mixing maximally with the electron/muon or muon/tau flavors only. To make improvements in the future, one has to start with the 4×4 Hamiltonian governing this effect, thereby omitting the assumptions made in our calculations. As a result, one obtains the general allowed neutrino flavor composition parameter space.

In this chapter, we considered the neutrino flavor composition only, however one could incorporate other observables to the analysis in order to constrain the BSM scenarios further. Introducing a ultralight scalar DM ($m_{DM} \sim 10^{-23}$ eV), neutrino-DM interactions can affect the neutrino flux by enhancing or suppressing it [296].

In our analysis, we considered the neutrino telescope IceCube/IceCube-Gen2 only. IceCube's main competitor, the KM3NeT experiment, will have a low-energy (ORCA) and a high-energy (ARCA) component, meaning they are capable of making the same research as the IceCube Collaboration. Combining the results from each neutrino telescope, means the size of the flavor contours would (probably) be reduced. Other experiments such as radio telescopes can also provide additional input to this discussion. There are several experiments which can provide additional information about a specific BSM scenario. As mentioned earlier, Fermilab want to investigate the existence of an eV sterile neutrino. Combining their results together with the IceCube-Gen2 contours, means even stronger limits on the active-sterile mixings. These examples show that there are complementary among many different experiments, which each provides information to the analysis. Therefore, combining the various limits, results in the strongest bound on BSM physics, and one can pursue a full analysis of this in the future.

Chapter 10

Conclusion and outlook

The SM of elementary particle physics is quite successful, however it cannot explain several observed phenomena such as neutrino mass, dark matter, and the baryon asymmetry. Introducing physics beyond the SM, provides possible explanations for these phenomena, and one must investigate, both theoretically and experimentally, the new physics signals in order to constrain/exclude possible BSM extensions of the SM. In this dissertation, we studied various BSM scenarios and their phenomenological consequences.

We used a model-independent and model-dependent approach to predict the active-sterile mixings of GeV sterile neutrinos in the context of neutrino mass models. The predictive power is limited in generic approaches, while the predictability increases for symmetry-generated models since it (usually) introduces less theory parameters in comparison to generic approaches. As a result, we find no preference for refind active-sterile mixing in the model-independent approach, whereas ratios among the flavored mixing elements appear in the symmetry-generated neutrino mass models. Therefore, we encourage the experimental collaborations to study both the flavored and total active-sterile mixings since the refined mixings act as a model discriminator. Futhermore, we discussed the current experimental bounds and future sensitivities to GeV sterile neutrinos since we have encounted subtleties in their interpretation, and we have highlighted the importance to compare them under equal assumptions.

A different possibility of generating neutrino masses is possible. Not necessarily experimentally accessible, sterile neutrinos with GUT scale mass can be the origin of the baryon asymmetry via thermal leptogenesis in addition to generating small neutrino masses. A resonant variant is probed by the LHC experiment, however a highly fine-tuned mass degeneracy is needed to generate successful leptogenesis. This can be compared to the conventional scenario studied in the literature, where the lightest sterile neutrino contributes to the baryon asymmetry only and its mass is near the GUT scale. This simplifies the computation considerably since there are less theory parameters involved, and we use this method. We consider structured neutrino mass models, which was not derived under the assumption of generating successful leptogenesis, and we compare the mass distribution predictions to that of the anarchy hypothesis. As a result, the structured (structureless) mass matrices generates a broad (peaked) mass distribution.

Considering this simplified calculation, one could consider a scenario with all sterile neutrinos contributing to the baryon asymmetry in the future.

The two previous scenarios concerning sterile neutrinos are originating from theoretical models, and there is no experimental evidence supporting these models. There are, however, anomalous signals in the neutrino oscillation data, suggesting the existence of eV sterile neutrinos. With this in mind, we study the introduction of eV sterile neutrinos in the context of the anarchy hypothesis. Our method is consistent with previous analyses, which shows universal active-sterile mixing distributions in the case with two sterile neutrinos. Going beyond this case, we consider a scenario with three eV sterile neutrinos, resulting in non-universal active-sterile mixing distributions when the Dirac/Majorana mass matrices are picked from a gaussian distribution. Requiring the mass matrices are given by random matrices squared, the distributions become universal again, meaning there is a clear difference between the two methods used in this scenario.

In neutrino mass modeling, we consider Abelian symmetry-generated mass matrices. These models cannot explain the control parameter value ($\epsilon \simeq 0.2$) from first principles. Considering non-Abelian symmetry groups, a complete quantizing of the full mixing matrix is possible. We applied a bottom-up reconstruction procedure to find non-Abelian finite groups $\mathcal{G}_Q$ capable of quantizing Cabbibo mixing to leading order in the quark sector. It complements "top-down" scans that do not necessarily find the simplest results due to theory biases such as restrictions on the representations of the parent symmetry or accommodating lepton mixing in addition. After all, no group has been found that can fully quantize the CKM mixing matrix given the assumptions made in these scans. Therefore, the non-Abelian groups, if natural, may make predictions that are substantially corrected via other mechanisms such as renormalization group running or specific symmetry breaking effects. Our results seem consistent with former studies of Cabbibo quark mixing, giving us candidates such as (Quasi)Dihedrals and semi-direct product structures. We reproduce Cabbibo angle within its experimental allowed range for larger groups. Therefore, we highlight the reconstruction procedure, which may be used for model-building, both within SM and BSM mixing scenarios.

In many parts of the dissertation, we consider direct detection of BSM physics. However, one can probe BSM physics indirectly via astrophysical neutrinos, and an ideal observable is the neutrino flavor composition. Considering the parameter space allowed by standard neutrino mixing in a systematic approach, we obtain a basis for which a comparison can be made when including BSM physics. Large deviations are possible for certain BSM scenarios, illustrating the potential of future neutrino telescopes such as IceCube-Gen2. It is possible for such experiments to exclude roughly 96% percentage of the allowed parameter space by measuring the flavor composition only. Other observables such as arrival direction, energy-dependence of the

flavor composition, Glashow resonance events, and expected tau neutrino events can provide additional information to the analysis, meaning one can possibly constrain the parameter space further. This shows that astrophysical neutrinos are a promising way to search for BSM physics, complementary to LHC physics, flavor physics, and dark matter searches.

The future of the Standard Model will be the same as the future of any physics theory that has been successful at predicting experimental data: it is here to stay. This is because they are useful theories in the domain they were designed for, *i.e.* in the limit where the underlying assumptions are true. Any theory that will surpass the Standard Model will have to include it as a limit for the range up to the TeV scale, as it must also explain all the experiments that have proven the Standard Model to be a useful theory. However, as time goes, additional data becomes available, resulting in a discovery of new physics, providing a future direction for particle physics, or more stringent limits on possible deviations from the SM. In turn, BSM models are supported or disproven. An example is supersymmetry, a long-standing BSM scenario, which introduces particles at the TeV scale. This is accessible for the LHC experiments, however no detection is made yet. This gives valuable input into the future, whether one wants to pursue supersymmetry further or investigate other BSM possibilities (both theoretically and experimentally).

Astroparticle physics provides additional useful information about the Standard Model and the future direction of physics. Quite recently, some new interesting (not BSM) discoveries were made. Firstly, the LIGO Collaboration announced the detection of gravitational waves [297], which opens a new way to study astrophysical sources. Secondly, the detection of gravitational waves together with an electromagnetic counterpart was announced [298]. This observation supports the multi-messenger framework, where multiple messengers (photons, neutrinos, cosmic rays and gravitational waves) provide different experimental input about the astrophysical source and its properties. The ultimate goal is an unified theory of astroparticle physics, which describes all messengers originating from a single or multiple source classes. There are attempts given in the literature (see *e.g.* [299–303]), and as more data becomes available, we are one step closer to a final theory of particle/astroparticle physics.

Therefore, discovering standard physics, which is not detected yet, or physics beyond the SM would be a major breakthrough, meaning it deserves dedicated experimental and theoretical study.

Appendix A

Symmetries for other angles

In this appendix, we study un-physical Cabibbo angles, meaning we restrict the mixing angle window to $0.7 \leq \sin\theta_C \leq 0.8$. We illustrate that our script, given appropriate inputs, can find more diverse group structures. We choose the symmetry assignment $\mathcal{G}_{u/d} \sim Z_{n/m}$ with the input $a, b \in \{0, 1...10\}$, $\mathcal{O}(T, S) \leq 4$, and $\mathcal{O}(\mathcal{G}_\mathcal{Q}) \leq 75$, and the results are found in Tab. A.1. We generate groups like S_3 and $\Sigma(2 \cdot 4^2) = ((Z_4 \times Z_4) \rtimes Z_2) \in \Sigma(2N^2)$ as expected, which are known in the literature to generate lepton mixing angles (see e.g. [304] and references therein). Additionally, Tab. A.1 also provides evidence for the plateau seen in Fig. 6.1C is an artifact of our constraint on $\sin\theta_C$. If this were relaxed, the plateau would disappear.

c	T_{diag}	S_i	GAP-ID	Group Structure	$\sin\theta_C$
$\frac{1}{4}$	[-1, 1]	[-1, 1]	[8, 3]	D_8	0.7071
$\frac{1}{4}$	[E(3)^2, 1]	[-1, 1]	[18, 3]	$Z_3 \times S_3$	0.7071
$\frac{1}{4}$	[-i, 1]	[-1, 1]	[32, 11]	$\Sigma(2 \cdot 4^2)$	0.7071
$\frac{1}{4}$	[E(3)^2, E(3)]	[-1, 1]	[6, 1]	S_3	0.7071
$\frac{1}{4}$	[-i, i]	[E(3)^2, 1]	[36, 6]	$Z_3 \times (Z_3 \rtimes Z_4)$	0.7071
$\frac{1}{4}$	[-i, i]	[E(3)^2, E(3)]	[12, 1]	$Z_3 \rtimes Z_4$	0.7071
$\frac{1}{4}$	[-i, i]	[-i, i]	[8, 4]	Q_8	0.7071
$\frac{2}{7}$	[-1, 1]	[-1, 1]	[14, 1]	D_{14}	0.7818
$\frac{2}{7}$	[-i, i]	[-1, 1]	[56, 4]	$Z_4 \times D_{14}$	0.7818
$\frac{2}{7}$	[1, -1]	[-1, 1]	[28, 3]	D_{28}	0.7818
$\frac{2}{7}$	[-i, i]	[-i, i]	[28, 1]	$Z_7 \rtimes Z_4$	0.7818

Table A.1: Flavor symmetries of U^{LO}_{CKM} using charge assignment $\mathcal{G}_{u/d} \sim Z_{n/m}$ with $\mathcal{O}(T, S) \leq 4$ and $\mathcal{O}(\mathcal{G}_F) \leq 75$. We have searched the (non-physical) range $0.7 \leq \sin\theta_C \leq 0.8$. Table taken from Ref. [180].

Appendix B

Minimization scheme

We want to find an abscissa x rather than an ordinate $f(x)$, and parabolic interpolation is effective method when locating a minimum. This is done via *Brent's method* [156] which is a minimization scheme in one dimension (multiple dimensions minimization is discussed later), and it uses the formula

$$x = b - \frac{1}{2}\frac{(b-a)^2[f(b)-f(c)] - (b-c)^2[f(b)-f(a)]}{(b-a)[f(b)-f(c)] - (b-c)[f(b)-f(a)]} \tag{B.0.1}$$

for the abscissa x that is the minimum of a parabola going through three points $f(a), f(b)$ and $f(c)$, where the triplet of points have to satisfy $a < b < c$ and $f(b) < f(a), f(c)$. This ensures the method going downhill when locating the minimum. If $f(b) > f(a)$, then the role of a and b is switched in order to be stepping downhill, whereafter the minimum is located via parabolic interpolation. A schematical diagram of the parabolic interpolation is shown in Fig. B.1, where the first interpolation through points ①, ② and ③ leads to the best fit point ④. To be acceptable, the parabolic interpolation must (i) fall within the initial interval (①, ③) and (ii) ensure convergence towards the minimum. This means the movement from the best current abscissa x has to be less than half the movement of the step before last, and the reason is not to "punish" the algorithm for a single bad step if it can make it up on the next one. Thereafter, an additional interpolation is performed through points ①, ② and ④, leading to the fit point ⑤, which is quite close to the actual minimum. This continues until the minimum is some tolerance distance *tol* away from a point already evaluated since there is no information gained. A typical ending configuration for Brent's method is a and b are $2 \cdot x \cdot tol$ apart with x (the best abscissa) and fractionally accurate to $\pm tol$. This ends the discussion of minimizing in one dimension.

Turning to multiple dimensions, we can use a one-dimensional minimization scheme and minimize along the line $\boldsymbol{n}$ by the one-dimensional method to its minimum and proceed this way in the N-dimensional space until the function stops decreasing. Various multidimensional minimization methods that consists of sequences of line minimizations only differ by how they choose the next direction $\boldsymbol{n}$ to try in order to find the local minimum in N-dimensions. A simple example

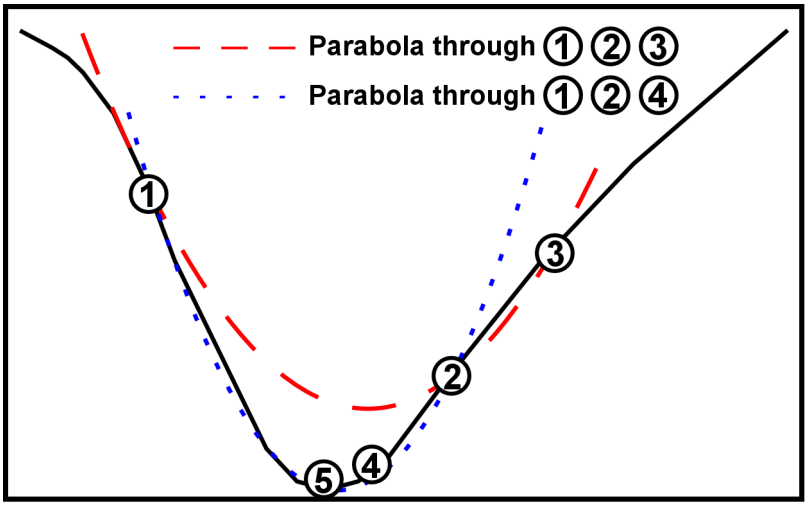

Figure B.1: Convergence to a minimum by parabolic interpolation. A parabola (dashed line) is drawn through the three original points 1,2,3 on the given function (solid line). The function is evaluated at the parabola's minimum, 4, which replaces point 3. A new parabola (dotted line) is drawn through points 1,4,2. The minimum of this parabola is at 5, which is close to the minimum of the function.

is taking the unit vectors $e_0, e_1, ..., e_{N-1}$ as a set of directions, moving along the first direction to its minimum, then along the second direction to its minimum, thereby cycling through the whole set of directions to locate the minimum. However, this method is very inefficient for some functions, as shown in a two-dimensional example in Fig. B.2 left, where the method has to go down a narrow valley, thereby requiring many cycling steps to reach the minimum. More generally, in N dimensions, many cycles through all N basis vector will be required in order to get anywhere, and it is computational expensive. Obviously what is needed is a better set of directions than the unit vectors. A set of directions where the minimization along one direction is not "spoiled" by subsequent minimization along another is said to be a conjugate set, and if you do successive line minimizations of a function along a conjugate set of directions, then you do not need to redo any of those directions when locating the minimum. A method is to come up with a set of N linearly independent, mutually conjugate directions, and this is done with *Powell's method* [157].

The procedure of acquiring a set of conjugate directions starts with initializing the set of directions $\boldsymbol{u}_i$ to the basis vectors and make use of the following sequence of steps until your function stop deceasing [157]:

- Save your starting position as P_0
- For $i = 0, ..., N-1$, move $\boldsymbol{P}_i$ to the minimum along direction $\boldsymbol{u}_i$ and call this point $\boldsymbol{P}_{i+1}$

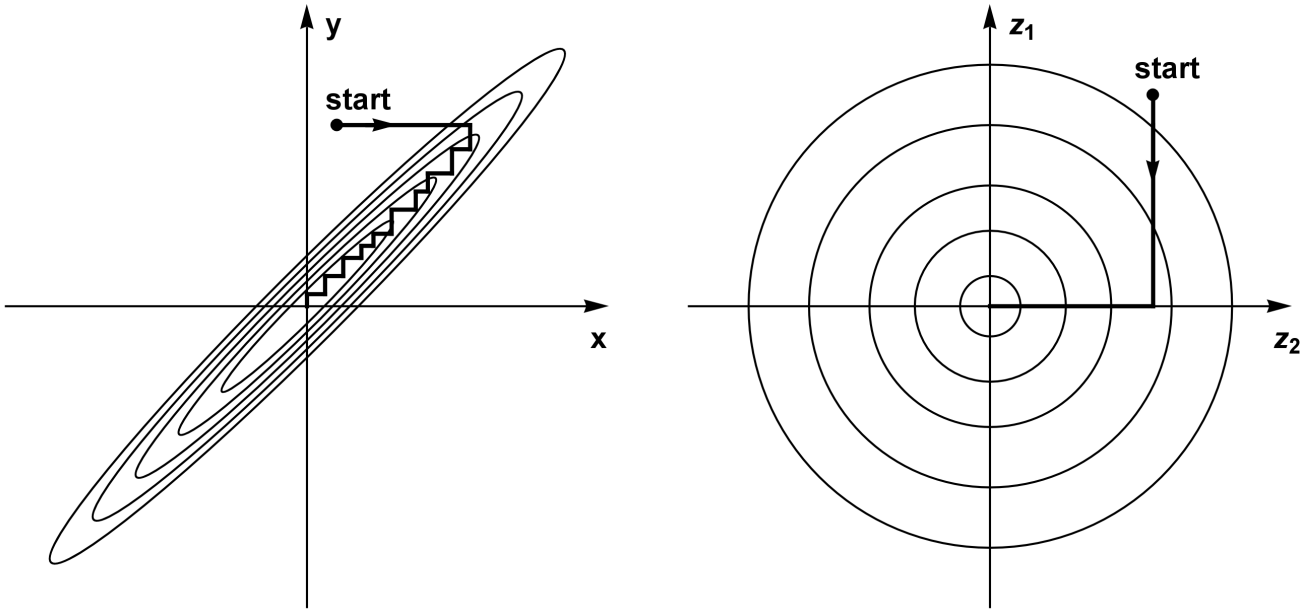

Figure B.2: (Left) Successive minimizations along coordinate directions in a long, narrow "valley" (shown as contour lines). Unless the valley is optimally oriented, this method is extremely inefficient, taking many tiny steps to get to the minimum and is computational expensive. (Right) Steepest descent method in the conjugate transformed parameter space of (Left). A step starts off in the local gradient direction, perpendicular to the contour lines, and traverses a straight line until a local minimum is reached, where the traverse is parallel to the local contour lines.

- For $i = 0, ..., N-2$, set $\boldsymbol{u}_i \leftarrow \boldsymbol{u}_{i+1}$
- Set $\boldsymbol{u}_{N-1} \leftarrow \boldsymbol{P}_N - \boldsymbol{P}_0$
- Move $\boldsymbol{P}_N$ to the minimum along direction $\boldsymbol{u}_{N-1}$ and call this point $\boldsymbol{P}_0$

Following this procedure k times will produce a set of directions $\boldsymbol{u}_i$ whose last k members are mutually conjugate. Therefore, N iterations, amounting to $N(N+1)$ line minimizations in all should locate the minimum. In Fig. B.2 right, a two-dimensional example of a minimization using conjugate sets is shown, and this minimization needs little effort to locate the minimum in the center. Therefore, this method is more efficient in localizing a minimum compared to choosing the basis unit vectors as the set of directions, which is represented by Fig. B.2 left.

Appendix C

Declaration of independent work

I declare that I have completed the thesis independently using only the aids and tools specified. I have not applied for a doctor's degree in the doctoral subject elsewhere and do not hold a corresponding doctor's degree. I have taken due note of the Faculty of Mathematics and Natural Sciences PhD Regulations, published in the Official Gazette of Humboldt-Universität zu Berlin no. 126/2014 on 18/11/2014.

Rasmus W. Rasmussen, Berlin, November 2017

Bibliography

[1] C. S. Lam, "Finite Symmetry of Leptonic Mass Matrices," *Phys. Rev.*, vol. D87, no. 1, p. 013001, 2013. ArXiv: 1208.5527.

[2] N. A. Ky, P. Quang Van, and N. T. Hong Van, "A neutrino mixing model based on an $A_4 \times Z_3 \times Z_4$ flavour symmetry," *Phys. Rev.*, vol. D94, no. 9, p. 095009, 2016. ArXiv: 1610.00304.

[3] S. Pramanick and A. Raychaudhuri, "Neutrino mass model with S_3 symmetry and seesaw interplay," *Phys. Rev.*, vol. D94, no. 11, p. 115028, 2016. ArXiv: 1609.06103.

[4] V. V. Vien, "Lepton mass and mixing in a neutrino mass model based on S_4 flavor symmetry," *Int. J. Mod. Phys.*, vol. A31, no. 09, p. 1650039, 2016. ArXiv: 1603.03933.

[5] E. Ma, "Soft $A_4 \to Z_3$ symmetry breaking and cobimaximal neutrino mixing," *Phys. Lett.*, vol. B755, pp. 348–350, 2016. ArXiv: 1601.00138.

[6] L. J. Hall, H. Murayama, and N. Weiner, "Neutrino mass anarchy," *Phys. Rev. Lett.*, vol. 84, pp. 2572–2575, 2000. ArXiv: hep-ph/9911341.

[7] N. Haba and H. Murayama, "Anarchy and hierarchy," *Phys. Rev.*, vol. D63, p. 053010, 2001. ArXiv: hep-ph/0009174.

[8] S. Weinberg, "Baryon- and Lepton-Nonconserving Processes," *Phys. Rev. Lett.*, vol. 43, pp. 1566–1570, 1979.

[9] F. Bonnet, D. Hernandez, T. Ota, and W. Winter, "Neutrino masses from higher than d=5 effective operators," *JHEP*, vol. 10, p. 076, 2009. ArXiv: 0907.3143.

[10] M. Gell-Mann, "A schematic model of baryons and mesons," *Physics Letters*, vol. 8, no. 3, pp. 214 – 215, 1964.

[11] G. Zweig, "An SU_3 model for strong interaction symmetry and its breaking; Version 1," no. CERN-TH-401, 1964.

[12] G. Zweig, "An SU_3 model for strong interaction symmetry and its breaking; Version 2," no. CERN-TH-412, p. 80 p, 1964.

[13] E. D. Bloom *et al.*, "High-Energy Inelastic e-p Scattering at 6° and 10°," *Phys. Rev. Lett.*, vol. 23, pp. 930–934, 1969.

[14] M. Breidenbach *et al.*, "Observed Behavior of Highly Inelastic Electron-Proton Scattering," *Phys. Rev. Lett.*, vol. 23, pp. 935–939, 1969.

[15] J. J. Aubert *et al.*, "Experimental Observation of a Heavy Particle J," *Phys. Rev. Lett.*, vol. 33, pp. 1404–1406, 1974.

[16] J. E. Augustin *et al.*, "Discovery of a Narrow Resonance in e^+e^- Annihilation," *Phys. Rev. Lett.*, vol. 33, pp. 1406–1408, 1974.

[17] S. W. Herb *et al.*, "Observation of a Dimuon Resonance at 9.5 GeV in 400-GeV Proton-Nucleus Collisions," *Phys. Rev. Lett.*, vol. 39, pp. 252–255, 1977.

[18] F. Abe *et al.*, "Observation of top quark production in $\bar{p}p$ collisions," *Phys. Rev. Lett.*, vol. 74, pp. 2626–2631, 1995. ArXiv: hep-ex/9503002.

[19] S. Abachi *et al.*, "Search for high mass top quark production in $p\bar{p}$ collisions at $\sqrt{s} = 1.8$ TeV," *Phys. Rev. Lett.*, vol. 74, pp. 2422–2426, 1995. ArXiv: hep-ex/9411001.

[20] K. A. Olive *et al.*, "Review of Particle Physics," *Chin. Phys.*, vol. C38, p. 090001, 2014.

[21] J. J. Thomsen, "Cathode Rays," *The London, Edinburgh, and Dublin Philosophical Magazine and Journal of Science*, vol. 44, no. 269, pp. 293–316, 1897.

[22] L. M. Brown, "The idea of the neutrino," *Physics Today*, vol. 31, no. 9, p. 23, 1978.

[23] F. Reines and C. L. Cowan, "The Neutrino," *Nature*, vol. 178, no. 4531, pp. 446–449, 1956.

[24] C. D. Anderson and S. H. Neddermeyer, "Cloud Chamber Observations of Cosmic Rays at 4300 Meters Elevation and Near Sea-Level," *Phys. Rev.*, vol. 52, pp. 263–271, 1936.

[25] S. H. Neddermeyer and C. D. Anderson, "Note on the Nature of Cosmic-Ray Particles," *Phys. Rev.*, vol. 51, pp. 884–886, 1937.

[26] G. Danby *et al.*, "Observation of High-Energy Neutrino Reactions and the Existence of Two Kinds of Neutrinos," *Phys. Rev. Lett.*, vol. 9, pp. 36–44, 1962.

[27] M. L. Perl *et al.*, "Evidence for Anomalous Lepton Production in e^+e^- Annihilation," *Phys. Rev. Lett.*, vol. 35, pp. 1489–1492, 1975.

[28] K. Kodama *et al.*, "Observation of tau neutrino interactions," *Phys. Lett.*, vol. B504, pp. 218–224, 2001. ArXiv: hep-ex/0012035.

[29] P. A. R. Ade *et al.*, "Planck 2015 results. XIII. Cosmological parameters," *Astron. Astrophys.*, vol. 594, p. A13, 2016. ArXiv: 1502.01589.

[30] S. Gardner, V. Bernard, and U. G. Meissner, "Radiative tritium beta-decay and the neutrino mass," *Phys. Lett.*, vol. B598, pp. 188–196, 2004. ArXiv: hep-ph/0407077.

[31] V. N. Aseev *et al.*, "An upper limit on electron antineutrino mass from Troitsk experiment," *Phys. Rev.*, vol. D84, p. 112003, 2011. ArXiv: 1108.5034.

[32] J. J. Gómez-Cadenas and J. Martín-Albo, "Phenomenology of neutrinoless double beta decay," *PoS*, vol. GSSI14, p. 004, 2015. ArXiv: 1502.00581.

[33] M. Agostini *et al.*, "Results on Neutrinoless Double-β Decay of ^{76}Ge from Phase I of the GERDA Experiment," *Phys. Rev. Lett.*, vol. 111, no. 12, p. 122503, 2013. ArXiv: 1307.4720.

[34] P. Minkowski, "$\mu \to e\gamma$ at a rate of one out of 109 muon decays?," *Physics Letters B*, vol. 67, pp. 421 – 428, 1977.

[35] M. Gell-Mann, P. Ramond, and R. Slansky, "Complex Spinors and Unified Theories," *Conf. Proc.*, vol. C790927, pp. 315–321, 1979. ArXiv: 1306.4669.

[36] T. Yanagida, "Horizontal Symmetry and Masses of Neutrinos," *Progress of Theoretical Physics*, vol. 64, pp. 1103–1105, 1980.

[37] R. N. Mohapatra and G. Senjanovic, "Neutrino Mass and Spontaneous Parity Nonconservation," *Phys. Rev. Lett.*, vol. 44, pp. 912–915, 1980.

[38] J. Schechter and J. W. F. Valle, "Neutrino masses in SU(2) $\bigotimes$ U(1) theories," *Phys. Rev. D*, vol. 22, pp. 2227–2235, 1980.

[39] M. Magg and C. Wetterich, "Neutrino Mass Problem and Gauge Hierarchy," *Phys. Lett.*, vol. 94B, pp. 61–64, 1980.

[40] G. Lazarides, Q. Shafi, and C. Wetterich, "Proton Lifetime and Fermion Masses in an SO(10) Model," *Nucl. Phys.*, vol. B181, pp. 287–300, 1981.

[41] R. N. Mohapatra and G. Senjanovic, "Neutrino Masses and Mixings in Gauge Models with Spontaneous Parity Violation," *Phys. Rev.*, vol. D23, p. 165, 1981.

[42] E. Ma and U. Sarkar, "Neutrino masses and leptogenesis with heavy Higgs triplets," *Phys. Rev. Lett.*, vol. 80, pp. 5716–5719, 1998. ArXiv: hep-ph/9802445.

[43] R. Foot, H. Lew, X. G. He, and G. C. Joshi, "See-saw neutrino masses induced by a triplet of leptons," *Zeitschrift für Physik C Particles and Fields*, vol. 44, no. 3, pp. 441–444, 1989.

[44] E. Ma, "Pathways to naturally small neutrino masses," *Phys. Rev. Lett.*, vol. 81, pp. 1171–1174, 1998. ArXiv: hep-ph/9805219.

[45] R. N. Mohapatra, "Mechanism for Understanding Small Neutrino Mass in Superstring Theories," *Phys. Rev. Lett.*, vol. 56, pp. 561–563, 1986.

[46] R. N. Mohapatra and J. W. F. Valle, "Neutrino Mass and Baryon Number Nonconservation in Superstring Models," *Phys. Rev.*, vol. D34, p. 1642, 1986.

[47] L. J. Hall and M. Suzuki, "Explicit R-parity breaking in supersymmetric models," *Nuclear Physics B*, vol. 231, no. 3, pp. 419 – 444, 1984.

[48] Y. Grossman and H. E. Haber, "Sneutrino mixing phenomena," *Phys. Rev. Lett.*, vol. 78, pp. 3438–3441, 1997. ArXiv: hep-ph/9702421.

[49] M. A. Diaz, J. C. Romao, and J. W. F. Valle, "Minimal supergravity with R-parity breaking," *Nucl. Phys.*, vol. B524, pp. 23–40, 1998. ArXiv: hep-ph/9706315.

[50] A. Abada and M. Losada, "Constraints on a general three generation neutrino mass matrix from neutrino data: Application to the MSSM with R-parity violation," *Nucl. Phys.*, vol. B585, pp. 45–78, 2000. ArXiv: hep-ph/9908352.

[51] M. Hirsch *et al.*, "Neutrino masses and mixings from supersymmetry with bilinear R parity violation: A Theory for solar and atmospheric neutrino oscillations," *Phys. Rev.*, vol. D62, p. 113008, 2000. ArXiv: hep-ph/0004115.

[52] A. Dedes, S. Rimmer, and J. Rosiek, "Neutrino masses in the lepton number violating MSSM," *JHEP*, vol. 08, p. 005, 2006. ArXiv: hep-ph/0603225.

[53] H. K. Dreiner *et al.*, "Neutrino masses and mixings in the baryon triality constrained minimal supersymmetric standard model," *Phys. Rev.*, vol. D84, p. 113005, 2011. ArXiv: 1106.4338.

[54] R. N. Mohapatra and G. Senjanovic, "Neutrino Mass and Spontaneous Parity Violation," *Phys. Rev. Lett.*, vol. 44, p. 912, 1980.

[55] G. B. Gelmini and M. Roncadelli, "Left-Handed Neutrino Mass Scale and Spontaneously Broken Lepton Number," *Phys. Lett.*, vol. 99B, pp. 411–415, 1981.

[56] T. P. Cheng and L.-F. Li, "Neutrino Masses, Mixings and Oscillations in SU(2) x U(1) Models of Electroweak Interactions," *Phys. Rev.*, vol. D22, p. 2860, 1980.

[57] A. Zee, "A Theory of Lepton Number Violation, Neutrino Majorana Mass, and Oscillation," *Phys. Lett.*, vol. 93B, p. 389, 1980.

[58] K. S. Babu, "Model of 'Calculable' Majorana Neutrino Masses," *Phys. Lett.*, vol. B203, pp. 132–136, 1988.

[59] N. G. Deshpande, J. F. Gunion, B. Kayser, and F. I. Olness, "Left-right symmetric electroweak models with triplet Higgs," *Phys. Rev.*, vol. D44, pp. 837–858, 1991.

[60] N. Arkani-Hamed *et al.*, "Neutrino masses from large extra dimensions," *Phys. Rev.*, vol. D65, p. 024032, 2001. ArXiv: hep-ph/9811448.

[61] G. R. Dvali and A. Yu. Smirnov, "Probing large extra dimensions with neutrinos," *Nucl. Phys.*, vol. B563, pp. 63–81, 1999. ArXiv: hep-ph/9904211.

[62] R. N. Mohapatra *et al.*, "Neutrino masses and oscillations in models with large extra dimensions," *Phys. Lett.*, vol. B466, pp. 115–121, 1999. ArXiv: hep-ph/9907520.

[63] R. Barbieri, P. Creminelli, and A. Strumia, "Neutrino oscillations from large extra dimensions," *Nucl. Phys.*, vol. B585, pp. 28–44, 2000. ArXiv: hep-ph/0002199.

[64] M. Drewes, "The Phenomenology of Right Handed Neutrinos," *Int. J. Mod. Phys.*, vol. E22, p. 1330019, 2013. ArXiv: 1303.6912.

[65] K. N. Abazajian *et al.*, "Light Sterile Neutrinos: A White Paper," 2012. ArXiv: 1204.5379.

[66] R. Barbier *et al.*, "R-parity violating supersymmetry," *Phys. Rept.*, vol. 420, pp. 1–202, 2005. ArXiv: hep-ph/0406039.

[67] Y. Cai, J. Herrero-García, M. A. Schmidt, A. Vicente, and R. R. Volkas, "From the trees to the forest: a review of radiative neutrino mass models," 2017. ArXiv: 1706.08524.

[68] I. Esteban *et al.*, "Updated fit to three neutrino mixing: exploring the accelerator-reactor complementarity," *JHEP*, vol. 01, p. 087, 2017. ArXiv: 1611.01514.

[69] S. Parke and M. Ross-Lonergan, "Unitarity and the three flavor neutrino mixing matrix," *Phys. Rev.*, vol. D93, no. 11, p. 113009, 2016. ArXiv: 1508.05095.

[70] S. P. Mikheyev and A. Y. Smirnov, "Resonance enhancement of oscillations in matter and solar neutrino spectroscopy," *Soviet Journal of Nuclear Physics*, vol. 42, pp. 1441–1448, 1985.

[71] L. Wolfenstein, "Neutrino oscillations in matter," *Phys. Rev. D*, vol. 17, pp. 2369–2374, 1978.

[72] L. Wolfenstein, "Neutrino oscillations and stellar collapse," *Phys. Rev. D*, vol. 20, pp. 2634–2635, 1979.

[73] J. Charles *et al.*, "Current status of the Standard Model CKM fit and constraints on $\Delta F = 2$ New Physics," *Phys. Rev.*, vol. D91, no. 7, p. 073007, 2015. ArXiv: 1501.05013.

[74] D. J. Gross and F. Wilczek, "Ultraviolet Behavior of Non-Abelian Gauge Theories," *Phys. Rev. Lett.*, vol. 30, pp. 1343–1346, 1973.

[75] H. D. Politzer, "Reliable Perturbative Results for Strong Interactions?," *Phys. Rev. Lett.*, vol. 30, pp. 1346–1349, 1973.

[76] H. Ishimori, Kobayashi, *et al.*, "Non-Abelian Discrete Symmetries in Particle Physics," *Prog. Theor. Phys. Suppl.*, vol. 183, pp. 1–163, 2010. ArXiv: 1003.3552.

[77] Z.-z. Xing and Z.-h. Zhao, "A review of μ-τ flavor symmetry in neutrino physics," *Rept. Prog. Phys.*, vol. 79, no. 7, p. 076201, 2016. ArXiv: 1512.04207.

[78] C. Froggatt and H. Nielsen, "Hierarchy of quark masses, cabibbo angles and CP-violation," *Nuclear Physics B*, vol. 147, pp. 277 – 298, 1979.

[79] S. King, "Talk at FLASY 2015," *Colima, Mexico.*, 2015.

[80] F. Plentinger *et al.*, "Systematic parameter space search of extended quark-lepton complementarity," *Nucl. Phys.*, vol. B791, pp. 60–92, 2008. ArXiv: hep-ph/0612169.

[81] X. Lu and H. Murayama, "Neutrino Mass Anarchy and the Universe," *JHEP*, vol. 08, p. 101, 2014. ArXiv: 1405.0547.

[82] K. S. Jeong *et al.*, "Degenerate spectrum in the neutrino mass anarchy with Wishart matrices and implications for $0\nu\beta\beta$ and $\delta_{\rm CP}$," *Phys. Rev.*, vol. D91, no. 11, p. 113010, 2015. ArXiv: 1412.4061.

[83] E. Ma and G. Rajasekaran, "Softly broken A(4) symmetry for nearly degenerate neutrino masses," *Phys. Rev.*, vol. D64, p. 113012, 2001. ArXiv: hep-ph/0106291.

[84] K. S. Babu, E. Ma, and J. W. F. Valle, "Underlying A(4) symmetry for the neutrino mass matrix and the quark mixing matrix," *Phys. Lett.*, vol. B552, pp. 207–213, 2003. ArXiv: hep-ph/0206292.

[85] G. Altarelli and F. Feruglio, "Tri-bimaximal neutrino mixing from discrete symmetry in extra dimensions," *Nucl. Phys.*, vol. B720, pp. 64–88, 2005. ArXIv: hep-ph/0504165.

[86] G. Altarelli and F. Feruglio, "Tri-bimaximal neutrino mixing, A(4) and the modular symmetry," *Nucl. Phys.*, vol. B741, pp. 215–235, 2006. ArXiv: hep-ph/0512103.

[87] I. de Medeiros Varzielas, S. F. King, and G. G. Ross, "Tri-bimaximal neutrino mixing from discrete subgroups of SU(3) and SO(3) family symmetry," *Phys. Lett.*, vol. B644, pp. 153–157, 2007. ArXiv: hep-ph/0512313.

[88] K. M. Parattu and A. Wingerter, "Tribimaximal Mixing From Small Groups," *Phys. Rev.*, vol. D84, p. 013011, 2011. ArXiv: 1012.2842.

[89] I. de Medeiros Varzielas and D. Pidt, "UV completions of flavour models and large θ_{13}," *JHEP*, vol. 03, p. 065, 2013. ArXiv: 1211.5370.

[90] H. Ishimori and E. Ma, "New Simple A_4 Neutrino Model for Nonzero θ_{13} and Large δ_{CP}," *Phys. Rev.*, vol. D86, p. 045030, 2012. ArXiv: 1205.0075.

[91] Y. H. Ahn, S. K. Kang, and C. S. Kim, "Spontaneous CP Violation in A_4 Flavor Symmetry and Leptogenesis," *Phys. Rev.*, vol. D87, no. 11, p. 113012, 2013. ArXiv: 1304.0921.

[92] N. Memenga, W. Rodejohann, and H. Zhang, "A_4 flavor symmetry model for Dirac neutrinos and sizable U_{e3}," *Phys. Rev.*, vol. D87, no. 5, p. 053021, 2013. ArXiv: 1301.2963.

[93] S. Bhattacharya, E. Ma, A. Natale, and A. Rashed, "Radiative Scaling Neutrino Mass with A_4 Symmetry," *Phys. Rev.*, vol. D87, p. 097301, 2013. ArXIv: 1302.6266.

[94] P. M. Ferreira, L. Lavoura, and P. O. Ludl, "A new A_4 model for lepton mixing," *Phys. Lett.*, vol. B726, pp. 767–772, 2013. ArXiv: 1306.1500.

[95] R. Gonzalez Felipe, H. Serodio, and J. P. Silva, "Neutrino masses and mixing in A4 models with three Higgs doublets," *Phys. Rev.*, vol. D88, no. 1, p. 015015, 2013. ArXiv: 1304.3468.

[96] A. E. C. Hernandez *et al.*, "Lepton masses and mixings in an A_4 multi-Higgs model with a radiative seesaw mechanism," *Phys. Rev.*, vol. D88, no. 7, p. 076014, 2013. ArXiv: 1307.6499.

[97] S. F. King *et al.*, "Quark-Lepton Mass Relation in a Realistic A_4 Extension of the Standard Model," *Phys. Lett.*, vol. B724, pp. 68–72, 2013. 1301.7065.

[98] S. Morisi *et al.*, "Neutrino mixing with revamped A_4 flavor symmetry," *Phys. Rev.*, vol. D88, no. 1, p. 016003, 2013. ArXiv: 1305.6774.

[99] S. Morisi *et al.*, "Quark-Lepton Mass Relation and CKM mixing in an A4 Extension of the Minimal Supersymmetric Standard Model," *Phys. Rev.*, vol. D88, p. 036001, 2013. ArXiv: 1303.4394.

[100] R. González Felipe *et al.*, "Models with three Higgs doublets in the triplet representations of A_4 or S_4," *Phys. Rev.*, vol. D87, no. 5, p. 055010, 2013. ArXiv: 1302.0861.

[101] M. D. Campos *et al.*, "Fermion masses and mixings in an $SU(5)$ grand unified model with an extra flavor symmetry," *Phys. Rev.*, vol. D90, no. 1, p. 016006, 2014. ArXiv: 1403.2525.

[102] A. E. C. Hernandez and R. Martinez, "A predictive 3-3-1 model with A_4 flavor symmetry," *Nucl. Phys.*, vol. B905, pp. 337–358, 2016. ArXiv: 1501.05937.

[103] R. de Adelhart Toorop, F. Feruglio, and C. Hagedorn, "Finite Modular Groups and Lepton Mixing," *Nucl. Phys.*, vol. B858, pp. 437–467, 2012. ArXiv: 1112.1340.

[104] M. Holthausen, K. S. Lim, and M. Lindner, "Lepton Mixing Patterns from a Scan of Finite Discrete Groups," *Phys. Lett.*, vol. B721, pp. 61–67, 2013. ArXiv: 1212.2411.

[105] S. F. King, T. Neder, and A. J. Stuart, "Lepton mixing predictions from $\Delta(6n^2)$ family Symmetry," *Phys. Lett.*, vol. B726, pp. 312–315, 2013. ArXiv: 1305.3200.

[106] L. Lavoura and P. O. Ludl, "Residual $\mathbb{Z}_2 \times \mathbb{Z}_2$ symmetries and lepton mixing," *Phys. Lett.*, vol. B731, pp. 331–336, 2014. ArXiv: 1401.5036.

[107] A. S. Joshipura and K. M. Patel, "A massless neutrino and lepton mixing patterns from finite discrete subgroups of U(3)," *JHEP*, vol. 04, p. 009, 2014. ArXiv: 1401.6397.

[108] A. S. Joshipura and K. M. Patel, "Discrete flavor symmetries for degenerate solar neutrino pair and their predictions," *Phys. Rev.*, vol. D90, no. 3, p. 036005, 2014. ArXiv: 1405.6106.

[109] S. F. King and P. O. Ludl, "Direct and Semi-Direct Approaches to Lepton Mixing with a Massless Neutrino," *JHEP*, vol. 06, p. 147, 2016. ArXiv: 1605.01683.

[110] R. M. Fonseca and W. Grimus, "Classification of lepton mixing matrices from finite residual symmetries," *JHEP*, vol. 09, p. 033, 2014. ArXiv: 1405.3678.

[111] J. Talbert, "[Re]constructing Finite Flavour Groups: Horizontal Symmetry Scans from the Bottom-Up," *JHEP*, vol. 12, p. 058, 2014. ArXiv: 1409.7310.

[112] A. de Gouvea and H. Murayama, "Neutrino Mixing Anarchy: Alive and Kicking," *Phys. Lett.*, vol. B747, pp. 479–483, 2015. ArXiv: 1204.1249.

[113] M. Holthausen and K. S. Lim, "Quark and Leptonic Mixing Patterns from the Breakdown of a Common Discrete Flavor Symmetry," *Phys. Rev.*, vol. D88, p. 033018, 2013. ArXiv: 1306.4356.

[114] S.-F. Ge, "Unifying Residual $\mathbb{Z}_2^{23} \otimes \mathbb{Z}_2^{12}$ Symmetries and Quark-Lepton Complementarity," 2014. ArXiv: 1406.1985.

[115] H. Ishimori, S. F. King, H. Okada, and M. Tanimoto, "Quark mixing from $\Delta(6\mathrm{N}^2)$ family symmetry," *Phys. Lett.*, vol. B743, pp. 172–179, 2015. ArXiv: 1411.5845.

[116] C.-Y. Yao and G.-J. Ding, "Lepton and Quark Mixing Patterns from Finite Flavor Symmetries," *Phys. Rev.*, vol. D92, no. 9, p. 096010, 2015. ArXiv: 1505.03798.

[117] A. Blum *et al.*, "Fermion Masses and Mixings from Dihedral Flavor Symmetries with Preserved Subgroups," *Phys. Rev.*, vol. D77, p. 076004, 2008. ArXiv: 0709.3450.

[118] C. Hagedorn and D. Meloni, "D14 - A Common Origin of the Cabibbo Angle and the Lepton Mixing Angle θ_{13}," *Nucl. Phys.*, vol. B862, pp. 691–709, 2012. ArXiv: 1204.0715.

[119] S. R. J. Wysozka *et al.*, "Scale dependence of the quark masses and mixings: Leading order," *Phys. Rev.*, vol. D66, p. 116007, 2002. ArXiv: hep-ph/0206243.

[120] G. Ross and M. Serna, "Unification and fermion mass structure," *Phys. Lett.*, vol. B664, pp. 97–102, 2008. ArXiv: 0704.1248.

[121] I. de Medeiros Varzielas, G. G. Ross, and M. Serna, "Quasi-degenerate neutrinos and tri-bi-maximal mixing," *Phys. Rev.*, vol. D80, p. 073002, 2009. ArXiv: 0811.2226.

[122] D. Aristizabal Sierra, I. de Medeiros Varzielas, and E. Houet, "Eigenvector-based approach to neutrino mixing," *Phys. Rev.*, vol. D87, no. 9, p. 093009, 2013. ArXiv: 1302.6499.

[123] L. J. Hall and G. G. Ross, "Discrete Symmetries and Neutrino Mass Perturbations for θ_{13}," *JHEP*, vol. 11, p. 091, 2013. ArXiv: 1303.6962.

[124] D. Aristizabal Sierra and I. de Medeiros Varzielas, "Reactor mixing angle from hybrid neutrino masses," *JHEP*, vol. 07, p. 042, 2014. ArXiv: 1404.2529.

[125] A. de Gouvea and H. Murayama, "Statistical test of anarchy," *Phys. Lett.*, vol. B573, pp. 94–100, 2003. ArXiv: hep-ph/0301050.

[126] L. Canetti *et al.*, "Dark Matter, Baryogenesis and Neutrino Oscillations from Right Handed Neutrinos," *Phys. Rev.*, vol. D87, p. 093006, 2013. ArXiv: 1208.4607.

[127] T. Asaka, S. Blanchet, and M. Shaposhnikov, "The nuMSM, dark matter and neutrino masses," *Phys. Lett.*, vol. B631, pp. 151–156, 2005. ArXiv: hep-ph/0503065.

[128] T. Asaka and M. Shaposhnikov, "The nuMSM, dark matter and baryon asymmetry of the universe," *Phys. Lett.*, vol. B620, pp. 17–26, 2005. ArXiv: hep-ph/0505013.

[129] S. Tremaine and J. E. Gunn, "Dynamical Role of Light Neutral Leptons in Cosmology," *Phys. Rev. Lett.*, vol. 42, pp. 407–410, 1979.

[130] D. Gorbunov and M. Shaposhnikov, "How to find neutral leptons of the νMSM?," *JHEP*, vol. 10, p. 015, 2007. ArXiv: 0705.1729.

[131] D. Kirkman *et al.*, "The Cosmological baryon density from the deuterium to hydrogen ratio towards QSO absorption systems: D/H towards Q1243+3047," *Astrophys. J. Suppl.*, vol. 149, p. 1, 2003. ArXiv: astro-ph/0302006.

[132] E. Komatsu *et al.*, "Seven-year Wilkinson Microwave Anisotropy Probe (WMAP) Observations: Cosmological Interpretation," *Astrophys. Jour. Supp. Series*, vol. 192, no. 2, p. 18, 2011.

[133] F. Bjorkeroth, F. J. de Anda, I. de Medeiros Varzielas, and S. F. King, "Leptogenesis in a $\Delta(27) \times SO(10)$ SUSY GUT," *JHEP*, vol. 01, p. 077, 2017. ArXiv: 1609.05837.

[134] A. Boyarsky *et al.*, "The Role of sterile neutrinos in cosmology and astrophysics," *Ann. Rev. Nucl. Part. Sci.*, vol. 59, pp. 191–214, 2009. ArXiv: 0901.0011.

[135] M. Drewes and B. Garbrecht, "Leptogenesis from a GeV Seesaw without Mass Degeneracy," *JHEP*, vol. 03, p. 096, 2013.

[136] R. Jacobsson, "Talk at XXVII International Conference on Neutrino Physics and Astrophysics," *CERN, Schwitzerland*, 2016.

[137] F. F. Deppisch, P. S. Bhupal Dev, and A. Pilaftsis, "Neutrinos and Collider Physics," *New J. Phys.*, vol. 17, no. 7, p. 075019, 2015. ArXiv: 1502.06541.

[138] J. C. Helo, M. Hirsch, and S. Kovalenko, "Heavy neutrino searches at the LHC with displaced vertices," *Phys. Rev.*, vol. D89, p. 073005, 2014. ArxXiv: 1312.2900.

[139] A. J. Bevan *et al.*, "The Physics of the B Factories," *Eur. Phys. J.*, vol. C74, p. 3026, 2014.

[140] B. Adeva *et al.*, "Roadmap for selected key measurements of LHCb," 2009. ArXiv: 0912.4179.

[141] T. A. Collaboration, "The ATLAS Experiment at the CERN Large Hadron Collider," *Journal of Instrumentation*, vol. 3, no. 08, p. S08003, 2008.

[142] T. C. Collaboration, "The CMS experiment at the CERN LHC," *Journal of Instrumentation*, vol. 3, no. 08, p. S08004, 2008.

[143] M. Anelli *et al.*, "A facility to Search for Hidden Particles (SHiP) at the CERN SPS," 2015. ArXiv: 1504.04956.

[144] S. Alekhin *et al.*, "A facility to Search for Hidden Particles at the CERN SPS: the SHiP physics case," *Rept. Prog. Phys.*, vol. 79, no. 12, p. 124201, 2016. ArXiv: 1504.04855.

[145] C. Adams *et al.*, "The Long-Baseline Neutrino Experiment: Exploring Fundamental Symmetries of the Universe," 2013. ArXiv: 1307.7335.

[146] R. Acciarri *et al.*, "Long-Baseline Neutrino Facility (LBNF) and Deep Underground Neutrino Experiment (DUNE)," 2015. ArXiv: 1512.06148.

[147] G. Aarons *et al.*, "International Linear Collider Reference Design Report Volume 2: Physics at the ILC," 2007. ArXiv: 0709.1893.

[148] A. Blondel, E. Graverini, N. Serra, and M. Shaposhnikov, "Search for Heavy Right Handed Neutrinos at the FCC-ee," 2014. ArXiv: 1411.5230.

[149] S. Antusch, E. Cazzato, and O. Fischer, "Displaced vertex searches for sterile neutrinos at future lepton colliders," *JHEP*, vol. 12, p. 007, 2016. ArXiv: 1604.02420.

[150] L. Canetti and M. Shaposhnikov, "Baryon Asymmetry of the Universe in the NuMSM," *JCAP*, vol. 1009, p. 001, 2010. ArXiv: 1006.0133.

[151] J. Dorenbosch *et al.*, "A search for decays of heavy neutrinos in the mass range 0.5–2.8 gev," *Physics Letters B*, vol. 166, no. 4, pp. 473 – 478, 1986.

[152] G. Bernardi *et al.*, "Further limits on heavy neutrino couplings," *Physics Letters B*, vol. 203, no. 3, pp. 332 – 334, 1988.

[153] J. A. Casas and A. Ibarra, "Oscillating neutrinos and $\mu \to e\gamma$," *Nucl. Phys.*, vol. B618, pp. 171–204, 2001. ArXiv: hep-ph/0103065.

[154] M. Drewes and B. Garbrecht, "Combining experimental and cosmological constraints on heavy neutrinos," *Nucl. Phys.*, vol. B921, pp. 250–315, 2017. ArXiv: 1502.00477.

[155] W. Rodejohann and X.-J. Xu, "Robustness of neutrino mass matrix predictions," *Nucl. Phys.*, vol. B899, pp. 463–475, 2015. ArXiv: 1508.06063.

[156] R. P. Brent, "Algorithms for minimization without derivatives," 1973.

[157] M. J. D. Powell, "An efficient method for finding the minimum of a function of several variables without calculating derivatives," *The Computer Journal*, vol. 7, pp. 155–162, 1964.

[158] R. Fletcher, "Function minimization without evaluating derivatives," *Computer Journal*, vol. 8, pp. 33–41, 1965.

[159] T. Asaka and T. Tsuyuki, "Perturbativity in the seesaw mechanism," *Phys. Lett.*, vol. B753, pp. 147–149, 2016. ArXiv: 1509.02678.

[160] DELPHI, "Search for neutral heavy leptons produced in Z decays," *Zeitschrift für Physik C Particles and Fields*, vol. 74, pp. 57–71, 1997.

[161] R. W. Rasmussen and W. Winter, "Perspectives for tests of neutrino mass generation at the GeV scale: Experimental reach versus theoretical predictions," *Phys. Rev.*, vol. D94, no. 7, p. 073004, 2016. ArXiv: 1607.07880.

[162] F. Plentinger *et al.*, "The Seesaw mechanism in quark-lepton complementarity," *Phys. Rev.*, vol. D76, p. 113003, 2007. ArXiv: 0707.2379.

[163] F. Plentinger *et al.*, "Group Space Scan of Flavor Symmetries for Nearly Tribimaximal Lepton Mixing," *JHEP*, vol. 04, p. 077, 2008. ArXiv: 0802.1718.

[164] D. Gorbunov and A. Panin, "On the minimal active-sterile neutrino mixing in seesaw type I mechanism with sterile neutrinos at GeV scale," *Phys. Rev.*, vol. D89, no. 1, p. 017302, 2014. ArXiv: 1312.2887.

[165] H. Lacker, "private communication," 2015.

[166] G. Jungman, M. Kamionkowski, and K. Griest, "Supersymmetric dark matter," *Phys. Rept.*, vol. 267, pp. 195–373, 1996. ArXiv: hep-ph/9506380.

[167] G. Arcadi *et al.*, "The Waning of the WIMP? A Review of Models, Searches, and Constraints," 2017. ArXiv: 1703.07364.

[168] Peccei, R. D. and Quinn, Helen R., "CP conservation in the presence of pseudoparticles," *Phys. Rev. Lett.*, vol. 38, pp. 1440–1443, 1977.

[169] Peccei, R. D. and Quinn, Helen R., "Constraints imposed by CP conservation in the presence of pseudoparticles," *Phys. Rev. D*, vol. 16, pp. 1791–1797, 1977.

[170] J. E. Kim and G. Carosi, "Axions and the Strong CP Problem," *Rev. Mod. Phys.*, vol. 82, pp. 557–602, 2010. ArXiv: 0807.3125.

[171] R. Acciarri *et al.*, "Long-Baseline Neutrino Facility (LBNF) and Deep Underground Neutrino Experiment (DUNE)," 2016. ArXiv: 1601.02984.

[172] J. Strait *et al.*, "Long-Baseline Neutrino Facility (LBNF) and Deep Underground Neutrino Experiment (DUNE)," 2016. ArXiv: 1601.05823.

[173] R. Acciarri *et al.*, "Long-Baseline Neutrino Facility (LBNF) and Deep Underground Neutrino Experiment (DUNE)," 2016. ArXiv: 1601.05471.

[174] D. Hernandez and A. Yu. Smirnov, "Discrete symmetries and model-independent patterns of lepton mixing," *Phys. Rev.*, vol. D87, no. 5, p. 053005, 2013. ArXiv: 1212.2149.

[175] T. Araki *et al.*, "CKM matrix and flavor symmetries," *Phys. Rev.*, vol. D88, p. 096002, 2013. ArXiv: 1309.4217.

[176] C. S. Lam, "A Bottom-up analysis of horizontal symmetry," 2009. ArXiv: 0907.2206.

[177] C. S. Lam, "Horizontal symmetry," *Int. J. Mod. Phys.*, vol. A23, pp. 3371–3375, 2008. ArXiv: 0711.3795.

[178] L. L. Everett, T. Garon, and A. J. Stuart, "A Bottom-Up Approach to Lepton Flavor and CP Symmetries," *JHEP*, vol. 04, p. 069, 2015. ArXiv: 1501.04336.

[179] S. F. King and C. Luhn, "Neutrino Mass and Mixing with Discrete Symmetry," *Rept. Prog. Phys.*, vol. 76, p. 056201, 2013. ArXiv: 1301.1340.

[180] I. de Medeiros Varzielas *et al.*, "Bottom-Up Discrete Symmetries for Cabibbo Mixing," *Int. J. Mod. Phys.*, vol. A32, no. 06n07, p. 1750047, 2017. ArXiv: 1605.03581.

[181] I. de Medeiros Varzielas *et al.*, "Neutrino tribimaximal mixing from a non-Abelian discrete family symmetry," *Phys. Lett.*, vol. B648, pp. 201–206, 2007. ArXiv: hep-ph/0607045.

[182] E. Ma, "Neutrino Mass Matrix from Delta(27) Symmetry," *Mod. Phys. Lett.*, vol. A21, pp. 1917–1921, 2006. ArXiv: hep-ph/0607056.

[183] I. de Medeiros Varzielas, "$\Delta(27)$ family symmetry and neutrino mixing," *JHEP*, vol. 08, p. 157, 2015. ArXiv: 1507.00338.

[184] M. Fukugita and T. Yanagida, "Barygenesis without grand unification," *Physics Letters B*, vol. 174, pp. 45 – 47, 1986.

[185] C. S. Fong, E. Nardi, and A. Riotto, "Leptogenesis in the Universe," *Adv. High Energy Phys.*, vol. 2012, p. 158303, 2012. ArXiV: 1301.3062.

[186] L. Covi, E. Roulet, and F. Vissani, "CP violating decays in leptogenesis scenarios," *Phys. Lett.*, vol. B384, pp. 169–174, 1996. ArXiv: hep-ph/9605319.

[187] M. Plumacher, "Baryogenesis and lepton number violation," *Zeitschrift fur Physik C Particles and Fields*, vol. 74, no. 3, pp. 549–559, 1997.

[188] G. F. Giudice *et al.*, "Towards a complete theory of thermal leptogenesis in the SM and MSSM," *Nucl. Phys.*, vol. B685, pp. 89–149, 2004. ArXiv: hep-ph/0310123.

[189] V. Soni, "Sphalerons and electroweak baryogenesis," *Pramana*, vol. 41, pp. 427–439, 1993.

[190] V. Kuzmin *et al.*, "On anomalous electroweak baryon-number non-conservation in the early universe," *Physics Letters B*, vol. 155, pp. 36 – 42, 1985.

[191] A. Abada, S. Davidson, A. Ibarra, F. X. Josse-Michaux, M. Losada, and A. Riotto, "Flavour Matters in Leptogenesis," *JHEP*, vol. 09, p. 010, 2006. ArXiv: hep-ph/0605281.

[192] J. M. Cline *et al.*, "Protecting the primordial baryon asymmetry from erasure by sphalerons," *Phys. Rev.*, vol. D49, pp. 6394–6409, 1994. ArXiv: hep-ph/9401208.

[193] R. Allahverdi *et al.*, "Reheating in Inflationary Cosmology: Theory and Applications," *Ann. Rev. Nucl. Part. Sci.*, vol. 60, pp. 27–51, 2010. ArXiv: 1001.2600.

[194] A. Mazumdar and B. Zaldivar, "Quantifying the reheating temperature of the universe," *Nucl. Phys.*, vol. B886, pp. 312–327, 2014. ArXiv: 1310.5143.

[195] J. M. Cline *et al.*, "Completing constrained flavor violation: lepton masses, neutrinos and leptogenesis," *Phys. Rev.*, vol. D93, no. 3, p. 036009, 2016. ArXiv: 1510.04688.

[196] G. Engelhard, Y. Grossman, E. Nardi, and Y. Nir, "The Importance of N_2 leptogenesis," *Phys. Rev. Lett.*, vol. 99, p. 081802, 2007. ArXiv: hep-ph/0612187.

[197] S. Antusch, P. Di Bari, D. A. Jones, and S. F. King, "A fuller flavour treatment of N_2-dominated leptogenesis," *Nucl. Phys.*, vol. B856, pp. 180–209, 2012. ArXiv: 1003.5132.

[198] P. Di Bari and M. Re Fiorentin, "Supersymmetric $SO(10)$-inspired leptogenesis and a new N_2-dominated scenario," *JCAP*, vol. 1603, no. 03, p. 039, 2016. ArXiv: 1512.06739.

[199] W. Buchmuller, P. Di Bari, and M. Plumacher, "Leptogenesis for pedestrians," *Annals Phys.*, vol. 315, pp. 305–351, 2005. ArXiv: hep-ph/0401240.

[200] L. Canetti *et al.*, "Probing leptogenesis with GeV-scale sterile neutrinos at LHCb and Belle II," *Phys. Rev.*, vol. D90, no. 12, p. 125005, 2014. ArXiv: 1404.7114.

[201] K. S. Jeong and F. Takahashi, "Anarchy and Leptogenesis," *JHEP*, vol. 07, p. 170, 2012. ArXiv: 1204.5453.

[202] C. Athanassopoulos *et al.*, "The Liquid scintillator neutrino detector and LAMPF neutrino source," *Nucl. Instrum. Meth.*, vol. A388, pp. 149–172, 1997. ArXiv: nucl-ex/9605002.

[203] A. A. Aguilar-Arevalo *et al.*, "A Search for electron neutrino appearance at the $\Delta m^2 \sim 1\text{eV}^2$ scale," *Phys. Rev. Lett.*, vol. 98, p. 231801, 2007. ArXiv: 0704.1500.

[204] A. A. Aguilar-Arevalo *et al.*, "Unexplained Excess of Electron-Like Events From a 1-GeV Neutrino Beam," *Phys. Rev. Lett.*, vol. 102, p. 101802, 2009. ArXiv: 0812.2243.

[205] C. Giunti and M. Laveder, "Statistical Significance of the Gallium Anomaly," *Phys. Rev.*, vol. C83, p. 065504, 2011. ArXiv: 1006.3244.

[206] G. Mention *et al.*, "The Reactor Antineutrino Anomaly," *Phys. Rev.*, vol. D83, p. 073006, 2011. ArXiv: 1101.2755.

[207] D. Cianci *et al.*, "Prospects of Light Sterile Neutrino Oscillation and CP Violation Searches at the Fermilab Short Baseline Neutrino Facility," *Phys. Rev.*, vol. D96, no. 5, p. 055001, 2017. ArXiv: 1702.01758.

[208] J. Heeck and W. Rodejohann, "Sterile neutrino anarchy," *Phys. Rev.*, vol. D87, no. 3, p. 037301, 2013. ArXiv: 1211.5295.

[209] J. Heeck, "Seesaw parametrization for n right-handed neutrinos," *Phys. Rev.*, vol. D86, p. 093023, 2012. ArXiv: 1207.5521.

[210] M. G. Aartsen *et al.*, "Search for sterile neutrino mixing using three years of IceCube DeepCore data," *Phys. Rev.*, vol. D95, no. 11, p. 112002, 2017. ArXiv: 1702.05160.

[211] P. Coloma *et al.*, "DUNE sensitivities to the mixing between sterile and tau neutrinos," 2017. ArXiv: 1707.05348.

[212] Y. Farzan and A. Yu. Smirnov, "Coherence and oscillations of cosmic neutrinos," *Nucl. Phys.*, vol. B805, pp. 356–376, 2008. ArXiv: 0803.0495.

[213] M. G. Aartsen *et al.*, "IceCube-Gen2: A Vision for the Future of Neutrino Astronomy in Antarctica," 2014. ArXiv: 1412.5106.

[214] M. Kowalski, "The Icecube Particle Astrophysics Symposium (IPA)," *Madison, USA*, 2017.

[215] Z. Djurcic *et al.*, "JUNO Conceptual Design Report," 2015. ArXiv: 1508.07166.

[216] F. An *et al.*, "Neutrino Physics with JUNO," *J. Phys.*, vol. G43, no. 3, p. 030401, 2016. ArXiv: 1507.05613.

[217] F. P. An *et al.*, "Measurement of electron antineutrino oscillation based on 1230 days of operation of the Daya Bay experiment," 2016. ArXiv: 1610.04802.

[218] M. Bustamante *et al.*, "Theoretically palatable flavor combinations of astrophysical neutrinos," *Phys. Rev. Lett.*, vol. 115, no. 16, p. 161302, 2015. ArXiv: 1506.02645.

[219] T. Kashti and E. Waxman, "Flavoring astrophysical neutrinos: Flavor ratios depend on energy," *Phys. Rev. Lett.*, vol. 95, p. 181101, 2005. ArXiv: astro-ph/0507599.

[220] S. Hummer *et al.*, "Energy dependent neutrino flavor ratios from cosmic accelerators on the Hillas plot," *Astropart. Phys.*, vol. 34, pp. 205–224, 2010. ArXiv: 1007.0006.

[221] L. A. Anchordoqui *et al.*, "Galactic point sources of TeV antineutrinos," *Phys. Lett.*, vol. B593, p. 42, 2004. ArXiv: astro-ph/0311002.

[222] M. Kachelriess *et al.*, "High energy neutrino yields from astrophysical sources I: Weakly magnetized sources," *Phys. Rev.*, vol. D74, p. 063009, 2006. ArXiv: astro-ph/0606406.

[223] C. Patrignani *et al.*, "Review of Particle Physics," *Chin. Phys.*, vol. C40, no. 10, p. 100001, 2016.

[224] M. G. Aartsen *et al.*, "A combined maximum-likelihood analysis of the high-energy astrophysical neutrino flux measured with IceCube," *Astrophys. J.*, vol. 809, no. 1, p. 98, 2015. ArXiv: 1507.03991.

[225] R. W. Rasmussen, L. Lechner, M. Ackermann, M. Kowalski, and W. Winter, "Astrophysical neutrinos flavored with Beyond the Standard Model physics," 2017. ArXiv: 1707.07684.

[226] V. Brdar, J. Kopp, and X.-P. Wang, "Sterile Neutrinos and Flavor Ratios in IceCube," *JCAP*, vol. 1701, no. 01, p. 026, 2017. ArXiv: 1611.04598.

[227] T. Ohlsson, "Status of non-standard neutrino interactions," *Rept. Prog. Phys.*, vol. 76, p. 044201, 2013. ArXiv: 1209.2710.

[228] C. Biggio, M. Blennow, and E. Fernandez-Martinez, "Loop bounds on non-standard neutrino interactions," *JHEP*, vol. 03, p. 139, 2009. ArXiv: 0902.0607.

[229] S. Razzaque and A. Yu. Smirnov, "Flavor conversion of cosmic neutrinos from hidden jets," *JHEP*, vol. 03, p. 031, 2010. ArXiv: 0912.4028.

[230] N. Fraija, "Resonant oscillations of GeV–TeV neutrinos in internal shocks from gamma-ray burst jets inside stars," *Mon. Not. Roy. Astron. Soc.*, vol. 450, no. 3, pp. 2784–2798, 2015. ArXiv: 1504.00328.

[231] N. Fraija, "GeV–PeV neutrino production and oscillation in hidden jets from gamma-ray bursts," *Mon. Not. Roy. Astron. Soc.*, vol. 437, no. 3, pp. 2187–2200, 2014. ArXiv: 1310.7061.

[232] K. Murase and K. Ioka, "TeV–PeV Neutrinos from Low-Power Gamma-Ray Burst Jets inside Stars," *Phys. Rev. Lett.*, vol. 111, no. 12, p. 121102, 2013. ArXiv: 1306.2274.

[233] S. Sahu and B. Zhang, "Effect of Resonant Neutrino Oscillation on TeV Neutrino Flavor Ratio from Choked GRBs," *Res. Astron. Astrophys.*, vol. 10, pp. 943–949, 2010. ArXiv: 1007.4582.

[234] C. Lunardini and A. Yu. Smirnov, "The Minimum width condition for neutrino conversion in matter," *Nucl. Phys.*, vol. B583, pp. 260–290, 2000. ArXiv: hep-ph/0002152.

[235] O. Mena *et al.*, "Oscillation effects on high-energy neutrino fluxes from astrophysical hidden sources," *Phys. Rev.*, vol. D75, p. 063003, 2007. ArXiv: astro-ph/0612325.

[236] T. Shigeyama and K. Nomoto, "Theoretical light curve of sn 1987a and mixing of hydrogen and nickel in the ejecta," *Astrophys. J.*, vol. 360, pp. 242–256, 1990.

[237] D. Arnett, "Massive star evolution and sn 1987a," *Astrophysical Journal*, vol. 383, pp. 295–307, 1991.

[238] P. Meszaros and E. Waxman, "TeV neutrinos from successful and choked gamma-ray bursts," *Phys. Rev. Lett.*, vol. 87, p. 171102, 2001. ArXiv: astro-ph/0103275.

[239] S. Razzaque *et al.*, "Neutrino tomography of gamma-ray bursts and massive stellar collapses," *Phys. Rev.*, vol. D68, p. 083001, 2003. ArXiv: astro-ph/0303505.

[240] S. Razzaque, P. Meszaros, and E. Waxman, "TeV neutrinos from core collapse supernovae and hypernovae," *Phys. Rev. Lett.*, vol. 93, p. 181101, 2004. ArXiv: astro-ph/0407064.

[241] J. Alvarez-Muniz and P. Meszaros, "High energy neutrinos from radio-quiet AGNs," *Phys. Rev.*, vol. D70, p. 123001, 2004. ArXiv: astro-ph/0409034.

[242] F. W. Stecker, "A note on high energy neutrinos from agn cores," *Phys. Rev.*, vol. D72, p. 107301, 2005. ArXiv: astro-ph/0510537.

[243] L. Wolfenstein, "Different varieties of massive Dirac neutrinos," *Nuclear Physics B*, vol. 186, pp. 147 – 152, 1981.

[244] L. Wolfenstein, "CP properties of Majorana neutrinos and double beta decay," *Physics Letters B*, vol. 107, pp. 77 – 79, 1981.

[245] S. Petcov, "On pseudo-Dirac neutrinos, neutrino oscillations and neutrinoless double β-decay," *Physics Letters B*, vol. 110, pp. 245 – 249, 1982.

[246] J. F. Beacom *et al.*, "PseudoDirac neutrinos: A Challenge for neutrino telescopes," *Phys. Rev. Lett.*, vol. 92, p. 011101, 2004. ArXiv: hep-ph/0307151.

[247] P. Keranen *et al.*, "Effects of sterile neutrinos on the ultrahigh-energy cosmic neutrino flux," *Phys. Lett.*, vol. B574, pp. 162–168, 2003. ArXiv: hep-ph/0307041.

[248] A. Esmaili, "Pseudo-Dirac Neutrino Scenario: Cosmic Neutrinos at Neutrino Telescopes," *Phys. Rev.*, vol. D81, p. 013006, 2010. ArXiv: 0909.5410.

[249] J. F. Beacom *et al.*, "Decay of high-energy astrophysical neutrinos," *Phys. Rev. Lett.*, vol. 90, p. 181301, 2003. ArXiv: hep-ph/0211305.

[250] K. Hirata *et al.*, "Observation of a neutrino burst from the supernova sn1987a," *Phys. Rev. Lett.*, vol. 58, pp. 1490–1493, 1987.

[251] A. S. Joshipura *et al.*, "Constraints on decay plus oscillation solutions of the solar neutrino problem," *Phys. Rev.*, vol. D66, p. 113008, 2002. ArXiv: hep-ph/0203181.

[252] A. Bandyopadhyay *et al.*, "Neutrino decay confronts the SNO data," *Phys. Lett.*, vol. B555, pp. 33–42, 2003. ArXiv: hep-ph/0204173.

[253] K. Eguchi *et al.*, "A high sensitivity search for $\bar{\nu}_e$s from the sun and other sources at KamLAND," *Phys. Rev. Lett.*, vol. 92, p. 071301, 2004. ArXiv: hep-ex/0310047.

[254] B. Aharmim *et al.*, "Electron antineutrino search at the Sudbury Neutrino Observatory," *Phys. Rev.*, vol. D70, p. 093014, 2004. ArXiv: hep-ex/0407029.

[255] M. C. Gonzalez-Garcia *et al.*, "Status of Oscillation plus Decay of Atmospheric and Long-Baseline Neutrinos," *Phys. Lett.*, vol. B663, pp. 405–409, 2008. ArXiv: 0802.3699.

[256] P. Mehta and W. Winter, "Interplay of energy dependent astrophysical neutrino flavor ratios and new physics effects," *JCAP*, vol. 1103, p. 041, 2011. ArXiv: 1101.2673.

[257] J. M. Berryman *et al.*, "Non-Unitary Neutrino Propagation From Neutrino Decay," *Phys. Lett.*, vol. B742, pp. 74–79, 2015. ArXiv: 1407.6631.

[258] P. Baerwald *et al.*, "Neutrino Decays over Cosmological Distances and the Implications for Neutrino Telescopes," *JCAP*, vol. 1210, p. 020, 2012. ArXiv: 1208.4600.

[259] M. Maltoni and W. Winter, "Testing neutrino oscillations plus decay with neutrino telescopes," *JHEP*, vol. 07, p. 064, 2008. ArXiv: 0803.2050.

[260] D. Hooper, D. Morgan, and E. Winstanley, "Probing quantum decoherence with high-energy neutrinos," *Phys. Lett.*, vol. B609, pp. 206–211, 2005. ArXiv: hep-ph/0410094.

[261] D. Morgan, E. Winstanley, J. Brunner, and L. F. Thompson, "Probing quantum decoherence in atmospheric neutrino oscillations with a neutrino telescope," *Astropart. Phys.*, vol. 25, pp. 311–327, 2006. ArXiv: astro-ph/0412618.

[262] D. Hooper, D. Morgan, and E. Winstanley, "Lorentz and CPT invariance violation in high-energy neutrinos," *Phys. Rev.*, vol. D72, p. 065009, 2005. ArXiv: hep-ph/0506091.

[263] M. Blennow, T. Ohlsson, and W. Winter, "Damping signatures in future neutrino oscillation experiments," *JHEP*, vol. 06, p. 049, 2005. ArXiv: hep-ph/0502147.

[264] C. A. Arguelles, T. Katori, and J. Salvado, "New Physics in Astrophysical Neutrino Flavor," *Phys. Rev. Lett.*, vol. 115, p. 161303, 2015. ArXiv: 1506.02043.

[265] K. Abe *et al.*, "Test of Lorentz invariance with atmospheric neutrinos," *Phys. Rev.*, vol. D91, no. 5, p. 052003, 2015. ArXiv: 1410.4267.

[266] R. Abbasi *et al.*, "Search for a Lorentz-violating sidereal signal with atmospheric neutrinos in IceCube," *Phys. Rev.*, vol. D82, p. 112003, 2010. ArXiv: 1010.4096.

[267] P. F. de Salas, R. A. Lineros, and M. Tortola, "Neutrino propagation in the galactic dark matter halo," *Phys. Rev.*, vol. D94, no. 12, p. 123001, 2016. ArXiv: 1601.05798.

[268] J. F. Navarro, C. S. Frenk, and S. D. M. White, "The Structure of cold dark matter halos," *Astrophys. J.*, vol. 462, pp. 563–575, 1996. ArXiv: astro-ph/9508025.

[269] J. F. Navarro, C. S. Frenk, and S. D. M. White, "A Universal density profile from hierarchical clustering," *Astrophys. J.*, vol. 490, pp. 493–508, 1997. ArXiv: astro-ph/9611107.

[270] R. Catena and P. Ullio, "A novel determination of the local dark matter density," *JCAP*, vol. 1008, p. 004, 2010. ArXiv: 0907.0018.

[271] M. Pato, F. Iocco, and G. Bertone, "Dynamical constraints on the dark matter distribution in the Milky Way," *JCAP*, vol. 1512, no. 12, p. 001, 2015. ArXiv: 1504.06324.

[272] Q. Xia *et al.*, "Determining the local dark matter density with LAMOST data," *Monthly Notices of the Royal Astronomical Society*, vol. 458, no. 4, p. 3839, 2016.

[273] H. Pas, S. Pakvasa, and T. J. Weiler, "Sterile-active neutrino oscillations and shortcuts in the extra dimension," *Phys. Rev.*, vol. D72, p. 095017, 2005. ArXiv: hep-ph/0504096.

[274] A. Esmaili, O. L. G. Peres, and Z. Tabrizi, "Probing Large Extra Dimensions With IceCube," *JCAP*, vol. 1412, no. 12, p. 002, 2014. ArXiv: 1409.3502.

[275] M. M. Reynoso *et al.*, "Effects of large extra dimensions on cosmogenic neutrino fluxes," *Journal of Physics G: Nuclear and Particle Physics*, vol. 40, no. 5, p. 055202, 2013.

[276] M. M. Reynoso *et al.*, "Corrigendum: Effects of large extra dimensions on cosmogenic neutrino fluxes," *Journal of Physics G: Nuclear and Particle Physics*, vol. 40, no. 7, p. 079501, 2013.

[277] A. V. Kisselev, "High-energy cosmic neutrinos and extra spatial dimensions," *Physics of Atomic Nuclei*, vol. 73, no. 6, pp. 996–1014, 2010.

[278] J. Lykken, O. Mena, and S. Razzaque, "Ultrahigh-energy neutrino flux as a probe of large extra-dimensions," *JCAP*, vol. 0712, p. 015, 2007. ArXiv: 0705.2029.

[279] D. J. H. Chung and K. Freese, "Can geodesics in extra dimensions solve the cosmological horizon problem?," *Phys. Rev.*, vol. D62, p. 063513, 2000. ArXiv: hep-ph/9910235.

[280] D. J. H. Chung and K. Freese, "Cosmological challenges in theories with extra dimensions and remarks on the horizon problem," *Phys. Rev.*, vol. D61, p. 023511, 2000. ArXiv: hep-ph/9906542.

[281] C. Csaki, J. Erlich, and C. Grojean, "Gravitational Lorentz violations and adjustment of the cosmological constant in asymmetrically warped space-times," *Nucl. Phys.*, vol. B604, pp. 312–342, 2001. ArXiv: hep-th/0012143.

[282] E. Aeikens *et al.*, "Flavor ratios of extragalactic neutrinos and neutrino shortcuts in extra dimensions," *JCAP*, vol. 1510, no. 10, p. 005, 2015. ArXiv: 1410.0408.

[283] Y. D. O. Arcos and S. Sahu, "Earth matter effect on GeV neutrino propagation," 2015. ArXiv: 1510.07103.

[284] M. C. Gonzalez-Garcia and M. Maltoni, "Determination of matter potential from global analysis of neutrino oscillation data," *JHEP*, vol. 09, p. 152, 2013. ArXiv: 1307.3092.

[285] A. M. Dziewonski and D. L. Anderson, "Preliminary reference earth model," *Physics of the Earth and Planetary Interiors*, vol. 25, no. 4, pp. 297 – 356, 1981.

[286] M. C. Gonzalez-Garcia *et al.*, "Non-standard neutrino interactions in the Earth and the flavor of astrophysical neutrinos," *Astropart. Phys.*, vol. 84, pp. 15–22, 2016. ArXiv: 1605.08055.

[287] S. L. Glashow, "Resonant scattering of antineutrinos," *Phys. Rev.*, vol. 118, pp. 316–317, 1960.

[288] L. A. Anchordoqui *et al.*, "Neutrinos as a diagnostic of high energy astrophysical processes," *Phys. Lett.*, vol. B621, pp. 18–21, 2005. ArXiv: hep-ph/0410003.

[289] D. Biehl *et al.*, "Astrophysical Neutrino Production Diagnostics with the Glashow Resonance," *JCAP*, vol. 1701, p. 033, 2017. ArXiv: 1611.07983.

[290] J. G. Learned and S. Pakvasa, "Detecting tau-neutrino oscillations at PeV energies," *Astropart. Phys.*, vol. 3, pp. 267–274, 1995. ArXiv: hep-ph/9405296.

[291] J. F. Beacom *et al.*, "Measuring flavor ratios of high-energy astrophysical neutrinos," *Phys. Rev.*, vol. D68, p. 093005, 2003. ArXiv: hep-ph/0307025.

[292] T. DeYoung *et al.*, "Astrophysical tau neutrino detection in kilometer-scale Cherenkov detectors via muonic tau decay," *Astropart. Phys.*, vol. 27, pp. 238–243, 2007. ArXiv: astro-ph/0608486.

[293] A. Palladino, G. Pagliaroli, F. L. Villante, and F. Vissani, "Double pulses and cascades above 2 PeV in IceCube," *Eur. Phys. J.*, vol. C76, no. 2, p. 52, 2016. ArXiv: 1510.05921.

[294] S. W. Li, M. Bustamante, and J. F. Beacom, "Echo Technique to Distinguish Flavors of Astrophysical Neutrinos," 2016. ArXiv: 1606.06290.

[295] M. Usner, "The International Cosmic Ray Conference (ICRC)," *Busan, South Korea*, 2017.

[296] M. M. Reynoso *et al.*, "Propagation of high-energy neutrinos in a background of ultralight scalar dark matter," *Astropart. Phys.*, vol. 82, pp. 10–20, 2016. ArXiv: 1605.09671.

[297] B. P. Abbott *et al.*, "Observation of Gravitational Waves from a Binary Black Hole Merger," *Phys. Rev. Lett.*, vol. 116, p. 061102, 2016.

[298] B. P. Abbott *et al.*, "GW170817: Observation of Gravitational Waves from a Binary Neutron Star Inspiral," *Phys. Rev. Lett.*, vol. 119, p. 161101, 2017.

[299] K. Murase, S. Inoue, and S. Nagataki, "Cosmic Rays Above the Second Knee from Clusters of Galaxies and Associated High-Energy Neutrino Emission," *Astrophys. J.*, vol. 689, p. L105, 2008. ArXiv: 0805.0104.

[300] K. Murase and E. Waxman, "Constraining High-Energy Cosmic Neutrino Sources: Implications and Prospects," *Phys. Rev.*, vol. D94, no. 10, p. 103006, 2016. ArXiv: 1607.01601.

[301] M. Bustamante *et al.*, "Multi-messenger light curves from gamma-ray bursts in the internal shock model," *Astrophys. J.*, vol. 837, no. 1, p. 33, 2017. ArXiv: 1606.02325.

[302] D. Biehl *et al.*, "Cosmic-Ray and Neutrino Emission from Gamma-Ray Bursts with a Nuclear Cascade," 2017. ArXiv: 1705.08909.

[303] C. Blanco and D. Hooper, "High-Energy Gamma Rays and Neutrinos from Nearby Radio Galaxies," 2017. ArXiv: 1706.07047.

[304] A. E. C. Hernandez *et al.*, "Fermion and scalar phenomenology of a two-Higgs-doublet model with S_3," *Phys. Rev.*, vol. D93, no. 1, p. 016003, 2016. ArXiv: 1509.02083.